Development of a method to observe demagnetization field in thin-foiled magnets using electron holography

李, 秀眞

DOCTORAL THESIS

Development of a method to observe demagnetization field in thin-foiled magnets using electron holography

JANUARY 2023

Department of Applied Quantum Physics and Nuclear Engineering

Kyushu University

LEE Sujin

Table of Content

1. Introduction

1.1 Background on permanent magnet

The tremendous momentum and rapid growth in global electricity production has forced researchers and engineers to innovate the design of motors, transformers and generators to convert energy more efficiently, which has prompted their minimization and lightweight with advanced performance. Especially, the demand on the improved traction motors have led to the revolution of the permanent magnets in the last century, i.e., the development of new hard magnetic materials as shown in Fig. 1.1 [1]. In the early history of magnet before the break of "shape barrier" occurred in the Netherlands in 1951 [2], the magnets could only be manufactured in awkward shapes such as needles, bars, and horseshoes [3]. The reason of shape limit for making the magnets is the demagnetization field (H_d). The H_d for a uniformly magnetized ellipsoid can be represented with magnetization (M)

$$H_d = -\mathcal{N}M, \quad (1.1)$$

where $\mathcal{N}$ stands for demagnetizing factor that takes values between 0 and 1 and depends only on the shape of magnet. For example, $\mathcal{N}$ is 0 for a long needle magnetized along its axis or a thin film magnetized in-plane and 1 for a thin film magnetized perpendicular to the plane. Other values of $\mathcal{N}$ can be defined with reference to an ellipsoidal specimen. M represents the

magnetic moment (*i.e.*, fundamental magnetic quantity for a magnet in the unit of Am^2) per unit volume for which the unit of M (also H) is Am^{-1}. The permanent magnet ideally has a broad $M(H)$ hysteresis loop as shown in Fig. 1.2 (a), in which the magnetic field of hysteresis loop represents the field acting in the magnet (*i.e.*, $H_0 + H_d$), where H_0 stands for applied magnetic field. With the broad $M(H)$ hysteresis loop, the coercivity (H_c) must exceed the critical value determined by the spontaneous magnetization (M_s), which means the shape barrier for magnet manufacture are broken. This breakthrough appeared in the 1950s with new family of materials called hexagonal ferrites, after which permanent magnets could be designed into any desired shape. Until now the ferrite has occupied the large portion of permanent magnet markets due to its low cost.

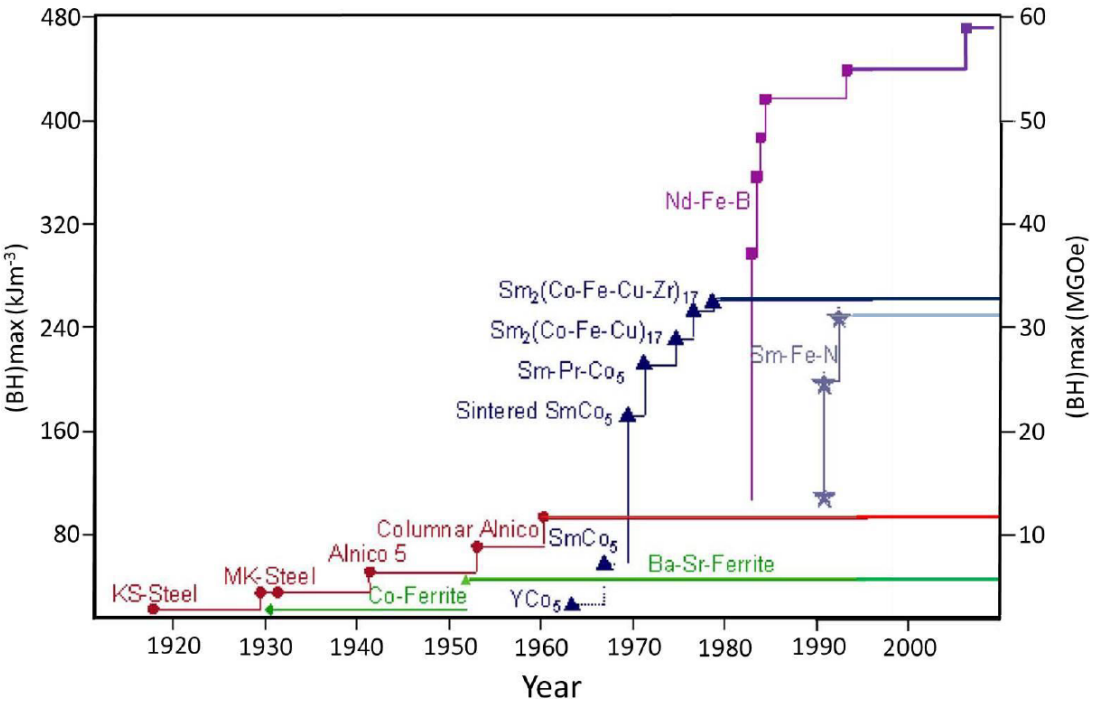

Fig. 1.1 Improvement in the maximum energy product at room temperature of the permanent magnets in the 20th century with different types of permanent magnets [1].

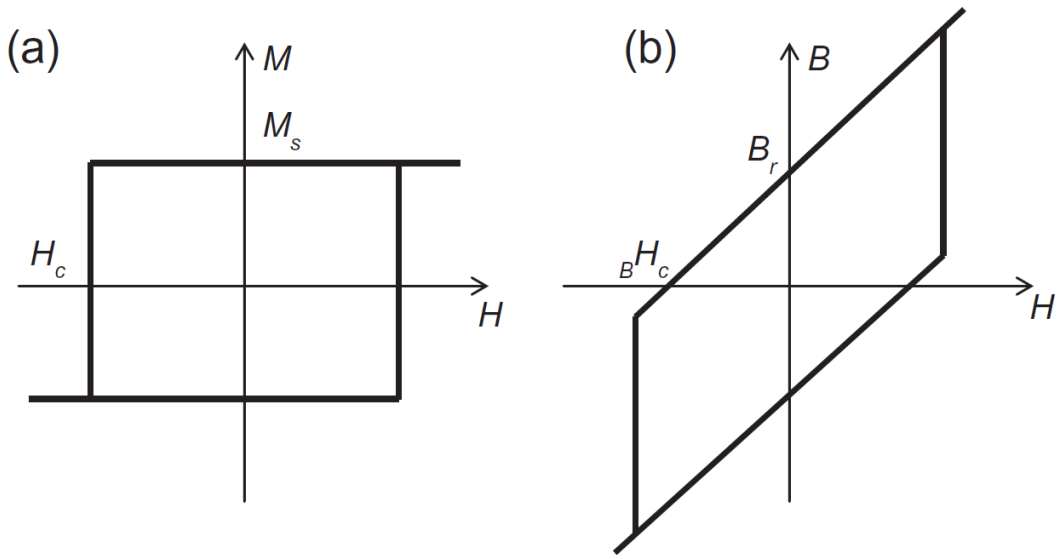

Fig. 1.2 Ideal hysteresis loop for a permanent magnet: (a) an *M*(*H*) loop and (b) a *B*(*H*) loop [4].

The permanent magnet into thin films with perpendicular anisotropy (*i.e.*, $\mathcal{N} \approx 1$) are useful for spintronics and magnetic recording. However, it can be pointless if permanent magnets are needed to provide force, torque, electromotive force or voltages without constant energy consumption because the film that are uniformly magnetized perpendicularly cannot produce the stray field [5]. Note that the stary field (H_s) represents *H*-field that are originated from the magnet outside its own volume, where *H*-field originated from the magnet within its own volume is used as same symbol H_d, *i.e.*, demagnetization field.

The maximum energy product $|BH|_{max}$ is an important property of a permanent magnet related to the *B*(*H*) loop of the magnet, as shown in Fig. 1.2 (b). In vacuum region, the magnetic flux density *B* can be expressed by the magnetic field *H*:

$$B = \mu_0 H \qquad (1.2)$$

where the μ_o is the vacuum permeability. On the other hand, within the magnet, *B* can be represented by the equation of the sum of *M* and *H*:

$$B = \mu_0 (M + H) \qquad (1.3)$$

The energy density in the stray magnetic field is $1/2 \int |BH| dV$ for the integral over the magnet volume, which provides the energy product is proportional to M^2 [5]. We assume that the magnetization remains fully saturated well into the second quadrant in *M*(*H*) loop in Fig. 1.2 (a), and Eq. (1.4) can be given using Eq. (1.1) and (1.3):

$$|BH| = \mu_0 (H + M) H = \mu_0 (1 - \mathcal{N}) \mathcal{N} M_s^2. \qquad (1.4)$$

We can obtain $\mathcal{N} = 1/2$ by differentiating with respect to $\mathcal{N}$ to find the maximum, which can give the absolute upper limit deduced for the ideal *B(H)* loop of Fig. 1.2 (b).

$$|BH|_{MAX} = \frac{1}{4} \mu_0 M_s^2. \qquad (1.5)$$

A shape of magnet for $\mathcal{N} = 1/2$ corresponds to a low cylinder of height whose height is roughly equal to its radius. Unfortunately, the magnetization curve for real magnet deviates from the ideal square loop of Fig. 1.2 (a), which results in the achievable maximum energy product:

$$|BH|_{max} < \frac{1}{4}\mu_0 M_s^2. \quad (1.6)$$

The development trends of permanent magnet have been directed in seeking to improve the $|BH|_{max}$ as shown in Fig. 1.1. Alnico alloy (Fe-Al-Ni-Co) [3] is the new magnet developed in the early 20th century, which can be used for high application temperature due to high Curie temperature (~850℃). The $|BH|_{MAX}$ was improved to ~80 kJm^{-3} with large spontaneous magnetization (~1.1 MAm^{-1}). However, low intrinsic coercivity was a problem originated from the low anisotropy field due to a fine needle-shaped ferromagnetic phase in a nonmagnetic matrix, which constrained the shape of the magnet to be rod-shaped or horseshoe-shaped (i.e., the shape barrier). After that, with the development of ferrites [6], magnet production became free from the shape barrier, but the ferrite magnets have low $|BH|_{max}$ (~40 kJm^{-3}) because of their low remanence. Sm-Co systems developed in the 1966 [7,8] had the largest magnetic anisotropy constant, which had attracted the interests from researchers in the rare earth permanent magnets. Especially, the $|BH|_{max}$ of Sm_2Co_{15} type magnet was improved to ~240 kJm^{-3}, but the widespread use of Sm-Co based magnet were hampered by the complex heat treatment procedure and high cost of Sm and Co. From the late 1970s to the early 1980s, many efforts were made to obtain better rare earth permanent

magnets as replacing Sm with cheap elements such as Nd, replacing Co with Fe, and adding B to stabilize the R-Fe alloys. In the end of the efforts, the rare earth permanent magnets based on $Nd_2Fe_{14}B$ were independently developed by two different research groups in 1982; Croat et. al. [9,10] obtained the Nd-Fe-B magnets with nanocrystallinity called MAGNEQUENCH, and Sagawa et. al. [11] produced the sintered Nd-Fe-B magnets, called NEOMAX, by powder metallurgy method. The Nd-Fe-B magnets, illustrated in Fig.1.3, is comprised of very cheap element Fe with a large ferromagnetic moment, a small amount of a relative abundant light rare earth element Nd providing large anisotropy, and B occupying 2 % of the volume of the unit cell to stabilize the tetragonal crystal structure. It is

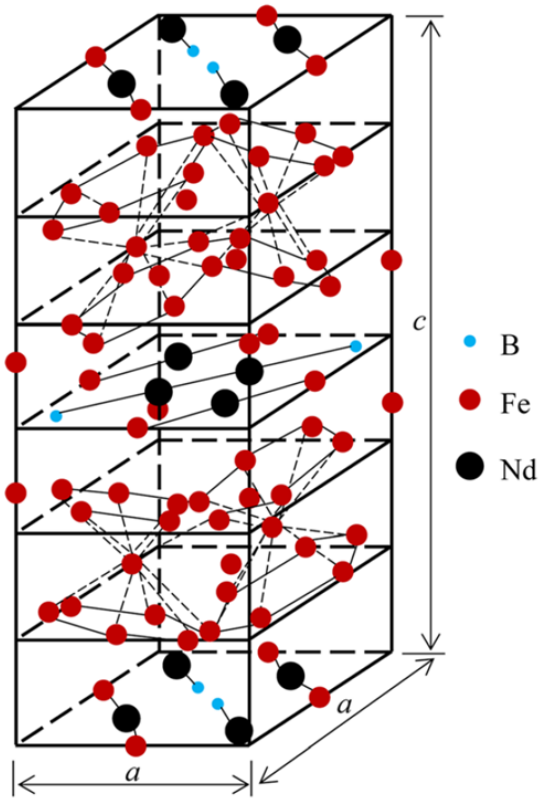

Fig. 1.3 Tetragonal unit cell of the Nd2Fe14B crystal. a=8.80 Å and c=12.19 Å [12].

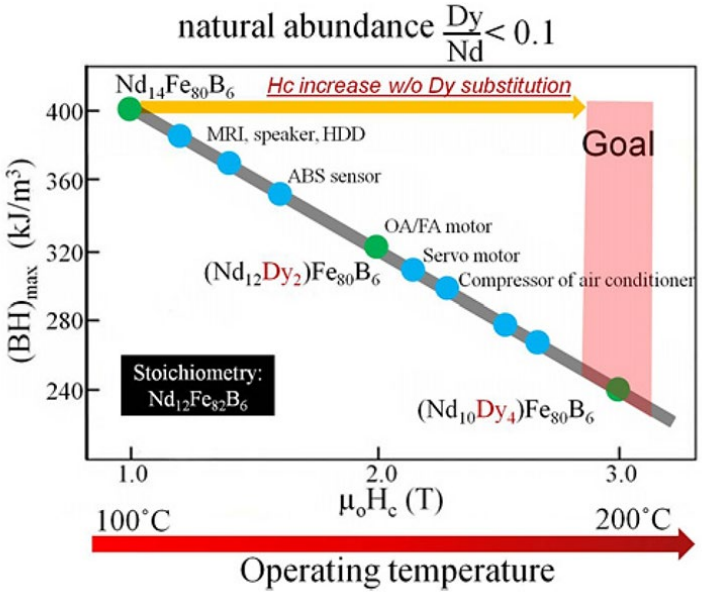

Fig. 1.4 Energy product $|BH|_{max}$ and coercivity of commercial sintered magnets and their compositions [17].

reported that the maximum energy product for a laboratory magnet is increased by ~480 kJm^{-3}, which almost approaches the theoretical maximum value of $|BH|_{MAX}$=512 kJm^{-3}. Also, the $|BH|_{max}$ of commercial grades showed over ~450 kJm^{-3} [13].

1.2 Development of Nd-Fe-B magnets for high coercivity

The coercivity represents the measured value of critical magnetic field to induce undesired magnetization reversal and is used to characterize the ability of permanent magnet. In order for the magnetic domains to be reversed by the applied external magnetic fields or the thermal fluctuations, the energy barrier provides due to the magnetocrystalline anisotropy (K_u) must be overcome. However, the phenomenon on the magnetization reversal is complex because it depends not only on the crystallographic microstructure but also on magnetic domain structures, which is sensitive to

the magnetic dipolar interactions and the exchanging interactions between the neighboring magnetic domains. This makes the analysis of the coercivity mechanism more difficult [14]. The coercivity of permanent magnet is determined by the easiest path of these mechanism, in which the magnetization reversal can occur either continuously through a coherent or incoherent rotation, or discontinuously through a dynamic domain motion. High coercivity can be achieved by impeding magnetization rotation with magnetic anisotropy and hindering the nucleation or the growth of reverse magnetic domains [15].

1.2.1 Current status of Nd-Fe-B magnet

The growing demand of hybrid/electric vehicles, robots, and drones requires further improvement of the coercivity of permanent magnets because it enables the significant miniaturization of traction motors. Among the sintered permanent magnets that have been commercialized, the Nd-Fe-B system provides a high maximum energy product attributed to the high magnetocrystalline anisotropy ($K_u \approx 4.5$ MJ m^{-3}) and high saturation magnetization (≈ 1.6 T) in the $Nd_2Fe_{14}B$ phase [4,16,17]. However, with regard to a commercial Nd-Fe-B magnet subjected to optimized heat treatment, the value of coercivity at room temperature is approximately 1.2 T, which is only ~20% relative to the anisotropy field H_A ($\mu_o H_A \approx 7$ T) in the $Nd_2Fe_{14}B$ phase. As another important problem, the coercivity is reduced significantly at elevated temperatures. For example, the value of coercivity is only approximately 0.2 T at the operating temperature (~473 K) of traction motors. A solution to increase the coercivity is the substitution of Dy for Nd,

where a value of 3 T is achieved at room temperature due to the improvement in the magnetocrystalline anisotropy of $Dy_2Fe_{14}B$ (~15 T). However, due to the antiferromagnetic spin coupling between Dy and Fe, this substitution reduces the saturation magnetization of the sintered magnet, and consequently in $|BH|_{max}$ as shown in Fig. 1.4 [17]. From an industrial viewpoint, Dy is a type of critical element with limited natural resources. To overcome this issue, there are many studies on coercivity enhancement of Nd-Fe-B magnets with free of Dy, which will be discussed in the next sections.

1.2.2 Tailoring of magnetism in grain boundary

An efficient way for improvement of the coercivity (H_c) is tailoring of the magnetism in the grain boundary (GB) region, which has finite thickness (*i.e.*, <3 nm in commercial Nd-Fe-B magnets). Since the invention of the Nd-Fe-B sintered magnet, the GB region had been considered to be in a nonferromagnetic state [18-23], which could achieve exchange decoupling between neighboring $Nd_2Fe_{14}B$ crystal grains and accordingly suppress the avalanche propagation of reversed magnetic domains. However, Sepehri-Amin et. al. [24] reported that an unexpectedly high concentration of Fe (>60%) within the narrow GB region was revealed by the three-dimensional (3-D) atom probe study. This result provided that the narrow GB was ferromagnetic by the magnetic measurements using the model thin film approximating the chemical compositions of the specimen. Their prediction was justified by several methods of direct magnetic measurements including soft X-ray magnetic circular dichroism [25], spin-polarized scanning

electron microscopy [26], and electron holography [27]. These studies recalled further examinations on the tailoring of GB magnetism and its impact on the improvement of coercivity [28-30]. For example, Sasaki et. al. [] confirmed that the coercivity of the sintered magnet increased by 1.8 T through the Ga-doping, which reduced the Fe content in the GB phase, while the Nd-rich composed of Ga and Cu increased due to the improved wettability of the Nd-rich phase. These results indicated that the GB magnetism tailoring (i.e., the formation of non-ferromagnetic GB) achieved the improvement of the coercivity due to the exchange decoupling of the neighboring $Nd_2Fe_{14}B$ grains. Grain boundary diffusion process (GBDP) is known as useful method to form the non-ferromagnetic GB, which employed on various magnets including from the hydrogen disproportionation desorption recombination processed magnet [31,32] to the hot-deformed magnet [33-36]. The coercivity of the diffused magnets using various kinds of low melting point eutectic alloys at room temperature improved by ~2.6T. However, the GBDP provides the loss of the remanent magnetization because of rapid increase of Nd-rich phase within the magnet [37].

1.2.3 Demagnetization field within Nd-Fe-B magnet

Another important subject in regard to the coercivity mechanism is the distribution of H_d within the Nd-Fe-B magnet, as H_d is a factor responsible for the undesired magnetization reversal [38-41]. Although the magnitude and/or distribution of H_d in a sintered magnet depends on the shape, size, and the orientational dispersion of the $Nd_2Fe_{14}B$ crystal grains, an enhancement of H_d can assist nucleation of the reverse magnetic domains, which leads to

deterioration of the coercivity [40, 41]. The impact of H_d on the coercivity mechanism has been studied using micromagnetic simulations, in which model specimens with simple shapes were addressed [41-47]. Among the models, Kronmüller model is used to analyze the coercivity phenomenologically, where the coercivity can be expressed as:

$$H_c(T) = \alpha H_A(T) - N_{eff} M_s(T), \qquad (1.7)$$

where parameter α describes the reduction of the H_A due to the microstructural defects or the c-axis misalignment of grains, N_{eff} describes the reduction of the coercivity due to the demagnetization field, which can be regarded as the microstructural factors influencing local effective demagnetization [48]. The micromagnetic parameters α and N_{eff} for various types of Nd-Fe-B magnets can be deduced from the slope and the intercept by linear fitting of H_c/M_s versus H_a/M_s. According to the study by Fischbacher et. al., the N_{eff} [49] increased as the artificial crystal grains became platelet shaped. In addition, as a result of the H_d calculations using the micromagnetic simulation (*i.e.*, Landau-Lifshitz-Gilbert calculations [50,51]), Li et al. [41] indicated that both the edges and corners of crystal grains (approximated by a polyhedron) could provide potential nucleation sites for magnetization reversal, which is strongly related to the distribution of demagnetization field that is the largest at the c-plane surfaces of the grains as shown in Fig. 1.5. Bance et al. [43] calculated the demagnetization field for different diameters of artificial crystal grains (from 55 nm to 8.3 μm) to discuss the roles of the surface grains on the magnetization reversal. However, despite these intensive studies with simulations, experimental tools that allow for discussion about H_d within real magnet are still lacking.

This provides us the motivation to obtain the information about H_d within a Nd-Fe-B magnet using electron holography observation, which will be discussed in Chapter 1.4.

1.3 Background on electron holography

Electron holography [52,53] is a powerful electron-interference technique that can be used through transmission electron microscopy (TEM). Initially, electron holography was proposed to recover the phase shift to overcome the problem of TEM imaging in which the phase shift information of the high-energy electron wave passing through the specimen is lost [54]. Note that the phase shift of electron waves passed through specimen is directly related to

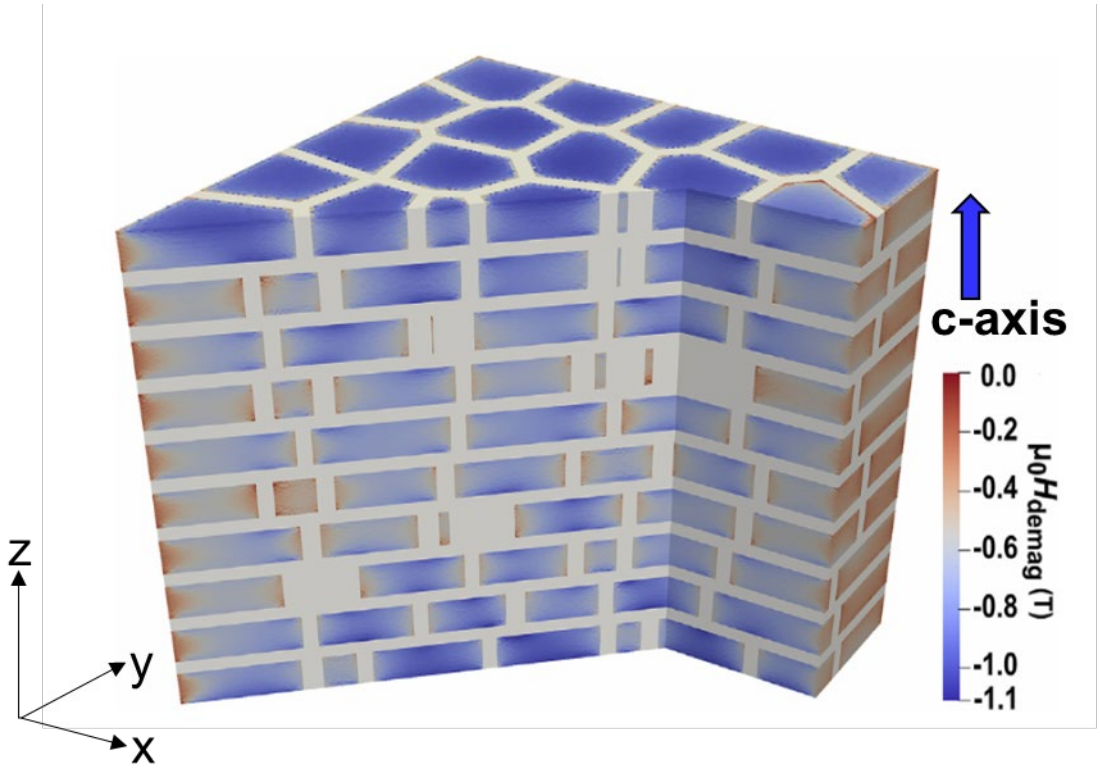

Fig. 1.5 The z component of H_d distribution for the model specimen. The direction of c-axis indicates z direction [41].

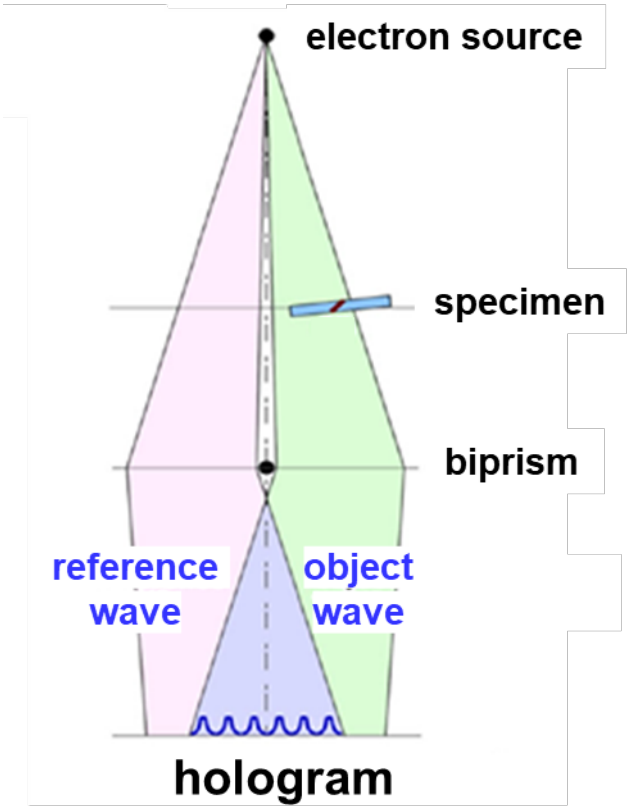

Fig. 1.6 Electron-beam diagram showing conventional electron holography experiments [27]

the in-plane of magnetic flux density and the electrostatic potential in the specimen, which can provide the quantitative measurement of electric and magnetic field with high resolution and sensitivity. Among the holography techniques, off-axis electron holography is commonly most used as illustrated schematically in Fig. 1.6. The specimen is examined using coherent illumination from an electron source with the region of interest positioned so that it covers approximately half the field of view. The electrostatic biprism located close to a conjugate image plane in the microscope functions to overlap the object wave passing through the region of interest on the specimen with the reference wave passing through the vacuum. The interference pattern (*i.e.*, electron hologram) must then be processed to retrieve or reconstruct a complex electronic wavefunction that

conveys the desired phase and amplitude information about the sample. Regarding magnetic materials, holograms are typically recorded with the conventional microscope objective lens turned off, as strong magnetic field derived from objective lens can make the specimen undesirably magnetized along the electron beam direction. For this point, specimen may be placed in a field-free environment using a Lorentz lens (*e.g.*, mini-lens located under the lower objective pole-piece) to record holograms at high magnification. The phase information (*i.e.*, reconstructed phase image) obtained from the electron hologram allows for the magnetic flux density measurement from a nanometer-scaled area, and reveals the magnetic domain structure.

The practical use of electron holography could be achieved from the development of stable coherent field emission gun (FEG) on TEM [55]. Thereafter, the progress of peripheral techniques includes the rapid growth in computer speed and memory [52, 56], the multiple biprism [57-59] enabling the holograms to be collected free from undesired Fresnel fringes, the sophisticated aberration-correction systems bring about the reconstructed phase image in the improved lateral resolution, the advent of the slow-scan charge-coupled-device (CCD) camera [60] that records the hologram with sufficient contrast minimizing the specimen/beam drift within a reasonable exposure time, and in recent the development of the direct detection camera having an excellent modulation transfer function [61].

1.4 Magnetic domain observation using electron holography

1.4.1 Advantages of electron holography

In addition to electron holography, Lorentz microscopy, one of the TEM

techniques, is useful method to image the magnetic domain structures. Lorentz microscopy uses the sideways deflection of incident electrons (*i.e.*, Lorentz force) derived from the magnetic field of the specimen. By Lorentz microscopy (*i.e.*, using Fresnel mode) the position of magnetic domain walls can be indicated by black and white lines due to the deficiency and excess of electrons induced by Lorentz force in the defocused condition [62,63], which allows for *in-situ* observation of domain wall motion during magnetization reversal. However, it is difficult to observe the domain walls with high contrast in Lorentz image under the complex magnetization distribution such as the direction of magnetic flux lines across the domain walls, and difficult to obtain the quantification information of magnetic field. Several techniques used to investigate the local magnetic properties of materials, including micro-SQUID magnetometry [64], magnetic force microscopy (MFM) [65,66], photoemission electron microscopy (PEEM) [67] also have insufficient spatial resolution for the observation of magnetic domain structures in nanometer-sized magnetic materials and/or vortex-core structures.

On the other hand, electron holography can provide the information of detailed magnetization distribution or the direction and strength of the magnetic flux density at high resolution that can approach the nanometer scale, and can reveal the leakage of the magnetic field outside the specimen. Therefore, it is possible to understand important magnetic properties such as coercivity and magnetization reversal behavior through in-depth analysis on the magnetic domain structure using electron holography.

1.4.2 Research review

Thanks to useful features described in the above section, electron holography has been intensively applied to the various magnetic materials fields including both hard-magnetic and soft-magnetic materials [68-72], magnetic nanoparticles [73-80], magnetic recording system [81], fluxon in superconductor [82], magnetic skyrmions and chiral systems [83-88], etc.

For the development of hard and soft magnetic materials with their high performance, many studies using electron holography has been conducted to obtain the information of magnetic domains. McCartney and Zhu [68,69]

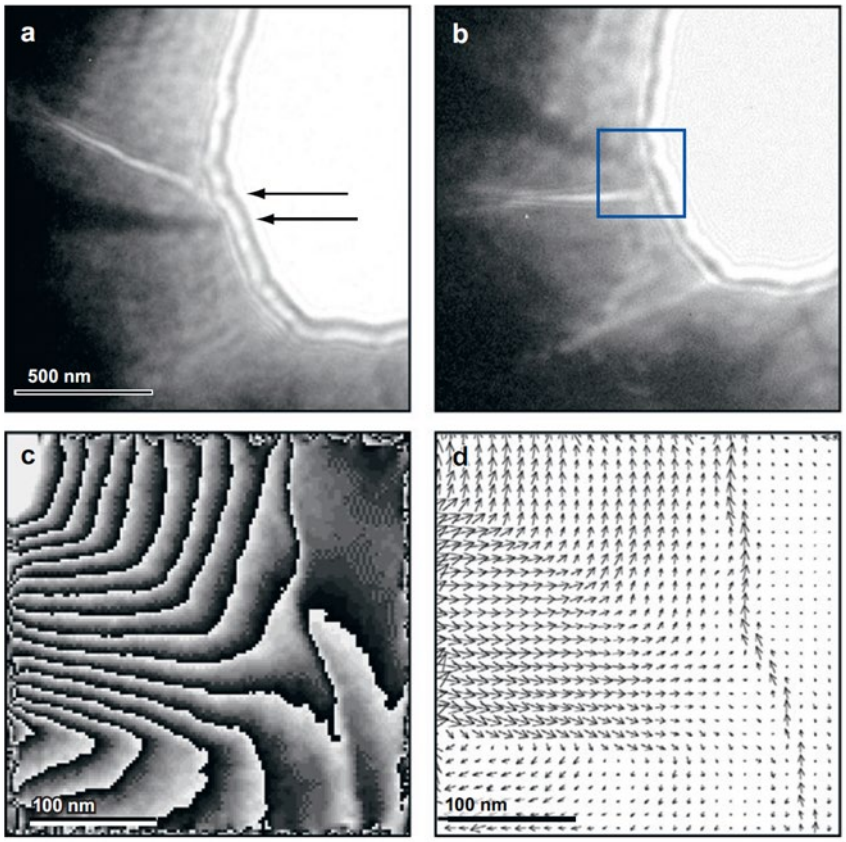

Fig. 1.7 (a) and (b) Overfocus and under focus Lorentz micrographs of Nd2Fe14B showing domains walls. (c) Reconstructed phase image from area outlined in (b), with phase contour spacings of 0.5π radians. (d) Magnetic induction map derived from phase gradients showing 90° and 180° domain walls [68, 69]

revealed the magnetic domain structures in sintered $Nd_2Fe_{14}B$ permanent magnet using Lorentz microscopy in Figs. 1.7(a) and (b), and Fig. 1.7(c), magnified region from Fig. 1.7(b), showed the reconstructed phase image where the spacing of the contour lines (*i.e.*, the phase shift per unit length [53]) provides information about the in-plane component of *B*. Direction and size of arrows in a vector map of Fig. 1.7(d) indicates the direction and strength of the *B*, which are given from the phase gradient information using Fig. 1.7(c). As a result, the magnetization of three magnetic domains for the top, middle, and bottom position were determined to be 0.8, 1.2, and 0.5 T, respectively. They thought that these differences happened because of unconsidered phase information immediately above and below the sample

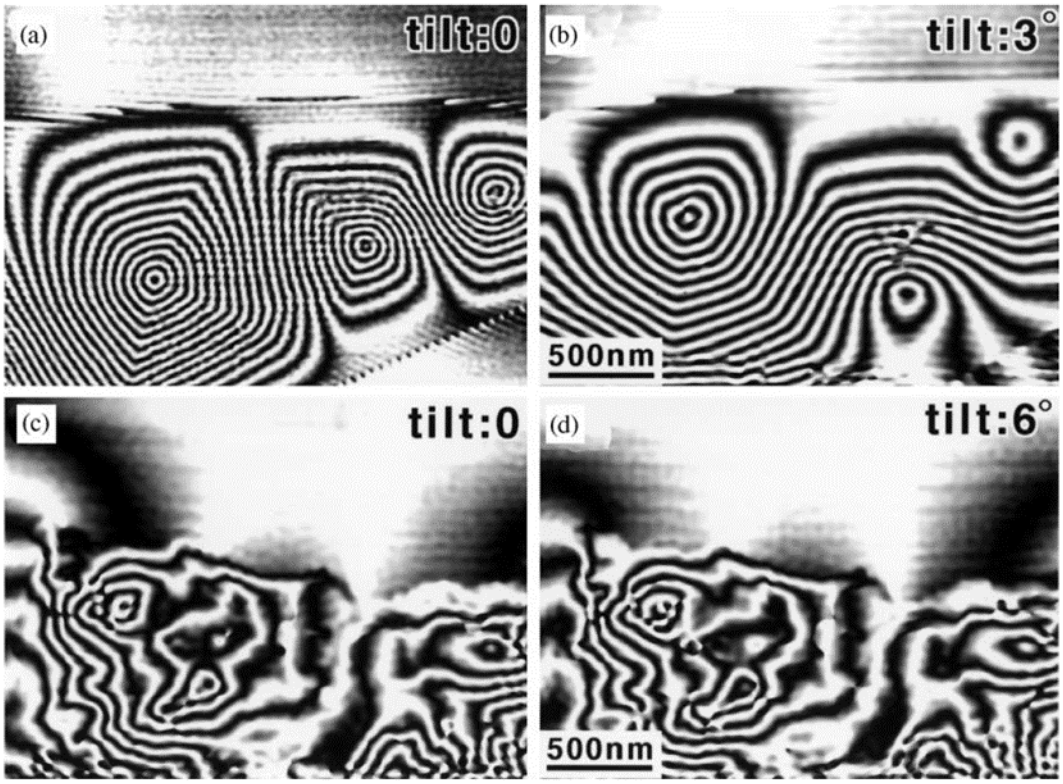

Fig. 1.8 (a) and (b) Reconstructed phase images of as-quenched $Fe_{73.5}Cu_1Nb_3Si_{13.5}B_9$ for the increase of tilting angle. (c) and (d) Reconstructed phase images of $Fe_{73.5}Cu_1Nb_3Si_{13.5}B_9$ annealed at 973 K for the increase of tilting angle. In-plane components of the external magnetic field are (b) 8.3 A/m and (d) 16.6 A/m [71].

surface or holography feature only sensitive to the in-plane components of the B.

Especially, H_c is strongly related to not only microstructure but also magnetic domain structures, as described in Chapter 1.2. Shindo et. al. [71] investigated *in-situ* observation of magnetic domain structures in variably annealed $Fe_{73.5}Cu_1Nb_3Si_{13.5}B_9$ soft magnets in Fig. 1.8 as the external magnetic field was applied perpendicular to the specimen. They figured out through the reconstructed phase images of Figs. 1.8 (c) and (d) the undesired increase of the H_c in terms of the soft magnetic magnet was because the

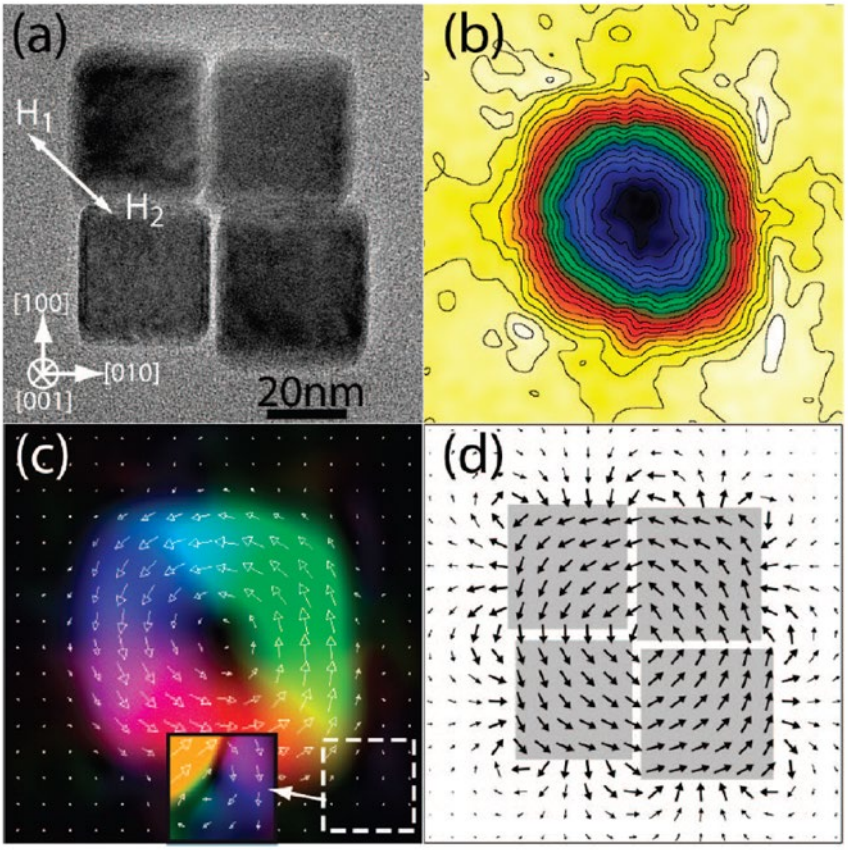

Fig.1.9 Electron holography and micromagnetic simulations for a single isolated Fe nanocube. (a) TEM image reveals the cubic structure and an external iron oxide layer surrounding the nanocube. (b) Phase image corresponding to the magnetic contribution to the phase shift with 0.05 rad isophase contours. Note the cylindrical symmetry of the magnetic flux line. (c) Vector map of the in-plane induction [75].

strong pinning of magnetic domain walls was induced by the increased size of precipitates during annealing at the grain boundaries.

The analysis on magnetic nanostructures has significantly attracted many fundamental scientific interests [89] as magnetic nanoparticles can be applied for magnetic recording. However, the nanoparticles make the phase

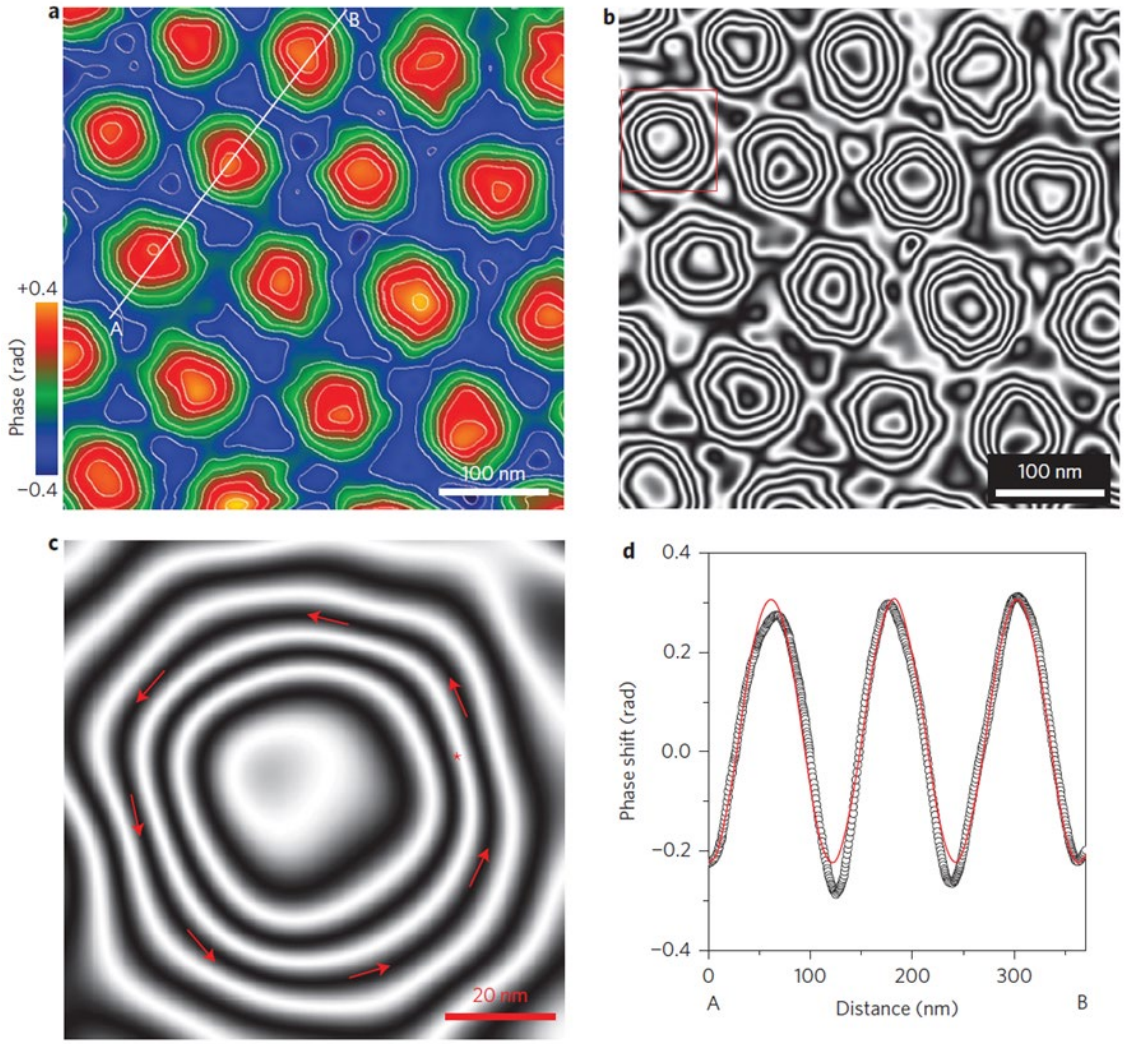

Fig.1.10 Magnetic flux maps of the skyrmion lattice. (a) Two-dimensional map showing the phase shift due to magnetic vector potential. A plot A-B is shown in (d). (b) Magnetic flux in the skyrmion lattice. (c) Enlarged image corresponding to the area indicated by the red square in (b). The asterisk in red indicates the region in which we determined the in-plane component of *B*. (d) Phase shift profile corresponding to line A-B in (a) [83].

analysis difficult because magnetic phase change decreases with their reduced width (i.e., due to the size dependence of magnetic phase shift). Also, experimental parameters can affect the phase analysis because narrow fringe spacing in holograms to adapt for the limited specimen dimensions deteriorates the fringe contrast (*i.e.*, visibility of holograms) [90], which results in the low quality of phase image. Great details about parameters determining the precision of phase analysis will be discussed in Chapter 6.

Snoek et. al. [75] revealed magnetic domain structures (*i.e.*, vortex states) at remanent state (with no external applied magnetic field) of room temperature for 30 nm Fe nanocubes with single crystallinity. They successfully characterized the vortex states in the assemblies of 4 nanocubes at high spatial resolution (~5 nm) with the combination of micromagnetic simulation, which is presented in Fig. 1.9. Park et. al. [83] showed that electron holography is also useful tool for visualization for complex magnetic structure (*i.e.*, three-dimensional spin structures of a skyrmion lattice) in helimagnet $Fe_{0.5}Co_{0.5}Si$ thin foil, as shown in Fig. 1.10. The magnetic flux density even in weak phase objects such as skyrmions could be determined as 0.04 ± 0.005 T for the asterisk region of Fig. 1.10 (c) by separating the phase shift due to electrostatic potential and magnetic phase shift. The operation to only obtain the magnetic phase shift was also performed in this thesis, and the process will be explained in Chapter 2.

1.4.3 Challenge in electron holography: phase information of demagnetization field

As the research review suggests, electron holography is only sensitive to *B*,

which is comprised of the contributions from M and H in Eqs. (1.2) and (1.3). In addition, there are two sources for the magnetic field H, *i.e.*, the H_d inside of the specimen, and H_s that exists outside of the specimen that are described in Chapter 1.1. Therefore, it remains challenging to extract phase information about H_d within a thin-foil specimen. This problem is common for other methods of electron microscopy, such as Lorentz microscopy and differential phase contrast method.

1.5 Purpose and construction of this study

The purpose of this study is to establish a method that allows for extracting the phase information related to H_d within a single-crystalline $Nd_2Fe_{14}B$ foil. A process to determine the phase information approximating H_d will be explained in the subsequent chapters. The validity of this method is examined via the application to an artificial bar magnet ($Nd_2Fe_{14}B$) shaped in a square pillar. Finally, this method is applied to the mapping of H_d in a real specimen that is made of a single-crystalline $Nd_2Fe_{14}B$ grain. On the other hand, the accuracy of this method proposed should improve, as the results (*i.e.*, the phase map and the mapping about H_d) are obtained through various processes such as the subtraction or differentiation of the phase information. Towards the precision improvement of the method, the noise reduction, as one of useful imaging processing, is applied to the reconstructed phase image of a thin-foil $Nd_2Fe_{14}B$ specimen, in which the author uses the wavelet hidden Markov model (WHMM) that allows the discrimination of weak signal than the threshold. This study is divided into 7 chapters and the construction of this study is follows:

In Chapter 2, the basic principles and applications of electron microscopy techniques that are utilized in this study will be described, including TEM, electron holography, electron diffraction, and electron energy-loss spectroscopy (EELS).

In Chapter 3, the method that extracts the phase information relevant to H_d from the electron holography observation will be proposed, for which the process to reduce undesired other phase components about M and H_s will be also explained using the surface integral for magnetic fields. Also, technical problems of this method and unsuccessful cases of the phase H_d mapping will be remarked.

In Chapter 4, the method proposed in Chapter 3 will be applied to an artificial $Nd_2Fe_{14}B$ specimen having a simple rectangular shape. Following the method, we shall figure out the effectiveness of this method that provides the phase information of H_d extracted from the phase shift representing B. The distribution of H_d within the artificial specimen will be mapped, derived from the phase shift H_d.

In Chapter 5, the method will be also applied to a real thin-foil specimen consisting of a single $Nd_2Fe_{14}B$ grain to obtain the map of H_d. For unwanted phase contributions due to M and H_s, diverse electron microscope techniques including TEM observations, the electron diffraction pattern and EELS will be exploited to obtain the crystallographic/morphologic features of the real specimen. As a result of applying the method, the map of H_d will be compared with the result of micromagnetic simulations to demonstrate the validity of the method.

In Chapter 6, WHMM for denoising of electron holography observation for

a thin-foil $Nd_2Fe_{14}B$ specimen will be conducted to examine the effectiveness of noise reduction that can be applied to the method for the precision improvement of phase analysis in the future. The impact of the noise reduction will be discussed in terms of the phase discontinuity induced by the low visibility of electron holograms.

In Chapter 7, the achievements in this study are summarized.

Chapter 1 References

1. J. M. D. Coey (2011) Hard magnetic materials: A perspective, *IEEE Transactions on magnetics 47*(12): 4671-4681.

2. J. J. Went, G. W. Rathenau, E. W. Gorter, & G. W. Van Oosterhout (1952) Hexagonal iron-oxide compounds as permanent-magnet materials, *Physical Review 86*(3): 424.

3. R. A. McCurrie (1982) The structure and properties of alnico permanent magnet alloys, *Handbook of ferromagnetic materials*, *3*, 107-188.

4. J. M. D. Coey (2012). Permanent magnets: Plugging the gap. *Scripta Materialia 67*(6): 524-529.

5. J. M. Coey (2010) *Magnetism and magnetic materials*, Cambridge university press.

6. H. Stäblein (1982) Hard ferrites and plastoferrites, *Handbook of Ferromagnetic Materials 3*: 441-602.

7. K. Strnat (1970) The recent development of permanent magnet materials containing rare earth metals, *IEEE Transactions on Magnetics 6*(2): 182-190.

8. J. F. Liu, Y. Zhang, D. Dimitrov, & G. C. Hadjipanayis (1999) Microstructure and high temperature magnetic properties of Sm (Co, Cu, Fe, Zr) z (z= 6.7–9.1) permanent magnets, *Journal of applied physics 85*(5): 2800-2804.

9. J. J. Croat, J. F. Herbst, R. W. Lee, & F. E. Pinkerton (1984), Pr-Fe and Nd-Fe-based materials: A new class of high-performance permanent magnets, *Journal of Applied Physics 55*(6): 2078-2082.

10. J. J. Croat, J. F. Herbst, R. W. Lee, & F. E. Pinkerton (1984) High-energy product Nd-Fe-B permanent magnets, *Applied Physics Letters*, *44*(1): 148-149.

11. M. Sagawa, S. Fujimura, N. Togawa, H. Yamamoto, & Y. Matsuura, (1984) New material for permanent magnets on a base of Nd and Fe, *Journal of Applied Physics 55*(6): 2083-2087.

12. M. Li, & T. Tamura (2020) Segmentation and alignment of Nd2Fe14B platelets in Nd-Cu eutectic alloys using the electromagnetic vibration technique, *Metallurgical and Materials Transactions A 51*(6): 2939-2956.

13. Y. Matsuura (2006) Recent development of Nd–Fe–B sintered magnets and their applications, *Journal of magnetism and magnetic materials 303*(2): 344-347.

14. L. I. U. Jun (2015) Microstructure and coercivity relationship of hot-deformed Nd-Fe-B anisotropic magnets.

15. J. D. Livingston (1981) A review of coercivity mechanisms, *Journal of Applied Physics 52*(3): 2544-2548.

16. M. Sagawa, S. Fujimura, H. Yamamoto, Y. Matsuura, and S. Hirosawa (1985) Magnetic properties of rare-earth-iron-boron permanent magnet materials. *J. Appl. Phys.* 57: 4094-4096.

17. K. Hono and H. Sepehri-Amin (2012) Strategy for high-coercivity Nd-Fe-B magnets. *Scr. Mater.* 67: 530-535.

18. Y. Sun, G. B. Han, M. Liu, B. P. Han, & R. W. Gao (2007) Intergranular phase dependence of anisotropy and coercivity in nanoscaled permanent magnets, *Materials Letters 61*(21): 4294-4296.

19. O. Gutfleisch, (2000) Controlling the properties of high energy density permanent magnetic materials by different processing routes, *Journal of Physics D: Applied Physics 33*(17): R157.

20. W. F. Li, T. Ohkubo, & K. Hono (2009) Effect of post-sinter annealing on the coercivity and microstructure of Nd–Fe–B permanent magnets, *Acta Materialia 57*(5): 1337-1346.

21. T. Schrefl, H. F. Schmidts, J. Fidler, & H. Kronmüller (1993) The role of exchange and dipolar coupling at grain boundaries in hard magnetic materials, *Journal of magnetism and magnetic materials 124*(3): 251-261.

22. F. Vial, F. Joly, E. Nevalainen, M. Sagawa, K. Hiraga, & K. T. Park (2002) Improvement of coercivity of sintered NdFeB permanent magnets by heat treatment, *Journal of magnetism and magnetic materials 242*: 1329-1334.

23. R. K. Mishra, J. K. Chen, & G. Thomas, (1986) Effect of annealing on the microstructure of sintered Nd-Fe-B magnets, *Journal of applied physics 59*(6): 2244-2246.

24. H. Sepehri-Amin, T. Ohkubo, T. Shima, & K. Hono (2012) Grain

boundary and interface chemistry of an Nd–Fe–B-based sintered magnet, *Acta Materialia 60*(3): 819-830.

25. T. Nakamura, A. Yasui, Y. Kotani, T. Fukagawa, T. Nishiuchi, H. Iwai, ... & S. Hirosawa (2014) Direct observation of ferromagnetism in grain boundary phase of Nd-Fe-B sintered magnet using soft x-ray magnetic circular dichroism, *Applied Physics Letters 105*(20): 202404.

26. T. Kohashi, K. Motai, T. Nishiuchi, & S. Hirosawa (2014) Magnetism in grain-boundary phase of a NdFeB sintered magnet studied by spin-polarized scanning electron microscopy, *Applied Physics Letters 104*(23): 232408.

27. Y. Murakami, T. Tanigaki, T. T. Sasaki, Y. Takeno, H. S. Park, T. Matsuda, ... & D. Shindo, (2014) Magnetism of ultrathin intergranular boundary regions in Nd–Fe–B permanent magnets, *Acta Materialia 71*: 370-379.

28. T. T. Sasaki, T. Ohkubo, Y. Takada, T. Sato, A. Kato, Y. Kaneko, & K. Hono (2016) Formation of non-ferromagnetic grain boundary phase in a Ga-doped Nd-rich Nd–Fe–B sintered magnet, *Scripta Materialia 113*: 218-221.

29. L. Zhao, & J. M. Greneche (2019) On the magnetism of grain boundary phase and its contribution to the abnormal openness of recoil loops in hot-deformed magnets, *Journal of Physics D: Applied Physics 53*(9): 095002.

30. Y. Ainai, S. Kou, Y. Tatetsu, & Y. Gohda (2020) First-principles study on magnetism of a crystalline grain-boundary phase in Nd–Fe–B permanent magnets, *Japanese Journal of Applied Physics 59*(6): 060904.

31. H. Sepehri-Amin, T. Ohkubo, T. Nishiuchi, S. Hirosawa, & K. Hono, (2010) Coercivity enhancement of hydrogenation–disproportionation–

desorption–recombination processed Nd–Fe–B powders by the diffusion of Nd–Cu eutectic alloys, *Scripta Materialia 63*(11): 1124-1127.

32. C. Mishima, K. Noguchi, M. Yamazaki, H. Mitrai, Y. Honkuta, Proceedings of the 21th International Workshop on Rare Earth Permanent Magnets and Their Applications, Bled, Slovenia, 2010.

33. H. Sepehri-Amin, T. Ohkubo, S. Nagashima, M. Yano, T. Shoji, A. Kato, ... & K. Hono (2013) High-coercivity ultrafine-grained anisotropic Nd–Fe–B magnets processed by hot deformation and the Nd–Cu grain boundary diffusion process, *Acta Materialia 61*(17): 6622-6634.

34. L. Liu, H. Sepehri-Ami, T. Ohkubo, M. Yano, A. Kato, T. Shoji, & K. Hono (2016) Coercivity enhancement of hot-deformed Nd-Fe-B magnets by the eutectic grain boundary diffusion process. *Journal of Alloys and Compounds 666*: 432-439.

35. L. Liu, H. Sepehri-Amin, T. T. Sasaki, T. Ohkubo, M. Yano, N. Sakuma, ... & K. Hono (2018) Coercivity enhancement of Nd-Fe-B hot-deformed magnets by the eutectic grain boundary diffusion process using Nd-Ga-Cu and Nd-Fe-Ga-Cu alloys, *AIP Advances 8*(5): 056205.

36. U. M. R. Seelam, L. Liu, T. Akiya, H. Sepehri-Amin, T. Ohkubo, N. Sakuma, ... & K. Hono (2016) Coercivity of the Nd–Fe–B hot-deformed magnets diffusion-processed with low melting temperature glass forming alloys, *Journal of Magnetism and Magnetic Materials 412*: 234-242.

37. T. Akiya, J. Liu, H. Sepehri-Amin, T. Ohkubo, K. Hioki, A. Hattori, & K. Hono (2014) Low temperature diffusion process using rare earth-Cu eutectic alloys for hot-deformed Nd-Fe-B bulk magnets, *Journal of Applied*

Physics 115(17): 17A766.

38. W. Rave, K. Ramstöck, and A. Hubert (1998) Corners and nucleation in micromagnetics. *J. Magn. Magn. Mater.* 183: 329-333.

39. T. Schrefl, J. Fidler, and H. Kronmüller (1994) Nucleation fields of hard magnetic particles in 2D and 3D micromagnetic calculations. *J. Magn. Magn. Mater.* 138: 15-30.

40. J. Thielsch, D. Suess, L. Schultz, and O. Gutfleish (2013) Dependence of coercivity on length ratios in sub-micron $Nd_2Fe_{14}B$ particles with rectangular prism shape. *J. Appl. Phys.* 114: 223909.

41. J. Li, Lihua Liu, H. Sepehri-Amin, Xin Tang, T. Ohkubo, N. Sakuma, T. Shoji, A. Kato, T. Schrefl, and K. Hono (2018) Coercivity and its thermal stability of NdFeB hot-deformed magnets enhanced by the eutectic grain boundary diffusion process. *Acta Mater.* 161: 171-181.

42. M. Grönefeld and H. Kronmüller (1989) Calculation of strayfields near grain edges in permanent magnet material. *J. Magn. Magn. Mater.* 80: 223-228.

43. S. Bance, B. Seebacher, T. Schrefl, L. Exl, M. Winklhofer, G. Hrkac, G. Zimanyi, T. Shoji, M. Yano, N. Sakuma, M. Ito, A. Kato, and A. Manabe (2014) Grain-size dependent demagnetizing factors in permanent magnets. *J. Appl. Phys.* 116: 233903.

44. J. Fidler and T. Schrefl (1996) Overview of Nd-Fe-B magnets and coercivity. *J. Appl. Phys.* 79: 5029-5034.

45. J. Fidler and T. Schrefl (2000) Micromagnetic modelling-the current state of the art. *J. Phys. D: Appl. Phys.* 33: R135.

46. H. Sepehri-Amin, T. Ohkubo, M. Gruber, T. Schrefl, and K. Hono (2014) Micromagnetic simulations on the grain size dependence of coercivity in anisotropic Nd-Fe-B sintered magnets. *Scr. Mater.* 89: 29-32.

47. W. Li, Q. Zhou, L. Z. Zhao, Q. X. Wang, X. C. Zhong, and Z. W. Liu (2018) Micromagnetic simulation of anisotropic grain boundary diffusion for sintered Nd-Fe-B magnets. *J. Magn. Magn. Mater.* 451: 704-709.

48. H. Kronmüller, K. D. Durst, & M. Sagawa (1988) Analysis of the magnetic hardening mechanism in RE-FeB permanent magnets, *Journal of Magnetism and Magnetic Materials 74*(3): 291-302.

49. J. Fischbacher, A. Kovacs, L. Ex, J. Kühnel, E. Mehofer, H. Sepehri-Amin, ... & T. Schrefl (2018) Searching the weakest link: Demagnetizing fields and magnetization reversal in permanent magnets, *Scripta Materialia 154*: 253-258.

50. T.L. Gilbert (1955) A Lagrangian formulation of the gyromagnetic equation of the magnetization field. *Phys. Rev.* 100: 1243.

51. L.D. Landau and E. M. Lifshitz (1935) On the theory of the dispersion of magnetic permeability in ferromagnetic bodies. *Phys. Z. Sowjet.* 8: 153–169.

52. E. Völkl, L. F. Allard, and D. C. Joy (1999) *Introduction to Electron Holography.* (Kluwer Academic/Plenum Publishers, New York.)

53. A. Tonomura (1999) *Electron Holography (2nd ed.).* (Springer, Heidelberg)

54. R. E. Dunin-Borkowsk, T. Kasama, A. Wei, S. L. Tripp, M. J. Hÿtch, E. Snoeck, ... & A. Putnis (2004) Off-axis electron holography of magnetic

nanowires and chains, rings, and planar arrays of magnetic nanoparticles, *Microscopy research and technique 64*(5-6): 390-402.

55. A. Tonomura, T. Matsuda, J. Endo, H. Todokoro, & T. Komoda (1979). Development of a field emission electron microscope, *Microscopy*, *28*(1): 1-11.

56. W. J. De Ruijter, & J. K. Weiss (1993) Detection limits in quantitative off-axis electron holography, *Ultramicroscopy 50*(3): 269-283.

57. K. Harada, and A. Tonomura (2004) Double-biprism electron interferometry, *Appl. Phys. Lett.* 84: 3229.

58. T. Tanigaki, Y. Inada, S. Aizawa, T. Suzuki, H. S. Park, T. Matsuda, A. Taniyama, D. Shindo, and A. Tonomura (2012) Split-illumination electron holography, *Appl. Phys. Lett.* 101: 043101.

59. F. Röder, F. Houdellier, T. Denneulin, E. Snoeck, & M. Hÿtch (2016). Realization of a tilted reference wave for electron holography by means of a condenser biprism, *Ultramicroscopy 161*: 23-40.

60. W. J. De Ruijter (1995) Imaging properties and applications of slow-scan charge-coupled device cameras suitable for electron microscopy, *Micron 26*(3): 247-275.

61. S. L. Chang, C. Dwyer, J. Barthel, C. B. Boothroyd, & R. E. Dunin-Borkowski (2016) Performance of a direct detection camera for off-axis electron holography, *Ultramicroscopy 161*, 90-97.

62. P. B. Hirsch, A. Howie, R. B. Nicholson, D. W. Pashley, & M. J. Whelan, (1965) Electron Microscopy of Thin Crystals, Butterworths. *London, UK*, *358*.

63. P. J. Grundy, & R. S. Tebble (1968) Lorentz electron microscopy, *Advances in Physics 17*(66): 153-242.

64. W. Wernsdorfer, K. Hasselbach, A. Benoit, B. Barbara, B. Doudin, J. Meier, ... & D. Mailly (1997) Measurements of magnetization switching in individual nickel nanowires, *Physical Review B*, *55*(17): 11552.

65. K. Matsuyama, S. Komatsu, & Y. Nozaki (2000) Magnetic properties of nanostructured wires deposited on the side edge of patterned thin film, *Journal of Applied Physics 87*(9): 4724-4726.

66. S. P. Li, D. Peyrade, M. Natali, A. Lebib, Y. Chen, U. Ebels, ... & K. Ounadjela (2001) Flux closure structures in cobalt rings, *Physical Review Letters 86*(6): 1102.

67. G. Schönhense (1999) Imaging of magnetic structures by photoemission electron microscopy, *Journal of Physics: Condensed Matter 11*(48): 9517.

68. M. R. McCartney and Y. Zhu (1998) Induction mapping of $Nd_2Fe_{14}B$ magnetic domains by electron holography. *Appl. Phys. Lett.* 72: 1380-1382.

69. M. R. McCartney and Y. Zhu (1998) Off-axis electron holographic mapping of magnetic domains in $Nd_2Fe_{14}B$. *J. Appl. Phys.* 83: 6414-6416.

70. Y. Zhu and M. R. McCartney (1998) Magnetic-domain structure of $Nd_2Fe_{14}B$ permanent magnets. *J. Appl. Phys.* 84: 3267-3272.

71. D. Shindo, Y. G. Park, and Y. Yoshizawa (2002) Magnetic domain structures of $Fe_{73.5}Cu_1Nb_3Si_{13.5}B_9$ films studied by electron holography. *J. Magn. Magn. Mater.* 238: 101-108.

72. Z. Akase, K. Kimura, T. Saito, K. Niitsu, T. Tanigaki, Y. Iwasaki, P. Sharma, A. Makino, and D. Shindo (2022) Magnetic flux in soft magnetic Fe-Si-B-P-Cu amorphous alloy containing nanocrystallites analyzed by electron holography. *J. Magn. Magn. Mater.* 541: 168519.

73. M. J. Hÿtch, R. E. Dunin-Borkowski, M. R. Scheinfein, J. Moulin, C. Duhamel, F. Mazaleyrat, and Y. Champion (2003) Vortex flux channeling in magnetic nanoparticle chains. *Phys. Rev. Lett.* 91: 257207.

74. K. Yamamoto, S. A. Majetich, M. R. McCartney, M. Sachan, S. Yamamuro, and T. Hirayama (2008) Direct visualization of dipolar ferromagnetic domain structures in Co nanoparticle monolayers by electron holography. *Appl. Phys. Lett.* 93: 082502.

75. E. Snoeck, C. Gatel, L. M. Lacroix, T. Blon, S. Lachaize, J. Carrey, M. Respaud, and B. Chaudret (2008) Magnetic configurations of 30 nm iron nanocubes studied by electron holography. *Nano Lett.* 8: 4293-4298.

76. Y. Takeno, Y. Murakami, T. Sato, T. Tanigaki, H. S. Park, D. Shindo, R. M. Ferguson, and K. M. Krishnan (2014) Morphology and magnetic flux distribution in superparamagnetic, single-crystalline Fe_3O_4 nanoparticle rings. *Appl. Phys. Lett.* 105: 183102.

77. M. Ammar, M. LoBue, E. Snoeck, M. Hÿtch, Y. Champion, R. Barrué, and F. Mazaleyrat (2008) A quantitative analysis of magnetic vortices in Permalloy nanoparticles characterized by electron holography. *J. Magn. Magn. Mater.* 320: e716-e719.

78. S. L. Tripp and R. E. Dunin-Borkowski, and A. Wei (2003) Flux closure in self-assembled cobalt nanoparticle rings. *Angew. Chem. Int. Ed.* 42: 5591-5593.

79. S. Yamamuro, K. Yamamoto, D. L. Peng, T. Hirayama, and K. Sumiyama (2007) Random dipolar ferromagnetism in Co/CoO core-shell cluster assemblies observed by electron holography. *Appl. Phys. Lett.* 90: 242510.

80. A. Tonomura, T. Matsuda, J. Endo, T. Arii, and K. Mihama (1980) Direct observation of fine structure of magnetic domain walls by electron holography. *Phys. Rev. Lett.* 44: 1430

81. N. Osakabe, K. Yoshida, Y. Horiuchi, T. Matsuda, H. Tanabe, T. Okuwaki, J. Endo, H. Fujiwara, and A. Tonomura (1983) Observation of recorded magnetization pattern by electron holography. *Appl. Phys. Lett.* 42: 746.

82. S. Hasegawa, T. Matsuda, J. Endo, N. Osakabe, M. lgarashi, T. Kobayashi, M. Naito, A. Tonomura, and R. Aoki (1991) Magnetic-flux quanta in superconducting thin films observed by electron holography and digital phase analysis. *Phys. Rev.* B 43: 7631.

83. H. S. Park, X. Yu, S. Aizawa, T. Tanigaki, T. Akashi, Y. Takahashi, T. Matsuda, N. Kanazawa, Y. Onose, D. Shindo, A. Tonomura, and Y. Tokura (2014) Observation of the magnetic flux and three-dimensional structure of skyrmion lattices by electron holography. *Nature Nanotech.* 9: 337-342.

84. J. C. Loudon, A. C. Twitchett-Harrison, D. Cortés-Ortuño, M. T. Birch, L. A. Turnbull, A. Štefančič, F. Y. Ogrin, E. O. Burgos-Parra, N. Bukin, A. Laurenson, H. Popescu, M. Beg, O. Hovorka, H. Fangohr, P, A. Midgley, G.

Balakrishnan, and P. D. Hatton (2019) Do images of Biskyrmions Show Type-II Bubbles?. *Adv. Mater.* 31: 1806598.

85. F. Zheng, H. Li, S. Wang, D. Song, C. Jin, W. Wei, A. Kovács, J. Zang, M. Tian, Y. Zhang, H. Du, and R. E. Dunin-Borkowski (2017) Direct imaging of a zero-field target skyrmion and its polarity switch in a chiral magnetic nanodisk. *Phys. Rev. Lett.* 119: 197205

86. T. Denneulin, J. Caron, M. Hoffmann, M. Lin, H. K. Tan, A. Kovács, S. Blügel, and R. E. Dunin-Borkowski (2021) Off-axis electron holography of Néel-type skyrmions in multilayers of heavy metals and ferromagnets. *Ultramicrosc.* 220: 113155.

87. D. Song, L. Wang, W. Wang, F. Zheng, J. Tang, S. Wang, C. Zhu, J. Caron, A. Kovács, Z. Liu, D. Mandrus, M. Tian, H. Du, and R. E. Dunin-Borkowski (2020) Robust nature of the chiral spin helix in $CrNb_3S_6$ nanostructures studied by off-axis electron holography. *Phys. Rev. B* 102: 064432.

88. F. Zheng, F. N. Rybakov, A. B. Borisov, D. Song, S. Wang, Z. -A. Li, H. Du, N. S. Kiselev, J. Caron, A. Kovács, M. Tian, Y. Zhang, S. Blügel, and R. E. Dunin-Borkowski (2018) Experimental observation of chiral magnetic bobbers in B20-type FeGe. *Nature Nanotech.* 13: 451-455.

89. M. R. McCartney, & D. J. Smith (2007) Electron holography: Phase imaging with nanometer resolution. *Annu. Rev. Mater. Res. 37*: 729-767.

90. A. Harscher and H. Lichte (1996) Experimental study of amplitude and phase detection limits in electron holography, *Ultramicroscopy* 64: 57-66.

2. Methods

Electron holography is the most important tool in this study to obtain the magnetic phase information, so the principle and the application of electron holography are mainly addressed in this chapter. In addition to electron holography, conventional transmission electron microscopy (TEM) techniques and electron energy-loss spectroscopy (EELS) were utilized to do main work, and accordingly, this chapter also briefly explains the background and functions used in this thesis regarding TEM and EELS.

2.1 Electron microscopy

Electron microscope was initially proposed to overcome the limited image resolution in light microscopes, which is caused by the wavelength of visible light. Louis de Broglie in 1925 [1] first theoretically proposed that the electron had wave-like characteristics with a wavelength substantially less than visible light, which was independently demonstrated by Davisson and Germer [2], and Thompson and Reid in 1927 [3] through electron diffraction experiments demonstrating the wave nature of electron. Henceforth, an electron microscope was proposed and expanded from the first application of electron lenses into a practical reality by Knoll and Ruska in 1932 [4] to the widespread use of TEM by many groups, and when the effect of aberration is disregarded, the resolution (δ) of electron microscope can be represented in terms of the classical Rayleigh criterion []:

$$\delta = \frac{0.61\lambda}{n\,sin\beta}, \qquad (2.1)$$

where λ is the wavelength of electron, n is the refractive index of the medium between electron source and lens, and β is the semi-angle of collection of the magnifying lens. Equation (2.1) provides that the imaging resolution are strongly related to the wavelength of incident electron beams. The wavelength depends on the acceleration voltage of the microscope, and this can be defined by Eq. (2.2). The λ can be expressed in terms of the particle momentum $p(= m_0 v)$ based on de Broglie's ideas of the wave-particle duality.

$$\lambda = \frac{h}{m_0 v}, \qquad (2.2)$$

where m_0, v and h are the rest mass of electron, electron velocity and Planck's constant, respectively. The momentum is imparted to the electron by accelerating it through the potential drop, *i.e.*, the acceleration voltage in microscope *V*, giving it kinetic energy. This potential energy eV equals to the kinetic energy:

$$eV = \frac{m_0 v^2}{2}. \qquad (2.3)$$

With Eqs. (2.2) and (2.3), the wavelength can be rewritten in terms of the acceleration voltage to account for the relativistic effect (*i.e.*, to consider the velocity of light in vacuum, c):

$$\lambda = \frac{h}{[m_0 eU(1+\frac{eU}{2m_0c^2})]^{1/2}}. \qquad (2.4)$$

This relationship provides an important concept that the wavelength of the electrons decreases by increasing the acceleration voltage of microscopy.

Incident electrons produces various interactions with the specimen as shown in Fig. 2.1. For thin specimen, many electrons traverse the specimen, where the traversed electrons can be divided into two groups: (1) elastic scattering and (2) inelastic scattering. The elastic scattered electrons change the direction of the incident electron motion without changing their velocity or energy. Scattering of incident electrons by the nucleus is mostly elastic scattering. Since the mass of the nucleus is much greater than the mass of the electron, when an incident electron moves near the nucleus, it is affected by the nucleus's strong coulomb field. For this reason, the electron only changes the direction of motion without losing energy. Diffracted electrons fall into the category of elastic scattering where high-resolution electron microscopy and TEM imaging modes such as bright-field and dark field image can be utilized. In contrast, the inelastically scattered electrons change their velocity or energy, *i.e.*, loss of the electron energy. The scattering of electrons from extranuclear electrons to incident electrons is primarily inelastic scattering. This is because extranuclear electrons easily obtain energy from the incident

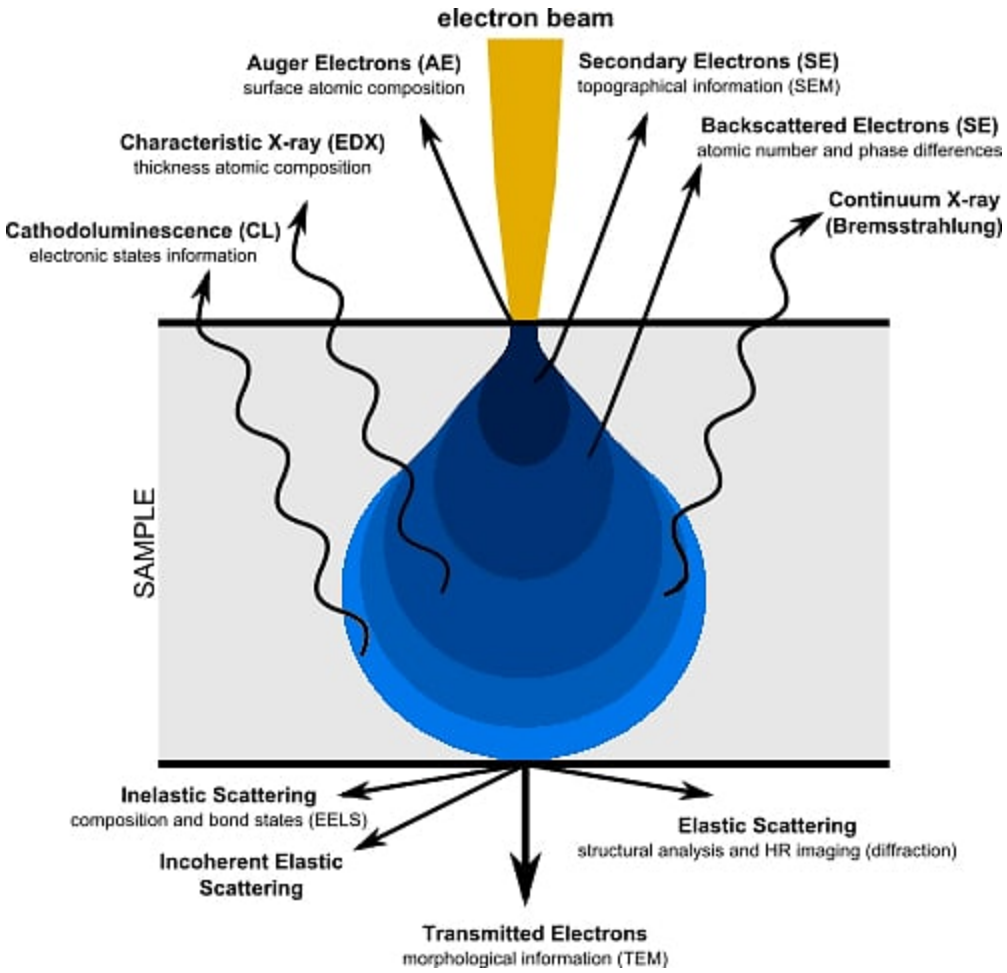

Fig. 2.1 Incident electron beam interaction with the sample [5].

electrons as the direction of incident electrons changes when they with similar properties to incident electrons collide with each other. Those incident electrons that lose energy and slow down their movement produce heat, light, characteristic X-ray, secondary electron signal, etc. Analytical electron microscopy utilizes the feature of inelastic scattering. EELS are most popularly used in analytical electron microscopy by utilizing inelastic electron scattering process.

2.1.1 Transmission electron microscopy

Transmission electron microscopy is a powerful method for characterizing the microstructure, and can be utilized with other analytical instruments such as EELS and energy-dispersive X-ray spectroscopy (EDS) providing useful information of chemical compositions, electronic states, thickness, etc. Electrons emitted from an electron gun, which are accelerated and passed through illumination lenses, are incident on a specimen. After traversing the specimen, the electrons form an image by appropriate action of the objective lens. The enlarged image is formed via image-forming lenses. The final image formed on the fluorescent scree is observed through a window of a viewing chamber, and the image is recorded on photo-film in the camera chamber.

Electrons are emitted from an electron gun located at the top of the microscope column. There are two types of electron gun, *i.e.*, thermionic emission type and field emission type, which determines the electron beam characteristics (*e.g.*, the diameter of electron beam and the width of energy spread). The tungsten (W) hairpin filament of a thermionic emission type electron gun was widely used for a long time, but recently the lanthanum hexaboride (LaB_6) single-crystal filament has been widely used because of its higher brightness than the W filament. However, the field emission gun (FEG) can produce the electrons in higher brightness and higher coherences than the thermionic emission gun. This is because electrons in metals pass through a potential barrier by the tunneling effect and can be emitted from the metal surface when a strong electric field is applied to the metal surface, which is called field emission. The FEG provides approximately 100 times higher electron brightness than thermionic emission gun made with LaB_6 filament and allows for a very small electron source, resulting in high

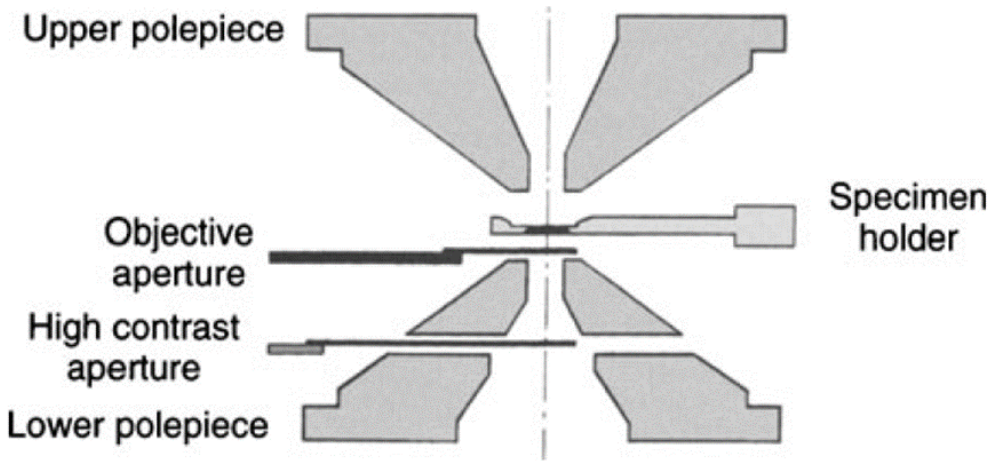

Fig. 2.2 Cross section of polepiece of the objective lens [6].

coherence of electrons. Thanks to the characteristics of FEG, it has been most widely introduced into analytical electron microscopes and makes the electron holography study possible and practically used, as mentioned in Chapter 1. The FEG has two types of guns, *i.e.*, Cold and Thermal field emission gun. The cold FEG (also used in this thesis) uses tungsten emitter with the surface of the (310) plane and works at room temperature without heating. Since the energy spread is small (0.3-0.5 eV), we can obtain high-energy resolution although the emission noise and/or instability of the emission is caused by the contamination of the residual gas on the emitter. This problem requires the regular maintenance that is flashing procedure. Thermal FEG, the other type of FEGs, works at high temperature (1600-1800 K) under a strong electric field by which electrons are emitted that pass through a decreased potential barrier (*i.e.*, Schottky effect). The thermal FEG has the disadvantage of a large energy spread (0.6-0.8 eV) due to the heating of the emitter but provides a stable emission current without the flashing procedure.

Objective lens is the first-stage lens to form an image after the electrons pass through the specimen. The objective lens consists of lens coil, a magnetic circuit (yoke), and a polepiece, which is illustrated in the cross section of a polepiece of the objective lens of Fig. 2.2. A strong magnetic field is generated in a space between the upper and lower polepieces, so the objective lens must be turned off to observe the intrinsic magnetic domains in the specimen, as explained in Chapter 1.3. An objective aperture, located on the back focal plane corresponding to the reciprocal space, selects the electron beam for subsequent imaging, and this function enables us to obtain the images with different contrast (*e.g.*, dark-field imaging by selecting a specific diffracted wave by an objective aperture).

Magnifying the image can be done by changing the focal length (*i.e.*, changing the lens current). Figure 2.3(a) shows the lens system of normal imaging mode. At first, a transmitted image of the specimen illuminated with

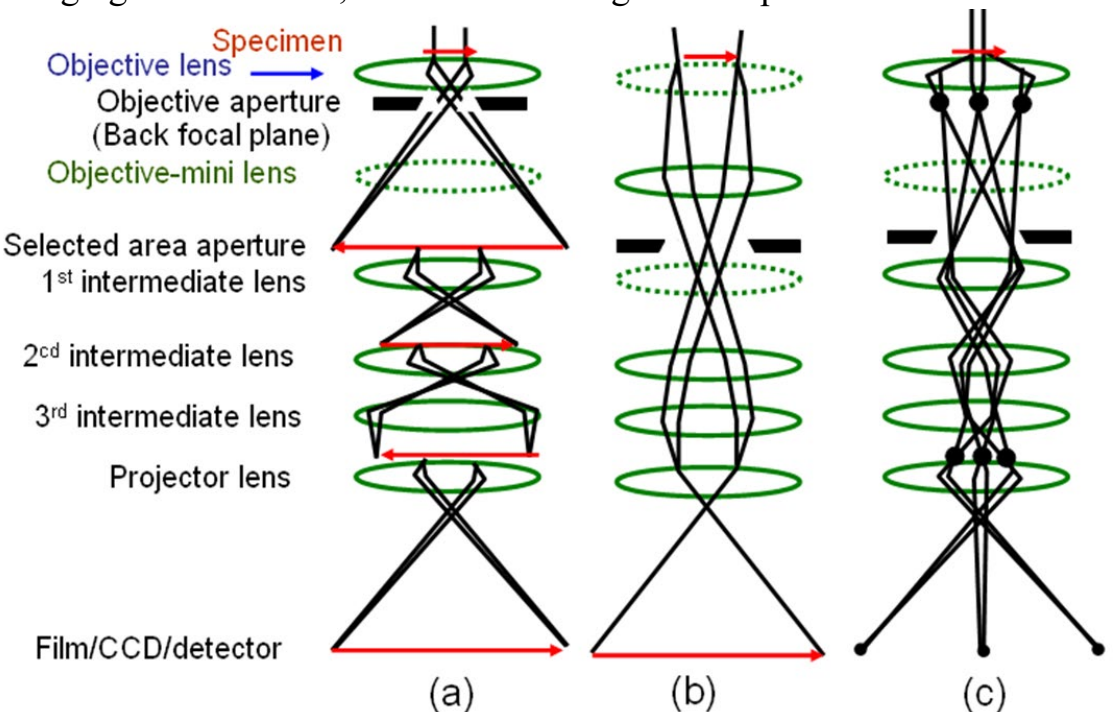

Fig. 2.3 Schematic imaging system in (a)conventional TEM imaging mode, (b) Low-Mag mode and (c) diffraction mode [7].

electrons is magnified by the objective lens. Here, the magnifying lens system includes an objective minilens (OM lens), an intermediate lens, and a projector lens. In typical magnification mode of Fig. 2.3(a), the image is magnified by the first intermediate lens that is adjusted to the image plane of the objective lens in the OM lens turned off. Figure 2.3(b) shows the lens system of imaging mode at low magnification (*i.e.*, Low-Mag mode) with the objective lens turned off. In Low-Mag mode, all the magnifying lens system contributes the formation of image except for the first intermediate lens. On the other hand, Fig. 2.3(c) shows the lens system of diffraction mode, resulting in the electron diffraction pattern. The electron diffraction is an indispensable part of TEM because it provides crystal structure, crystal orientation, lattice spacing and so on. In diffraction mode, the first intermediate lens is adjusted at the back focal plane of the objective lens in the state of the OM lens turned off, so the magnifying lens system magnifies the electron diffraction pattern formed on the back focal plane. The electron diffraction angle 2θ depends on the crystal structure of specimen, which can be given by the Bragg's law:

$$2d_{(hkl)}sin\theta = n\lambda, \qquad (2.5)$$

where $d_{(hkl)}$, n and λ represent the interplanar distance of crystal plane hkl, the order of diffraction (usually n =1 for first order) and the electron wavelength, respectively. The diffracted planes belong to specific zone axis $[UVW]$, which can be defined as the incident direction and follow the Weiss zone law: $hU + kV + lW = 0$. Figure 2.4 (a) shows the electron diffraction

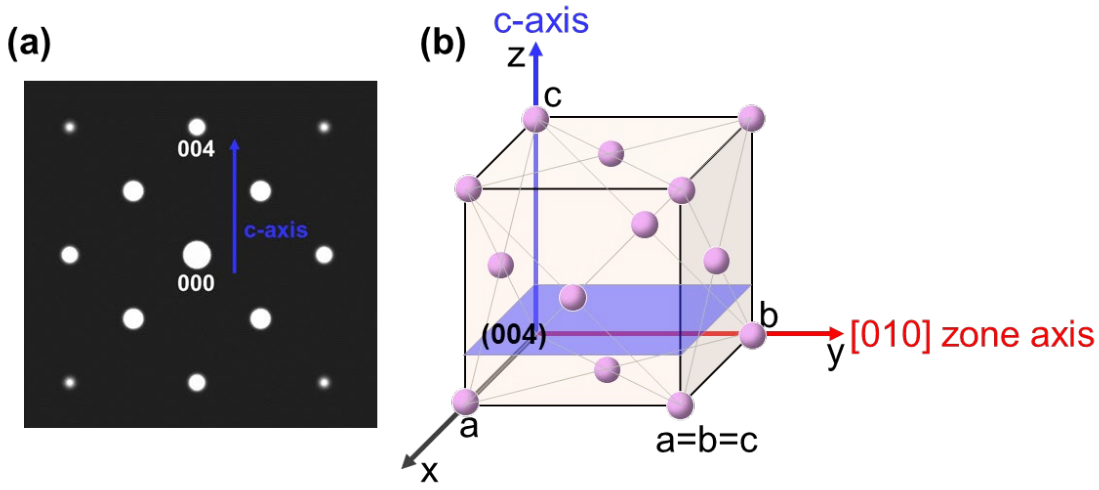

Fig. 2.4 (a) Electron diffraction pattern of Si at the zone axis of [010]. (b) Cubic unit cell of Si

pattern of Si at the zone axis of [010] where the diffracted plans (hkl) are parallel to the zone axis vector and the information crystal orientation can obtained. The direction of c-axis indicated by blue arrows in the electron diffraction pattern of Fig. 2.4(a) approximately corresponds to the real c-axis of Si unit cell in Fig. 2.4(b). In this study, the author calculated the orientation of c-axis of a single crystalline $Nd_2Fe_{14}B$ specimen, and the process to determine the direction of c-axis will be explained in Chapter 5.

2.1.2 Electron energy-loss spectroscopy

As described in the above section, the electrons passing through a specimen can be divided into two groups. One group contains the elastically scattered electrons without energy loss. The other group includes the inelastically scattered electrons, and this inelastic scattering electrons can be observed by using a spectrometer of EELS. Previously, EELS was only effective for elemental analysis for light elements, but was generally considered useless

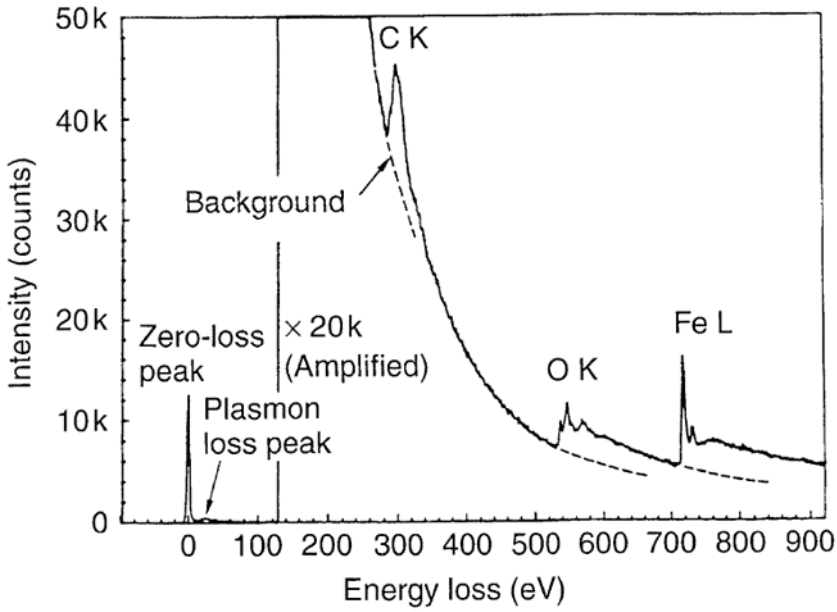

Fig. 2.5 Typical energy-loss spectrum for an iron oxide particle [6].

for quantitative analysis compared to EDS. For high performance of the detector and the development of FEG, the analysis accuracy of EELS was significantly improved, which has attracted many attentions for new applications such as elemental mapping, background subtraction in electron diffraction patterns, and measurement of specimen thickness and chemical states of elements. Representative energy-loss processes and their energy ranges are (1) Lattice vibration (phonon excitation, less than 0.1 eV), (2) Collective excitation of valence electrons (plasmon excitation, less than 30 eV), (3) Interband transition (less than 10 eV), (4) Inner-shell electron excitation (core electron excitation, more than 13 eV), (5) Excitation of free electron (secondary electron emission, less than 50eV), and (6) Bremsstrahlung (emission of continuous X-rays, spectrum background). Figure 2.5 shows a typical energy-loss spectrum (for an iron oxide particle). A sharp peak appears at 0 eV, which is called zero-loss peak, and corresponds to the elastically scattered electrons (both transmitted and diffracted beams).

Near the zero-loss peak, there is a peak that results from the plasmon excitation. In the higher energy-loss region, energy-loss peaks appear due to inner-shall excitation of the elements included in the specimen. The energy values and intensity distribution can be used to identify the elemental composition. Among useful analysis methods by utilizing these energy-loss process, this section mainly deals with the estimation method of specimen thickness, as it will be used in Chapter 5.

The EELS can provide an approximate value of thickness from both crystalline and amorphous specimens by straightforward integration of the EELS spectrum. The intensity of the zero-loss peak I_0 can be expressed with specimen thickness t:

$$I_0 = I_t \exp\left(-\frac{t}{\lambda}\right), \quad (2.6)$$

where I_t is the total intensity of the energy-loss spectrum and λ is the mean free path for inelastic scattering that depends on the collection angle β. For a thin-foil specimen, in general, the plasmon excitation is most probable inelastically scattering, thus the main components of λ can be considered to be due to plasmon excitation. The Eq. (2.6) can be rewritten in terms of specimen thickness *t* as follows:

$$\frac{t}{\lambda} = \ln\frac{I_t}{I_0}. \quad (2.7),$$

which is called log-ratio technique. With Eq. (2.7) this technique provides the information of *t*. If λ is known, the specimen thickness can be obtained. To figure out the λ, Iakoubovskii and Mitsuishi [8] measured the λ with a 200 keV TEM for most of stable elements and their oxides. Malis et. al., [9] proposed an equation allowing for the determination of the λ for the specimen composing of various elements although the collection angle β is necessary:

$$\lambda = \frac{106F(E_o/E_m)}{\ln(2E_o\beta/E_m)}. \qquad (2.8)$$

In this study, the specimen thickness for a thin-foil $Nd_2Fe_{14}B$ specimen was obtained by using the log-ratio method of EELS. However, the λ for the $Nd_2Fe_{14}B$ phase has not been reported. To determine the λ, in place of using Eq. (2.8), a complex analysis was performed through combination of a cross-sectional TEM observation and magnetic field simulation, and this will be discussed in Chapter 5.

2.2 Principle of electron holography

To explain the basic principle of electron holography, Fig. 2.6 shows a schematic cross section of a bar magnet that is magnetized in the *y* direction. The magnet is irradiated by incident electrons propagating in the $-z$ direction. Both the arrows P_0-P and Q_0-Q represent the trajectories of electrons. For simplicity, it is assumed that the points P_0, P, Q_0, and Q are distanced sufficiently from the bar magnet, and there is only negligible

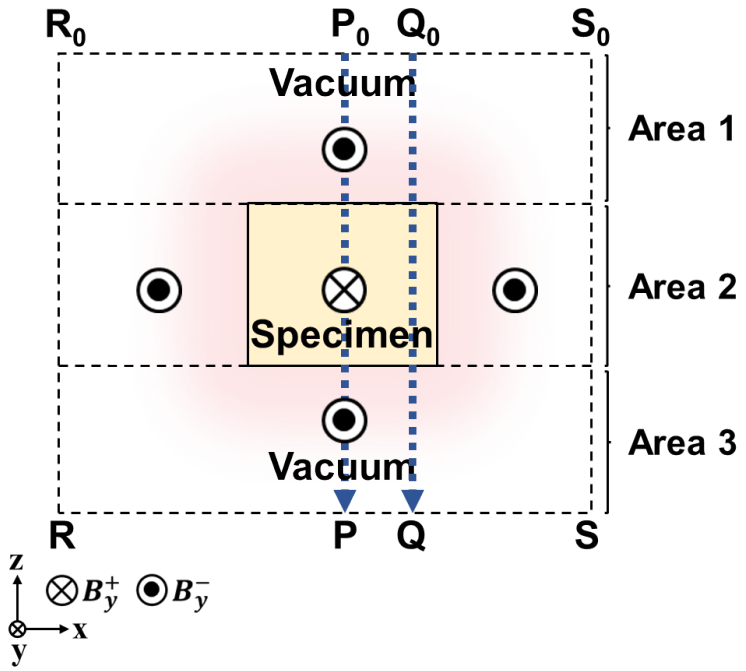

Fig. 2.6 Schematic illustration showing a cross section of a magnetic bar magnetized in the *y* direction. Incident electrons traverse in the $-z$ direction.

magnetic flux density at those points. Regarding the point P below the bar magnet in Fig. 2.6, the phase of the electron wave that has traversed the specimen, *i.e.,* the change in phase between P_0 and P, is expressed by

$$\phi_P = \sigma \int_{P_0}^{P} V(x,y,z)dz - \frac{e}{\hbar}\int_{P_0}^{P} A_z(x,y,z)dz, \qquad (2.9)$$

where σ, e and $\hbar$ are an interaction constant that depends on the acceleration voltage applied to the incident electrons, the elementary charge, and Planck's constant divided by 2π, respectively. $V(x,y,z)$ represents the electrostatic scalar potential. If the electric charging of the specimen is negligible, then this term approximates the mean inner potential of the specimen [10]. $A_z(x,y,z)$ is the z component of the vector potential ($\boldsymbol{A}$)

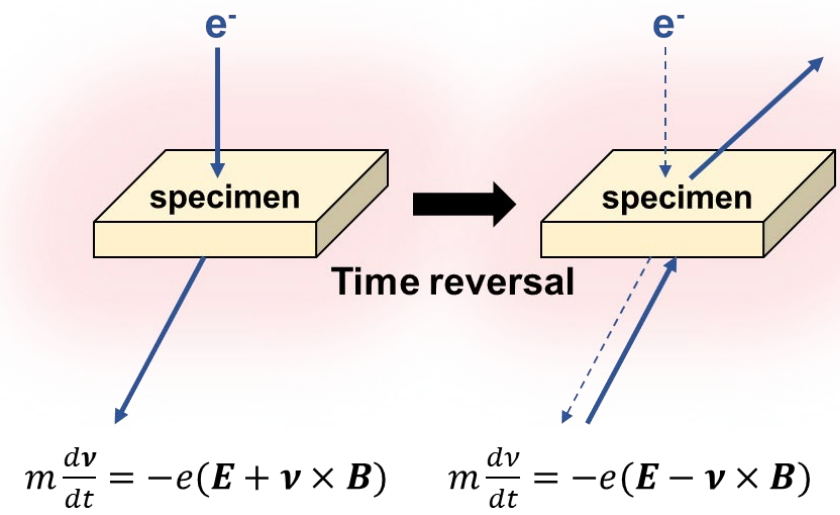

Fig. 2.7 Schematic representation showing the time reversal of electron trajectories in electromagnetic fields [11].

with respect to the magnetic flux density ($\boldsymbol{B}$). Similarly, the phase shift at point Q, *i.e.*, ϕ_Q, can be expressed using the line integral with $V(x, y, z)$ and $A_z(x, y, z)$, as shown in Eq. (2.9).

2.2.1 Phase shift due to magnetic flux density

Note that the phase shift due to $V(x, y, z)$ can be separated from that of $A_z(x, y, z)$ by the method referred to as a time-reversal operation using electron waves [11]. For TEM observations, the time reversal can be attained by flipping the specimen upside down with respect to the incident electrons. These operation remains the electric fields ($\boldsymbol{E}$) contribution to the phase shift (ϕ) unchanged but makes the magnetic field contribution opposite sign. Conceptually, these effects can be understood with reference to the following relationships:

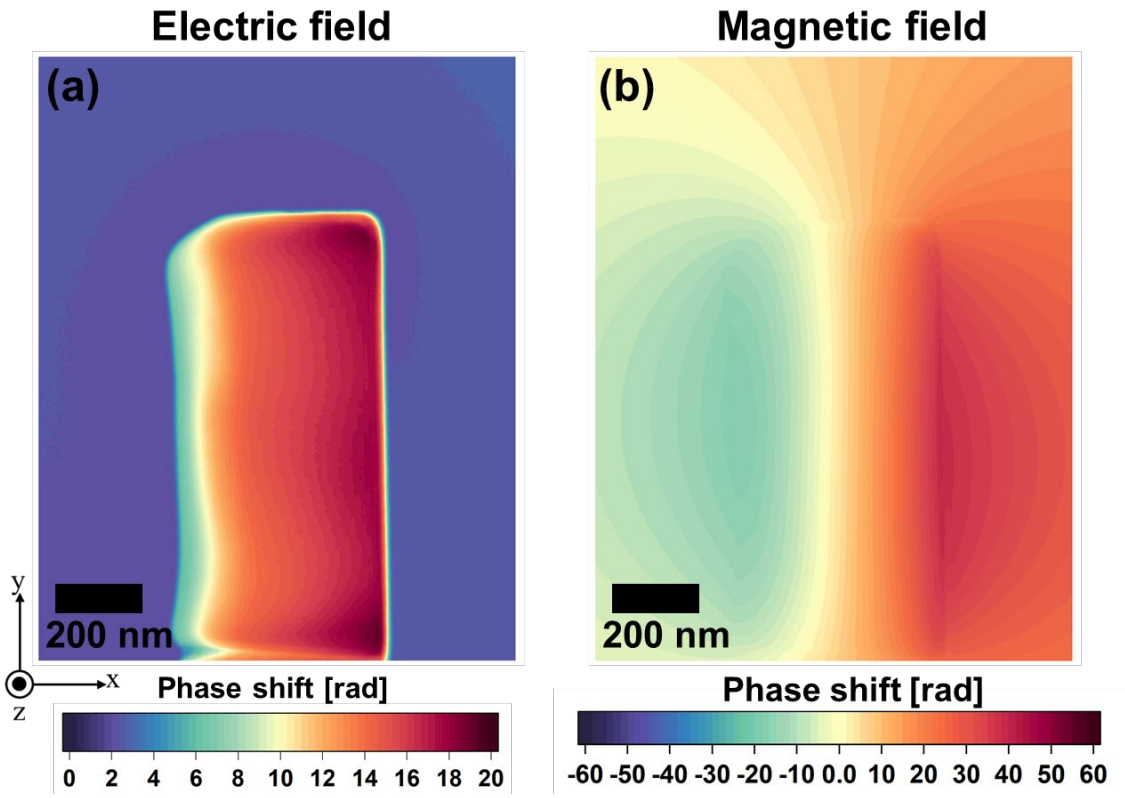

Fig. 2.7 Reconstructed phase images representing the contribution of (a) electric field and (b) magnetic field for a single crystalline $Nd_2Fe_{14}B$ specimen.

$$m\frac{d\boldsymbol{v}}{dt} = -e(\boldsymbol{E} + \boldsymbol{v} \times \boldsymbol{B}) \qquad (2.10)$$

$$m\frac{d\boldsymbol{v}}{dt} = -e(\boldsymbol{E} - \boldsymbol{v} \times \boldsymbol{B}) \qquad (2.11),$$

where t and v stands for the specimen thickness and electron velocity, respectively. Equation (2.11) represents the situation that the electron beam is incident to the specimen along the same trajectory but from the opposite direction, as shown in Fig. 2.7. Therefore, by subtracting the two holograms for the time reversal the phase shift due to the magnetic field only, *i.e.*, the second term of Eq. (2.9), can be obtained, as presented in Fig. 2.8 [separation between the field contributions of Fig. 2.8(a) and the magnetic field

contributions of Fig. 2.8(b) to ϕ]. With regard to the contribution from the magnetic field, the phase shift between the two points P and Q below the specimen in Fig. 2.6 is presented by,

$$\phi_{PQ} = -\frac{e}{\hbar}\int_{Q_0}^{Q} A_z(x,y,z)\,dz + \frac{e}{\hbar}\int_{P_0}^{P} A_z(x,y,z)\,dz. \qquad (2.12)$$

The Stokes' theorem and the relationship $\boldsymbol{B}$ = rot$\boldsymbol{A}$ are used to rewrite the phase shift ϕ_{PQ} of Eq. (2.12) using the surface integral in terms of the y component of the magnetic flux density $B_y(x,y,z)$, resulting in Eq. (2.14):

$$\phi_{PQ} = -\frac{e}{\hbar}\oint_{P_0Q_0QP} A_z\,(x,y,z)\,dxdz \qquad (2.13)$$

$$\phi_{PQ} = -\frac{e}{\hbar}\iint_{P_0Q_0QP} B_y(x,y,z)dxdz, \qquad (2.14)$$

where the surface integral should be performed over the closed area P_0Q_0QP. In what follows in this paper, the phase shift will be calculated with reference to the surface integral using B_y, in place of the line integral using A_z. The reason for adopting the surface integral using B_y instead of the line integral using A_z in this thesis will be discussed in Chapter 3. It should be noted that Eq. (2.14) provides only the relative change in the phase between the measurement point Q and the reference point P. Therefore, when Eq. (2.14) is applied to a phase-shift analysis, the value of the phase at point P is assumed to be zero, so that ϕ_{PQ} simply provides the magnitude of the phase

shift between P and Q. To compare the phase-shift map calculated using Eq. (2.14) with an electron holography observation, the offset (*i.e.,* initial value of the phase) should be determined for the reference point indicated by P. To determine the offset at the reference points, we referred to the values either in a reconstructed phase image determined by experiment (for analysis using the actual specimen) or in the calculations by the line integral using A_z (for analysis using the artificial specimen), and this is discussed in great detail in Chapter 4 and 5.

2.2.2 Process to obtain reconstructed phase image

The phase shift in the object electron wave, which has traversed a specimen can be captured in an electron hologram that comprises interference fringes generated in association with the reference electron wave [12]. This reference wave should be free from phase modulation due to the electromagnetic field of the specimen. Digitized electron hologram can be considered as an interference pattern where the carrier fringes is modulated both in amplitude and frequency. Note that the frequency modulation is caused by the phase shift that includes the information about the electromagnetic fields of the specimen. Therefore, the reconstruction of the electron hologram must be conducted to recover the phase information [13]. Fourier transform (FT) has been commonly used to reconstruct the hologram and reveal the carrier frequency. First of all, the intensity distribution $I(\boldsymbol{r})$ in the hologram with carrier frequency $\boldsymbol{q}$ can be written as [14]

$$I(\boldsymbol{r}) = 1 + A^2(\boldsymbol{r}) + I_{inel}(\boldsymbol{r}) + 2\mu A(\boldsymbol{r})\cos\left(2\pi\boldsymbol{q}\cdot\boldsymbol{r} + \phi(\boldsymbol{r})\right), \qquad (2.15)$$

where μ, $I_{inel}(\boldsymbol{r})$, $A(\boldsymbol{r})$ and $\phi(\boldsymbol{r})$ are the contrast of the fringes (to account for partial coherence), the inelastic (incoherent) background to the hologram, the amplitude and the phase of the image wave that modulate the cosinusoidal fringes, respectively. When the FT is applied to the hologram, Eq. (2.15) changes and consists of three parts:

$$\begin{aligned} \mathrm{FT}\{I(\boldsymbol{r})\} = \mathrm{FT}\{1 + A^2(\boldsymbol{r}) + I_{inel}(\boldsymbol{r})\} \quad & \text{Centre band} \\ +\mu\mathrm{FT}\{A(\boldsymbol{r})e^{\mathrm{i}\phi(r)}\} \otimes \delta(\boldsymbol{q} + \boldsymbol{q}c) \quad & \text{Side band 1} \\ +\mu\mathrm{FT}\{A(\boldsymbol{r})e^{\mathrm{i}\phi(r)}\} \otimes \delta(\boldsymbol{q} - \boldsymbol{q}c) \quad & \text{Side band 2.} \end{aligned} \qquad (2.16)$$

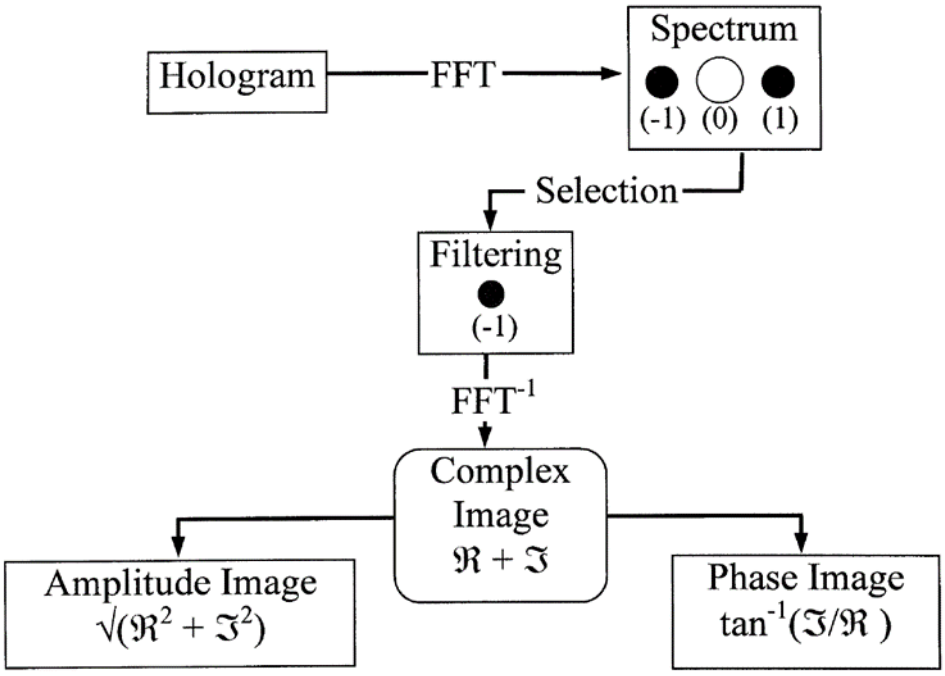

Fig. 2.9 Schematic illustration of the reconstructed process [13].

In Eq. (2.16), the centre band (or autocorrelation) is the FT of a conventional image and the two sidebands at $\boldsymbol{q} \pm \boldsymbol{q}c$ are the parts representing the FTs of the complex image wave that includes the phase information, *i.e.*, $\phi(\boldsymbol{r})$. The following process is to select one of the sidebands, cut it out and move it to the origin of Fourier space. Through an inverse FT with respect to a specific frequency zone (*i.e.*, one of the sidebands), we can recover the real and imaginary parts of the complex image, and hence can obtain the reconstructed phase image. This sequence of processes is schematically presented in Fig. 2.9. Note that finding the precise centre of sideband must be careful as incorrect position induces a phase ramp across the reconstructed phase image. The centre is usually taken to be the pixel in the vicinity of the sideband with the highest intensity in the FT modulus. Although various methods have been reported to overcome this problem [10, 14], the most accurate method (also used in this thesis) is to use the blank hologram (*i.e.*, reference hologram) recorded under identical conditions to the experiment, but not specimen. This method allows for the precise finding the centre because the fringes of blank hologram have not modulated by the object, and the removal of the spurious phase information due to the geometric distortions (caused by the projector system of the microscope like the lenses). After the sideband centre is precisely determined, the region around the sideband must be masked to move it to the origin, where the mask is circular and diffuse at the edges to minimize the abrupt loss of the information at the mask edge. The optimum size of mask depends on the materials [15], in general, the mask size is determined to be 1/3 of the carrier frequency. This represents that the high spatial resolution of the reconstructed phase image can be obtained with higher the frequency maintained over a larger radius,

which suggests importance of the requirement of narrow fringe spacing as possible in the electron hologram. However, narrow fringe spacing can deteriorate the fringe contrast, remaining the problem for the interferometry system, and this will be discussed in great details in Chapter 6. After the inverse FT, in addition, the values in the reconstructed phase image have discontinuities of 2π (*i.e.*, phase jumps) because they are mathematically limited to the interval of $(\pi,\pi]$ although the true phase span an interval larger than 2π. To remove the phase jumps, true phase image determined from the wrapped the discontinuities in the phase, called phase unwrapping, is carried out by the simple method (*i.e.*, a path-dependent method) that is identifying the phase jumps along a row or column of pixels and adding the appropriate integer multiple of 2π to each pixel in the wrapped phase. In practice, more sophisticated algorithms for phase unwrapping including the above algorithm have been suggested [16,17] because the presence of noise weaken the ability to reliably judge the existence of a phase jump. Finally, this process affords a reconstructed phase image, as shown in Fig. 2.7(b), which can be compared with the phase map that is calculated using the surface integral for B_y (or line integral for A_z) as discussed in Chapter 5.

Chapter 2 References

1. L. De Broglie (1925). Recherches sur la théorie des quanta, Paris, 1924 (thèse de physique), *Ann. de Physique 3*: 10-22.

2. C. Davisson, & L. H. Germer (1927) Diffraction of electrons by a crystal of nickel, *Physical review 30*(6): 705.

3. G. P. Thomson, & A. Reid (1927) Diffraction of cathode rays by a thin

film, *Nature 119*(3007): 890-890.

4. M. Knoll, & E. Rusk (1932) Das elektronenmikroskop. *Zeitschrift für physik 78*(5): 318-339.

5. https://www.atriainnovation.com/en/scanning-electron-microscopy-uses/

6. D. B. Williams, & C. B. Carter (1996) The transmission electron microscope, In *Transmission electron microscopy* (pp. 3-17). Springer, Boston, MA.

7. https://www.globalsino.com/EM/page4140.html.

8. K. Iakoubovskii, K. Mitsuishi, Y. Nakayama, & K. Furuya, (2008) Mean free path of inelastic electron scattering in elemental solids and oxides using transmission electron microscopy: Atomic number dependent oscillatory behavior, *Physical Review B 77*(10): 104102.

9. T. Malis, S. C. Cheng, & R. F. Egerton (1988). EELS log-ratio technique for specimen-thickness measurement in the TEM, *Journal of electron microscopy technique 8*(2): 193-200.

10. E. Völkl, L. F. Allard, and D. C. Joy (1999) *Introduction to Electron Holography.* (Kluwer Academic/Plenum Publishers, New York.)

11. A. Tonomura, T. Matsuda, J. Endo, T. Arii, and K. Mihama (1986) Holographic interference electron microscopy for determining specimen magnetic structure and thickness distribution. *Phys. Rev. B* 34: 3397.

12. A. Tonomura (1999) *Electron Holography (2nd ed.).* (Springer, Heidelberg)

13. P. A. Midgley (2001) An introduction to off-axis electron holography. *Micron* 32: 167-184.

14. M. Lehmann, E. Völkl, & F. Lenz (1994) Reconstruction of electron off-axis holograms: a new and fast alternative method, *Ultramicroscopy 54*(2-4): 335-344.

15. K. Ishizuka (1993) Optimized sampling schemes for off-axis holography, *Ultramicroscopy 52*(1): 1-5.

16. N. K. Bambha, J. R. Bickford, & K. K. Klett (2012) *Two-dimensional Phase Unwrapping for Digital Holography*. ARMY RESEARCH LAB ADELPHI MD SENSORS AND ELECTRON DEVICES DIRECTORATE.

17. M. A. Schofield, & Y. Zhu (2002) Fast and Robust Phase Unwrapping Algorithm for Electron Holography, *Microscopy and Microanalysis 8*(S02): 532-533.

3. Method to extract phase information of demagnetization field

3.1 Introduction

Electron holography, an indispensable experimental tool in this study, enables us to observe the magnetic domains [1,2]. However, in principle, electron holography is only sensitive to magnetic flux density (B). More strictly, the phase shift in the incident electron wave is owing to the vector potential $\boldsymbol{A}$, which is related to the magnetic flux by the relationship $\boldsymbol{B}$ = rot $\boldsymbol{A}$. Other useful microscopy and spectroscopy have been used to analyze the local magnetic microstructure [3-7]. For example, X-ray magnetic dichroism (XMCD) [8,9], spin-polarized scanning tunneling microscopy (SP-STM) [10], and micro-SQUID magnetometry [11] are only sensitive magnetization (M), which is complementary functionality to electron holography. Magnetic force microcopy [12] does not provide the information straightforwardly on the near surface distribution of magnetization as it measures the magnetic force between the magnetic moment of the tip and the stray magnetic field (H_s) from the specimen. Among methods that can be used with transmission electron microscopy (TEM), Lorentz microscopy and differential phase contrast (DPC) microscopy are useful methods to reveal the magnetic domain structures [13-15], but they have the same issue for electron holography, i.e., only sensitive to B, which indicates difficulty of extracting the phase information due to demagnetization field H_d (also M) [16].

This chapter pertains to this kind of discussion described above. Specifically, the author proposes a method for determining the phase maps

induced by each component of B (*i.e.*, M and H_s) from electron holography observation and finally extracting phase information of H_d. In this chapter, we shall figure out some technical problem in the phase mapping that was obtained by using the surface integral with B. Namely, we shall discuss not only the successful cases of H_d mapping (as mentioned in the subsequent chapters) but also the unsuccessful cases in which the calculation of phase map was highly distorted due to the incorrect selection of the offset phase shift, as mentioned later in detail. On the other hand, it is commonly accepted that the phase shift of electron wave is induced by A, *i.e.*, using line integral along the incident electron path ($-z$ direction) passing through the specimen (refer to Chapter 2.2). However, in this study, the surface integral using B was employed. To show the correctness in the calculations using surface integral of B, the result was thoroughly compared with the calculation using the line integral of A.

3.2 Proposal of the method to extract demagnetization field using electron holography

The magnetic flux density B can be expressed using M (*i.e.,* magnetic moment *per* unit volume), and the magnetic field H that is comprised of H_s outside of specimen and the H_d inside of specimen:

$$B = \mu_0 M + \mu_0 H = \mu_0 M + \mu_0 H_s + \mu_0 H_d. \quad (3.1)$$

μ_0 stands for the permeability of vacuum. In accordance with Eq. (3.1), we assume that the phase shift $\Delta\phi_B$ due to magnetic flux density, which is determined by electron holography, can be expressed using the three contributions:

$$\Delta\phi_B = \Delta\phi_M + \Delta\phi_{H_s} + \Delta\phi_{H_d}, \qquad (3.2)$$

where $\Delta\phi_M$, $\Delta\phi_{H_s}$, and $\Delta\phi_{H_d}$ represent the phase shift due to magnetization, the stray magnetic field, and the demagnetization field, respectively. It is noted that the material parameter $Q(= K/K_d)$ is 4.5 in the $Nd_2Fe_{14}B$ phase, where K and K_d represent the effective anisotropy constant (assumed to be equal to magnetocrystalline anisotropy $K_u = 4.5 \times 10^6$ J m^{-3}) and the stray field energy coefficient ($K_d = \frac{\mu_0}{2} {M_s}^2 =$

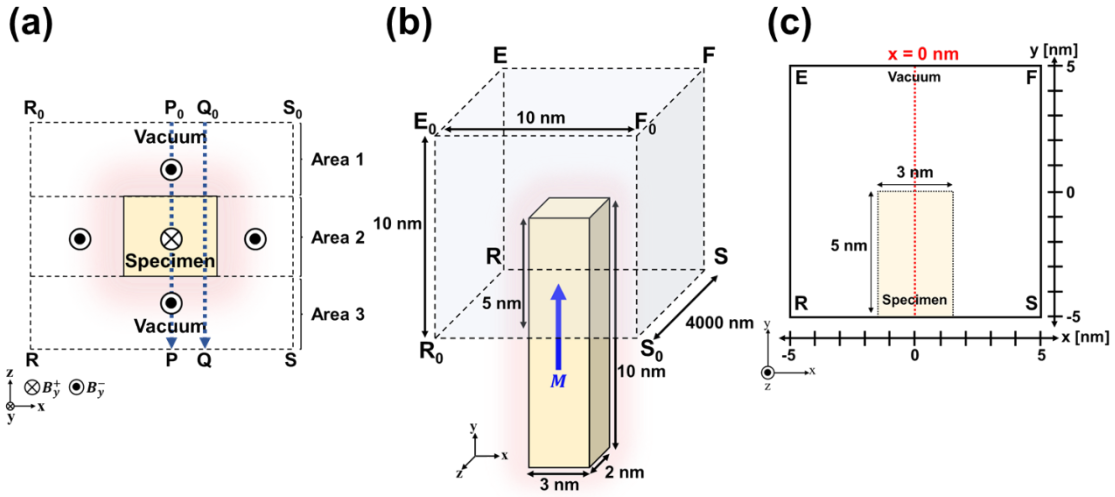

Fig. 3.1. schematic representations describing the principle and conditions of phase shift calculations using an artificial $Nd_2Fe_{14}B$ bar magnet. (a) Cross section of specimen magnetized in the y direction. Incident electrons traverse in the $-z$ direction. (b) Parallelepiped specimen with a size of 3×2×10 nm^3, and the cuboidal region (E, F, F$_0$, E$_0$, R, S, S$_0$, and R$_0$) irradiated by the object electron wave. (c) The area in which the phase images are revealed such as shown in Fig. 3.3.

1.0×10^6 J m^{-3}), respectively [17-19]. The condition $Q > 1$ means that the magnetocrystalline anisotropy dominates the magnetic domain structure in a $Nd_2Fe_{14}B$ specimen [19]. Therefore, it is reasonable to consider that the crystal grain is, in principle, magnetized along the *c*-axis (easy magnetization axis) of the $Nd_2Fe_{14}B$ lattice. For the analysis using the experimental data, as shown in the subsequent chapter, both the direction of the *c*-axis and the thickness variation of the specimen could be determined from TEM observations. With reference to the cross-sectional view in the artificial bar magnet of $Nd_2Fe_{14}B$, as shown in Fig. 3.1(a) (identical to Fig. 2.6), *M* exists only in the area 2 (*i.e.,* middle area in P_0Q_0QP). Therefore, we assume that the phase shift $\Delta\phi_M$ can be calculated using the surface integral for the area 2:

$$\Delta\phi_M = -\frac{e}{\hbar}\iint_{area2}\mu_0 M^y(x,y,z)dxdz, \qquad (3.3)$$

where M^y represents the *y* component of magnetization: refer to the *x*-*y*-*z* coordinate system in Fig. 3.1. The surface integral should be performed over the entire cross-sectional area of the specimen. Note that Eq. (3.3) determines the phase shift due to magnetization, which is only one component that comprises $\Delta\phi_B$ observed in the P-Q line of Fig. 3.1(a). As a result of the surface integral to determine $\Delta\phi_M$, we obtain another phase map that represents $\Delta\phi_{H_s} + \Delta\phi_{H_d}$, which is given by the subtraction of $\Delta\phi_M$ from $\Delta\phi_B$:

$$\Delta\phi_{H_s} + \Delta\phi_{H_d} = \Delta\phi_B - \Delta\phi_M. \quad (3.4)$$

In regard to the $Nd_2Fe_{14}B$ magnet, the residual phase map ($\Delta\phi_{H_s} + \Delta\phi_{H_d}$) by itself provides useful information on the demagnetization field within the specimen, as demonstrated in this chapter as well as in Chapter 4. However, for comprehensive studies on H_d, the contribution from H_s (superposed to the phase map of $\Delta\phi_{H_s} + \Delta\phi_{H_d}$) should be reduced. For this purpose, in this study, the H_s was calculated in three dimensions with reference to the specimen shape, the specimen thickness, and the orientation of the *c*-axis in the $Nd_2Fe_{14}B$ crystal, using the commercial code ELF/MAGIC (ELF Corp.). After the calculation of H_s, the phase shift $\Delta\phi_{H_s}$ can be determined by the surface integrals for the area outside of the specimen [*i.e.,* both area 1 and area 3 in P_0Q_0QP as shown in Fig. 3.1(a)] as presented in Eq. (3.5),

$$\Delta\phi_{H_s} = -\frac{e}{\hbar}\iint_{outside}\mu_0 H_s^y(x,y,z)dxdz, \quad (3.5)$$

where H_s^y represents the y component of the stray magnetic field. As a result of the surface integrals of Eqs. (3.3) and (3.5), the phase shift due to demagnetization field can be determined by the subtraction expressed by

$$\Delta\phi_{H_d} = \Delta\phi_B - \Delta\phi_M - \Delta\phi_{H_s}. \quad (3.6)$$

The usefulness of this method will be discussed in both Chapters 4 and 5 through applications to an artificial bar magnet and a real thin-foil specimen of the $Nd_2Fe_{14}B$ phase, respectively. However, various trials and errors have been made to obtain the appropriate phase map of $\Delta\phi_{H_d}$ from phase images, which is discussed in the next section.

3.3 Simulations

3.3.1 Calculations of three-dimensional magnetic field for $Nd_2Fe_{14}B$ specimen

To calculate the phase shift, an artificial $Nd_2Fe_{14}B$ bar magnet was referred, as illustrated in Fig. 3.1(b). The size of the parallelepiped specimen is 3 nm in the *x* direction, 10 nm in the *y* direction (*i.e.*, the long axis of the bar magnet), and 2 nm in the z direction. The specimen is magnetized in the *y* direction, as indicated by the blue arrow, with the saturation magnetization $\mu_o M \approx 1.6$ T. As shown in Fig. 3.1(b), the small bar magnet was addressed in this simulation, since it reduced the calculation time about the three-dimensional magnetic field and the repetition of surface integral to determine the phase shift. The aspect ratio (*i.e.,* the length in the *y* direction divided by that in the *x* direction) can be an essential factor for the discussion about the demagnetization field, and the results affected by the aspect ratio will be discussed in Chapter 4. To obtain phase maps, the cuboidal region ($10\times4000\times10$ nm^3) indicated by the letters E, F, F_0, E_0, R, S, S_0, and R_0 was assumed to be irradiated by the object electron wave: refer to Fig. 3.1(b). The electron wave traverses in the $-z$ direction. Figure 3.1(c) represents an area

in the *x*-*y* plane (corresponding to the area EFSR), for which the phase contour maps, such as Figs. 3.3 (a) and (c), are presented.

3.3.2 Calculations of vector potential using magnetization

From the law of Biot- Savart, $\boldsymbol{B}$ can be written down in general form for a current density $\boldsymbol{J}(\boldsymbol{r}')$ [20]:

$$\boldsymbol{B}(\boldsymbol{r}) = \frac{\mu_0}{4\pi}\int \boldsymbol{J}(\boldsymbol{r}') \times \frac{\boldsymbol{r}-\boldsymbol{r}'}{|\boldsymbol{r}-\boldsymbol{r}'|^3} d^3\boldsymbol{r}', \quad (3.7)$$

Where $\boldsymbol{J}$ stands for the current density. In the magnetostatic state, we know that in terms of the vector potential any $\boldsymbol{B} = \nabla \times \boldsymbol{A}$ (from now on, rot is denoted by ∇) has zero divergence and are generated by steady currents (*i.e.*, Ampère's law):

$$\nabla \cdot \boldsymbol{B} = 0, \quad (3.8)$$

$$\nabla \times \boldsymbol{B} = \mu_0 \boldsymbol{J}, \quad (3.9)$$

From Eq. (3.9) the general form of $\boldsymbol{A}$ can be expressed by

$$\boldsymbol{A}(\boldsymbol{r}) = \frac{\mu_0}{4\pi}\int \frac{\boldsymbol{J}(\boldsymbol{r}')}{|\boldsymbol{r}-\boldsymbol{r}'|} d^3\boldsymbol{r}' + \nabla\boldsymbol{\psi}(\boldsymbol{r}). \quad (3.10)$$

The added gradient of an arbitrary scalar function $\boldsymbol{\psi}$ shows that for a given $\boldsymbol{B}$ the vector potential can be freely transformed according to $\boldsymbol{A} \rightarrow \boldsymbol{A} + \nabla\boldsymbol{\psi}$, which is called a gauge transformation. The transformations on $\boldsymbol{A}$ are possible because it does not affect the magnetic field that is specified as the curl of $\boldsymbol{A}$. The freedom of gauge transformations (*i.e.*, freedom to add a constant to a scalar potential) allows us to make the divergence of $\boldsymbol{A}$ have any convenient functional form we desire. On the other hand, the Ampère Law of Eq. (3.9) can be substituted into a second-order differential equation using $\boldsymbol{A}$:

$$\mu_0 \boldsymbol{J} = \nabla \times (\nabla \times \boldsymbol{A})$$
$$= \nabla(\nabla \cdot \mathbf{A}) - \nabla^2 \boldsymbol{A}. \qquad (3.11)$$

The convenience choice of the gauge for $\boldsymbol{A}$ can be exploited to make the equation be simple as soon as possible, and we find

$$\nabla \cdot \boldsymbol{A} = 0. \qquad (3.12)$$

This particular choice is known as the Coulomb gauge. Then, the left term of Eq. (3.11) vanishes, and each component of the vector potential satisfies the Poisson equation,

$$\nabla^2 \boldsymbol{A} = -\mu_0 \boldsymbol{J}. \qquad (3.13)$$

From the electrostatic theory, the solution for $\boldsymbol{A}$ in infinite space can be rewritten as Eq. (3.10) having $\boldsymbol{\psi}$=constant**:**

$$\boldsymbol{A}(\boldsymbol{r}) = \frac{\mu_0}{4\pi} \int \frac{\boldsymbol{J}(\boldsymbol{r}')}{|\boldsymbol{r}-\boldsymbol{r}'|} d^3\boldsymbol{r}'. \qquad (3.14)$$

For the above equations, we have assumed that the current density was completely known function of position, in macroscopic problems, this is often not true. Atoms of matter have electrons that give rise to effective atomic currents, the current density of which is a rapidly fluctuating quantity. Only its average over macroscopic volume is relevant or known. Also, the atomic electrons contribute intrinsic magnetic moments in addition to the magnetic moments of orbital motion. All these moments can originate dipole fields that vary appreciably on the atomic scale of dimensions. The number of molecules or atoms per unit volume each with its molecular magnetic moment m_i gives rise to an average magnetic moment density (*i.e.,* $\boldsymbol{M}$). For bulk magnetization, we suppose that there is $\boldsymbol{J}$ from the flow of free charge in the medium. Then the vector potential from an infinitesimal volume $d^3\boldsymbol{r}'$ can be written as the integral over all space,

$$\boldsymbol{A}(\boldsymbol{r}) = \frac{\mu_0}{4\pi}\int\left[\frac{\boldsymbol{J}(\boldsymbol{r}')}{|\boldsymbol{r}-\boldsymbol{r}'|} + \frac{\boldsymbol{M}(\boldsymbol{r}')\times(\boldsymbol{r}-\boldsymbol{r}')}{|\boldsymbol{r}-\boldsymbol{r}'|^3}\right] d^3\boldsymbol{r}'. \qquad (3.15)$$

The second term of Eq. (3.15) represents the magnetic dipole's contribution. For the hard magnet, *i.e.*, *M* given and $\boldsymbol{J}$=0, the solution for vector potential can be

$$\boldsymbol{A}(\boldsymbol{r}) = \frac{\mu_0}{4\pi}\int\frac{\boldsymbol{M}(\boldsymbol{r}')\times(\boldsymbol{r}-\boldsymbol{r}')}{|\boldsymbol{r}-\boldsymbol{r}'|^3} d^3\boldsymbol{r}'. \qquad (3.16)$$

Therefore, the *z* component of vector potential (A_z), which in principle contribute to the phase shift of incident electron, could be calculated from *M*

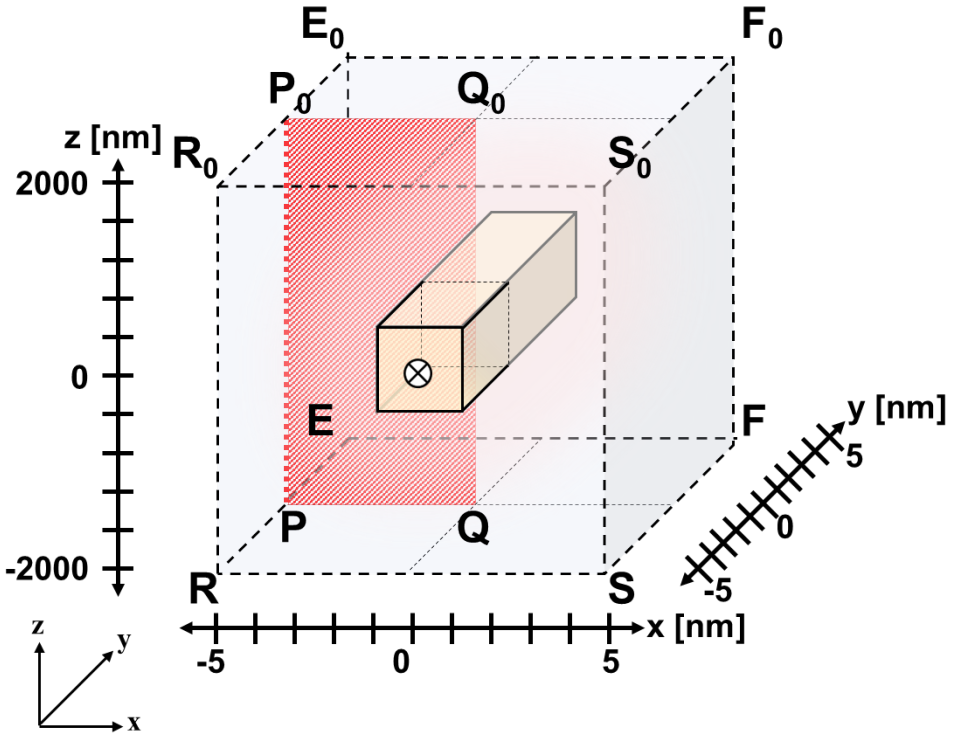

Fig. 3.2. Schematic illustration representing the process of surface integral performed for the area P_0Q_0QP. The start positions of surface integral are fixed as P_0 (-5, y_0, 2000) and P (-5, y_0, -2000).

with reference to Eq. (3.16), and phase image due to A_z is presented in the next section.

3.4 Remarks in phase mapping with the surface integral of *B*

3.4.1 The offset in phase shift

In this study, to calculate the phase shift due to magnetic flux density, the surface integral was performed for the hatched area in Fig. 3.2, closed by the four points P_0 (-5, y_0, 2000), Q_0 (x_0, y_0, 2000), Q (x_0, y_0, -2000), and P (-5, y_0, -2000). For one value of y_0, the positions of P_0 and P are fixed at the coordinates (-5, y_0, 2000) and (-5, y_0, -2000), respectively, while the positions of Q_0 and Q are variable over the range $-5\ \text{nm} \leq x_0 \leq 5\ \text{nm}$. Repeating the surface integral over this range determines the phase shift in the line that connects the two terminal points of Q, *i.e.*, Q (-5, y_0, -2000) and Q (5, y_0, -2000). Subsequently, the surface integral should be performed for a different value of y_0, so that the phase-shift plot can be obtained in another line that connects the two terminal points of Q (-5, y_0, -2000) and Q (5, y_0, -2000), which shows a different value of y_0. Therefore, the y_0 series of the phase-shift plot ($-5\ \text{nm} \leq y_0 \leq 5\ \text{nm}$) results in a two-dimensional map of the phase-shift in the *x*-*y* plane (*i.e.,* phase image) that represents $\Delta\phi_B$, as shown in Fig. 3.3(a). The magnitude and sense (increase or decrease) of the phase shift is indicated by colors, with reference to a color bar, such as that shown in Figs. 3.3 (a) and (b). (The extent of the phase shift shown in the color bar is small because of the small volume of the specimen.) However, this chapter mainly deals with the phase image from the methodological point of view of extracting the phase information of H_d, and

details about the description of the phase images, such as the sense and magnitude of phase gradient, will be discussed in Chapter 4. The position of the specimen edges is indicated by the gray lines in Figs. 3.3(a) and (c). Note that Fig. 3.3(c) represents a true phase map (*i.e.*, a reasonable calculation of

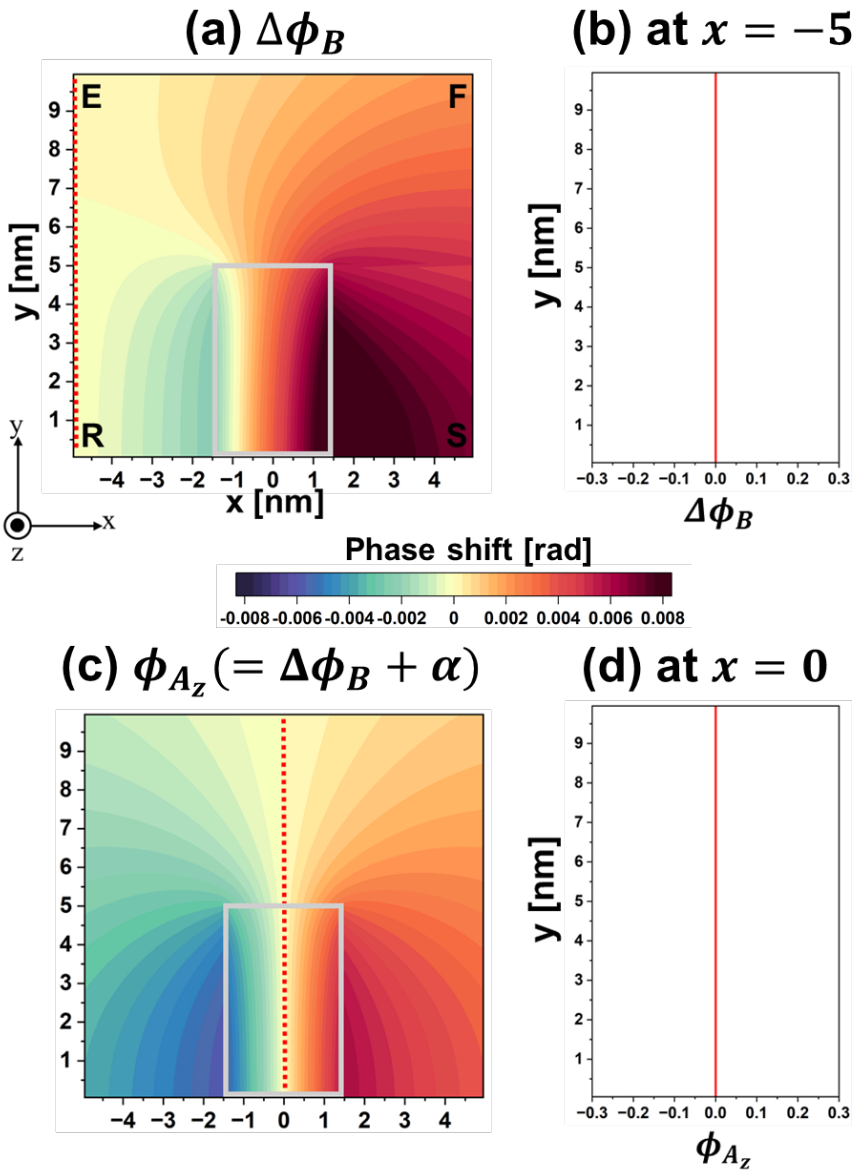

Fig. 3.3 Technical problem of the surface integral employed in the method. (a) Phase map using the surface integral for *B*. The surface integral started from $x = -5$. (b) Line profile of phase shift $\Delta\phi_B$ at $x = -5$. (c) Phase map using the line integral for *A*, showing the true plots of phase shift. (d) Line profile of phase shift ϕ_{A_z} at $x = 0$.

$\Delta\phi_B$ obtained by using a vector potential *A*, as mentioned later in detail), which is identical to an electron holography observation.

In the actual electron holography observation, the phase contours approximate the distribution of magnetic flux lines [2]. However, the phase image of $\Delta\phi_B$ [*i.e.*, calculation using the surface integral as shown in Fig. 3.3(a)] has asymmetric contour lines, unlike a phase image of Fig. 3.3(c). Here the result of Fig. 3.3(c) was obtained by the line integral using the vector potential *A* (*i.e.*, referred to as the phase map ϕ_{A_z}), approximating a true distribution of magnetic flux lines that is highly symmetric with reference to the long axis of the bar magnet. Figure 3.3(b) and (d) shows plots of phase shift measured along red dotted lines in Fig. 3.3(a) and (c), respectively. In reality, the symmetric shape of the specimen illustrated in Fig. 3.1 makes the phase shift zero at $x = 0$, as shown in Figs. 3.3(c) and (d). In Fig. 3.3(a), however, the $\Delta\phi_B$ plots with zero value are located along a line of $x = -5$. This result can be understood through the equation of the surface integral expressed using the summation operator under the coordinates system where *y* is fixed as one value:

$$\Delta\phi_B = -\frac{e}{\hbar} \cdot \lim_{\Delta x_i, \Delta z_k \to 0} \sum_{i=1}^{m} \sum_{k=1}^{n} B_y(x_i, z_k)\ \Delta x_i\ \Delta z_k. \qquad (3.17)$$

The surface integral should be zero (*i.e.*, Δx=0) at the start points of the calculations using Eq. (3.17), *i.e.*, the reference points of P_0 and P in Fig. 3.2. This means that the initial phase shift (*i.e.*, offset of the phase shift) for all the reference points is zero when the phase map is calculated by using the

surface integral of B. A red dotted line in Fig. 3.3(a) indicates the trace of reference points of P_0 and P in Fig. 3.2. The values of $\Delta\phi_B$ plots along the red dotted line are 0, as shown in Fig. 3.3(b). To avoid the undesired asymmetric phase distribution as shown in Fig. 3.3(a), we need the offset of phase shift (*i.e.*, the initial values of the surface integral) that is consistent with the experimental data. For this purpose, regarding the evaluation of the artificial bar magnet, the author referred to the calculations using the vector potential A (*i.e.*, the phase shift ϕ_{A_z}). This compensates the offsets in $\Delta\phi_B$ by adding $\alpha(=\phi_{Az}-\Delta\phi_B)$ to $\Delta\phi_B$, *i.e.*, $\Delta\phi_B+\alpha$, resulting in symmetric phase image identical to Fig. 3.3(c).

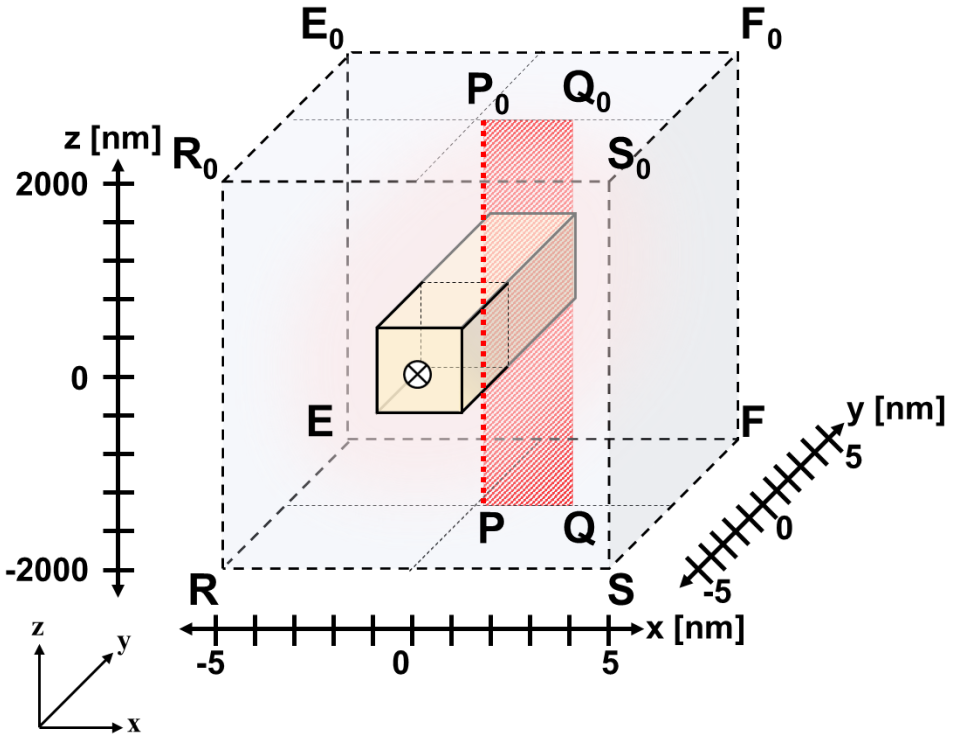

Fig. 3.4 Schematic illustration representing the process of surface integral for P_0Q_0QP with different reference points, *i.e.*, P_0 (0.05, y_0, 2000) and P (0.05, y_0, -2000).

3.4.2 Phase gap and asymmetric phase image

The start points of the surface integral should be carefully determined because of the offset in phase shift, as discussed in the above section. For phase images of $\Delta\phi_M$ and $\Delta\phi_{H_s}$, in this subsection, we refer to the coordinates of the reference points P_0 (0.05, y_0, 2000) and P (0.05, y_0, 2000), *i.e.*, the start points of the integral deviated from an equiphase line that means a line of $x = 0$ along which $\Delta\phi_{A_Z} = 0$ [see the red dotted line in Fig. 3.3(c)], which is presented in Fig. 3.4. Other conditions (the coordinates and range of Q_0 and Q points) and the procedure of the surface integral are the same as described in subsection 3.4.1. Using Eq. 3.3 in accordance with the procedure of the surface integral, Fig. 3.5(a) shows the phase map representing $\Delta\phi_M$. The area shown in Fig. 3.5(a) is corresponding to EFSR area in Fig. 3.4. Then, as described in Eq. 3.4, the subtracting $\Delta\phi_M$ in Fig. 3.5(a) from the reasonable $\Delta\phi_B$(=$\Delta\phi_B + \alpha$) in Fig. 3.3(c) was carried out, and this result is shown in Fig. 3.5(b), *i.e.*, a phase map representing $\Delta\phi_{H_s} + \Delta\phi_{H_d}$. The phase map of Fig. 3.5(b) has phase gaps, as indicated by the red arrow, which appears to occur in the process using the surface integral. One sources of the gap is attributed to the subtraction of phase the calculations of phase images ($\Delta\phi_B - \Delta\phi_M$), which producing such as a horizontal line along the interface between specimen and vacuum. Another phase gap in the *y* direction indicated by the yellow circle was found, such as fluctuation of contour lines shown in the enlargement in Fig. 3.5(b). The phase fluctuation appeared to have been generated along the near edge of the specimen in the *y* direction. Considering the locations of the fluctuation, one cause could be assumed with reference to the calculations of magnetic fields in the *x*-*y*-*z* coordinate system (*i.e.*, three-dimensional distribution of *B*, *M* and H_s): that

is, absent plots of phase shift at and/or very close to the specimen edges in the *y* direction. To avoid this defect, the plots in phase shift are revealed mainly within the specimen area [refer to the area closed by the grey lines in Figs. 3.3 (a) and (c)] by trimming the interface of specimen, and the results of applying this operation will be presented in Chapter 4.

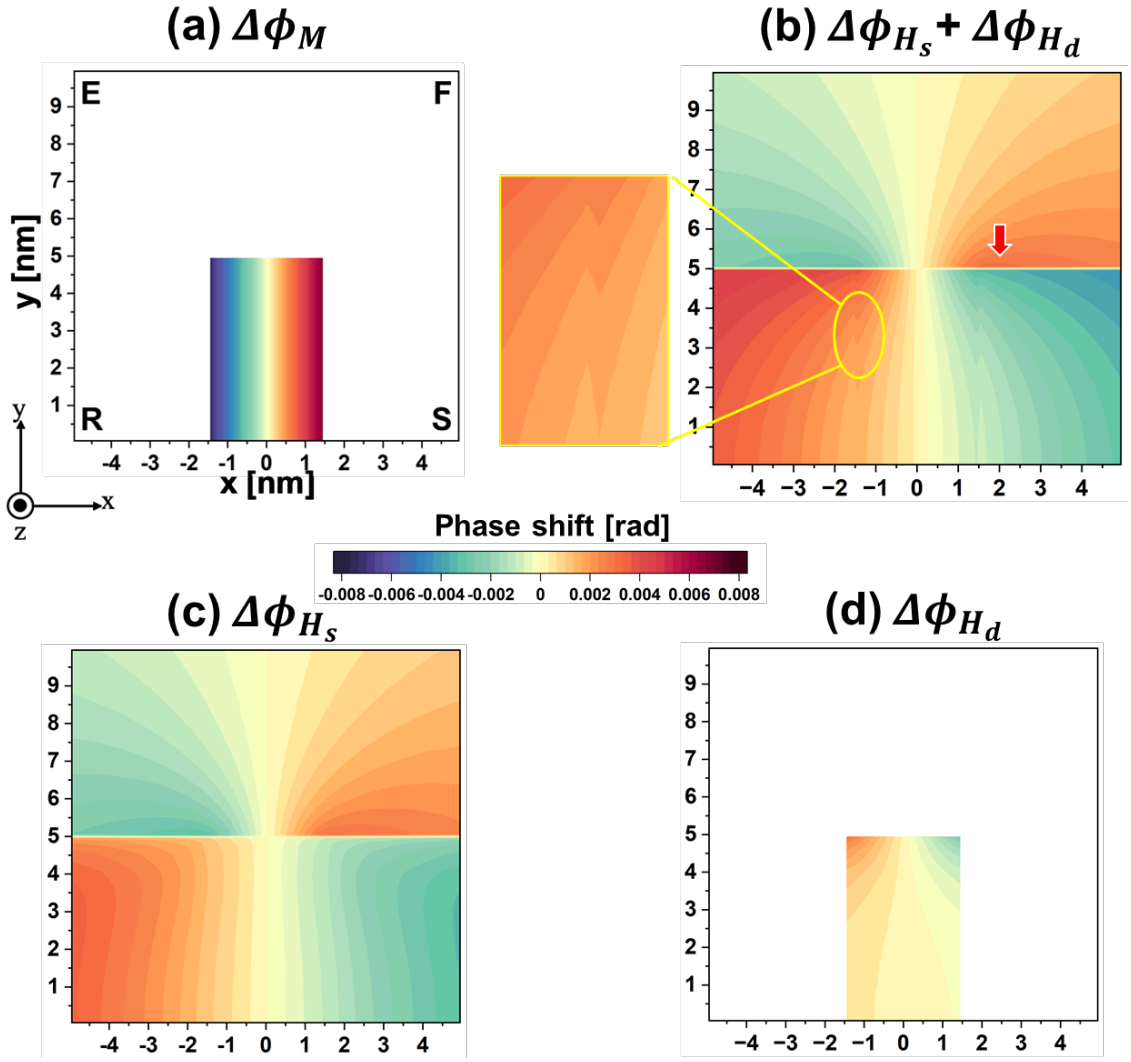

Fig. 3.5 Phase images having phase gaps and asymmetry derived the technical problem of the method. (a) Phase map related to $\Delta\phi_M$. The area in (a) corresponding to EFSR in Fig. 3.4. (b) Phase map related to $\Delta\phi_{H_s}+\Delta\phi_{H_d}$ by subtracting of (a)$\Delta\phi_M$ from $\Delta\phi_B$ of Fig. 3.3(c). The red arrow and yellow lines indicate the phase gaps. (c) Phase map related to $\Delta\phi_{H_s}$. (d) Phase map related to $\Delta\phi_{H_d}$ by removal of (c)$\Delta\phi_{H_s}$ from (b)$\Delta\phi_{H_s}+\Delta\phi_{H_d}$. The asymmetrical distribution of $\Delta\phi_{H_d}$ plots shown in (d).

Phase map of Fig. 3.5(c) representing $\Delta\phi_{H_s}$ could be obtained by using Eq. (3.5). To obtain phase information of $\Delta\phi_{H_d}$, the phase map of Fig. 3.5(c) (*i.e.*, $\Delta\phi_{H_s}$) was subtracted from the phase image of Fig. 3.5(b) (*i.e.*, $\Delta\phi_{H_s} + \Delta\phi_{H_d}$), expressed as Eq. (3.6). The subtraction provides the phase map representing $\Delta\phi_{H_d}$, as shown in Fig. 3.5(d). Note that the distribution of $\Delta\phi_{H_d}$ plots shows the asymmetric contour lines, which could be considered as incorrect when referring to the effect of the specimen shape on H_d (*i.e.*, fully symmetrical rectangular specimen with the long axis). This inappropriate H_d map is highly related to the offset of phase shift. As mentioned in the process of surface integral, the reference points of P_0 (0.05, y_0, 2000) and P (0.05, y_0, 2000) were not completely placed on the equiphase line of $\phi_{A_z} = 0$ [Fig. 3.3(c)], which represents the true distribution of phase shift obtained from the artificial, parallelepiped $Nd_2Fe_{14}B$ specimen. In other words, the *x* coordinate value of the reference points is 0.005, but that of the equiphase line is 0, which induced the incorrect offset value for $\Delta\phi_M$ and $\Delta\phi_{H_s}$. This problem indicates the necessity for the modification of the reference points (*i.e.*, the *x* coordinate of P_0 and P is 0). The H_d map affected by this changed environment of surface integral will be addressed in the subsequent chapter.

3.5 Summary

This chapter proposed a new method that allows for extractions the phase information about the demagnetization field from electron holography observations. $\Delta\phi_M$ and $\Delta\phi_{H_s}$ can be determined using the surface integral for M and H_s, respectively, for which three-dimensional distribution of

magnetic field is calculated with reference to the specimen shape, the *c*-axis and thickness of the specimen by TEM observations. However, the method using the surface integral caused a critical problem that is an initial value of phase shift (*i.e.*, the offset of phase shift) become zero, which led to the distorted distribution of $\Delta\phi_B$ plots in the phase map representing *B*. This problem could be avoided by compensating for the offset of phase shift, as referring to the calculations using vector potential (*i.e.*, $\Delta\phi_{A_z}$). Furthermore, the improper offset of phase shift $\Delta\phi_M$ and $\Delta\phi_{H_s}$ affected the phase map related to H_d, and this indicated the essential with regard to the correct consideration of the offset in phase shift for a reasonable phase map of $\Delta\phi_{H_d}$.

Chapter 3 References

1. E. Völkl, L. F. Allard, and D. C. Joy (1999) *Introduction to Electron Holography.* (Kluwer Academic/Plenum Publishers, New York.)

2. A. Tonomura (1999) *Electron Holography (2nd ed.).* (Springer, Heidelberg)

3. S. Yamamoto, M. Yonemura, T. Wakita, K. Fukumoto, T. Nakamura, T. Kinoshita, Y. Watanabe, F. Z. Guo, M. Sato, T. Terai, and T. Kakeshita (2008) Magnetic-domain structure analysis of Nd-Fe-B sintered magnets using XMCD-PEEM technique. *Mater. Trans.* 49:2354-2359

4. U. Schlickum, W. Wulfhekel, and J. Kirschner (2003) Spin-polarized scanning tunneling microscope for imaging the in-plane magnetization. *Appl. Phys. Lett.* 83:2016-2018

5. M. Pratzer, H. J. Elmers, M. Bode, O. Pietzsch, A. Kubetzka, and R. Wiesendanger (2001) Atomic-scale magnetic domain walls in quasi-one-dimensional Fe nanostripes. *Phys. Rev. Lett.* 87:127201

6. W. Wernsdorfer, B. Doudin, D. Mailly, K. Hasselbach, A. Benoit, J. Meier, J. Ansermet, and B. Barbara (1996) Nucleation of the magnetization reversal in individual nanosized nickel wires. *Phys. Rev. Lett.* 77:1873

7. E. Bonet, W. Wernsdorfer, B. Barbara, A. Benoit, D. Mailly, and A. Thiaville (1999) Three-dimensional magnetization reversal measurements in nanoparticles. *Phys. Rev. Lett.* 83:4188

8. G. Schütz, W. Wagner, W. Wilhelm, P. Kienle, R. Zeller, R. Frahm, and G. Materlik (1987) Absorption of circularly polarized x rays in iron. *Phys. Rev. Lett.* 58:737-740

9. C. T. Chen, F. Sette, Y. Ma, and S. Modesti (1990) Soft-x-ray magnetic circular dichroism at the $L_{2,3}$ edges of nickel. *Phys. Rev. B* 42:7262

10. W. Wulfhekel and J. Kirschner (1999) Spin-polarized scanning tunneling microscopy on ferromagnets. *Appl. Phys. Lett.* 75:1944

11. W. Wernsdorfer, K. Hasselbach, A. Benoit, W. Wernsdorfer, B. Barbara, D. Mailly, J. Tuaillon, J. P. Perez, V. Dupuls, J. P. Dupin, G. Guiraud, and A. Perex (1995) High sensitivity magnetization measurements of nanoscale cobalt clusters. *J. Appl. Phys.* 78:7192

12. T. G. Pokhil and B. M. Moskowitz (1997) Magnetic domains and domain walls in pseudo-single-domain magnetite studied with magnetic force microscopy. *J. Geophys. Research* 102:22681-22694

13. S. Lee, H. Lee, K. Song, S.-Y. Choi, and H. S. Park (2017) *In-situ* observation of domain wall motion in electroplated Ni80-Fe20 thin film by Lorentz TEM and DPC imaging. *J. Magn.* 22: 563-569

14. T. Kasahara, H. S. Park, D. Shindo, H. Toshikawa, T. Sato, and K. Kondo (2006) In situ observations of domain wall motion in Mn-Zn and Ni-Zn ferrites by Lorentz microscopy and electron holography. *J. Magn. Magn. Mater.* 305:165-170

15. Y. O. Murakami, T. Seki, A. Kinoshita, T. Shoji, Y. Ikuhara, and N. Shibata (2020) Magnetic-structure imaging in polycrystalline materials by specimen-tilt series averaged DPC STEM. Microscopy 69:312-320

16. J. N. Chapman (1984) The investigation of magnetic domain structures in thin foils by electron microscopy. *J. Phys. D: Appl. Phys.* 17:623-647

17. J. M. D. Coey (2012) Permanent magnets: Plugging the gap. *Scr. Mater.* 67: 524-529

18. K. Hono and H. Sepehri-Amin (2012) Strategy for high-coercivity Nd-Fe-B magnets. *Scr. Mater.* 67: 530-535.

19. A. Hubert and R. Schäfer (1998) *Magnetic domains: the analysis of magnetic microstructures.* (Springer-Verlag, Berlin.)

20. J. D. Jackson (1998) *Classical electrodynamics (3rd ed.).* (Wiley, New York)

4. Evaluation of the method using an artificial specimen

4.1 Introduction

Regarding the examination of magnetic materials, electron holography allows for detecting the phase shift due to magnetic flux density (B) [1,2]. In other words, it has been difficult to discuss the demagnetization field (H_d), which is only one component of B, by using the electron holography observation, although revealing the H_d distribution within a crystal is of vital importance in the study of permanent magnet. Indeed, any tools which are widely used in materials science/engineering do not allow for direct observations of H_d. These tools include X-ray magnetic dichroism [3,4], spin-polarized scanning tunneling microscopy [5], micro-SQUID magnetometry [6], Lorentz microscopy and differential phase contrast microscopy [7].

To solve this essential problem in magnetic imaging, the author proposed the method that extracts the phase shift due to H_d ($\Delta\phi_{H_d}$) using the electron holography observation (*i.e.*, phase shift due to magnetic flux density $\Delta\phi_B$), as described in Chapter 3. The phase shift $\Delta\phi_B$ are assumed to be a summation of three components of phase shift: that is, (1) phase shift due to magnetization ($\Delta\phi_M$), (2) phase shift due to stray magnetic field outside the specimen ($\Delta\phi_{H_s}$), and (3) $\Delta\phi_{H_d}$(contribution of H_d that exists inside the specimen. To obtain phase information about H_d, other phase shift (*i.e.*, $\Delta\phi_B$, $\Delta\phi_M$, and $\Delta\phi_{H_s}$) could be determined by experiments (for $\Delta\phi_B$) and calculations using surface integral with respect to in-plane component of magnetic field (for $\Delta\phi_B$, $\Delta\phi_M$, and $\Delta\phi_{H_s}$) As mentioned in Chapter 3,

particular solutions to avoid the technical problem of the method, which is initial phase shift of surface integral becoming 0 and phase gap occurred near the specimen edges due to the undetermined plots of phase shift at the interfaces, were suggested. The phase images relevant to $\Delta\phi_B$, $\Delta\phi_M$, $\Delta\phi_{H_s}$ and $\Delta\phi_{H_d}$ subjected to these solutions are presented in this chapter, leading to a reasonable phase map of $\Delta\phi_{H_d}$.

Therefore, in this chapter, we shall evaluate the usefulness of the method to extract the phase information about H_d which was proposed in Chapter 3. In particular, we shall discuss (1) the role of the offset in the phase shift, which should be referred to in the surface integral (*i.e.*, calculations of $\Delta\phi_B$, $\Delta\phi_M$, and $\Delta\phi_{H_s}$), and (2) operations to avoid the phase gap (*i.e.*, the fluctuation of phase shift) near the specimen, which was applied all phase maps determined using the surface integral (except for $\Delta\phi_B$ representing electron holography observation), and (3) the phase map of $\Delta\phi_{H_d}$ derived from the correct offset for the phase shift $\Delta\phi_B$, $\Delta\phi_M$, and $\Delta\phi_{H_s}$. For this purpose, the author applied the method proposed in Chapter 3 to an artificial $Nd_2Fe_{14}B$ magnet (identical to the model specimen referred to in Chapter 3). Note that, in this chapter, the proposed method will be assessed by using the artificial $Nd_2Fe_{14}B$ specimen having a simple rectangular shape as shown in Fig. 4.1. as this is the first step in the evaluation of the method. Application to a more complex shaped specimen (*i.e.*, actual TEM specimen) will be discussed in the subsequent chapter.

4.2 Simulations of three-dimensional magnetic field for the artificial $Nd_2Fe_{14}B$ specimen

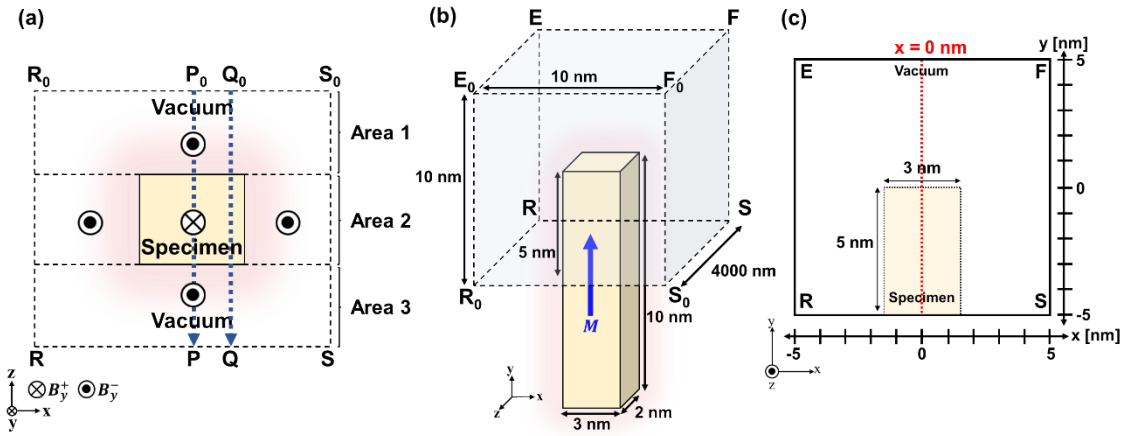

Fig. 4.1. Schematic representations describing the principle and conditions of phase shift calculations using an artificial $Nd_2Fe_{14}B$ bar magnet. (a) Cross section of specimen magnetized in the *y* direction. Incident electrons traverse in $-z$ direction. (b) Parallelepiped specimen with a size of 3×2×10 nm^3, and the cuboidal region (E, F, F_0, E_0, R, S, S_0, and R_0) irradiated by the object electron wave. (c) Area in which the phase images are revealed in Fig 4.3.

The artificial $Nd_2Fe_{14}B$ specimen in the form of a long bar, which is presented in Fig. 4.1, was adopted to evaluate the method. As shown in Fig. 4.1(b), the specimen is magnetized in the y direction with 1.6 T of the saturation magnetization ($\mu_0 M$), where μ_0 represents the permeability of vacuum. This model specimen had a large aspect ratio of 3.3 (*i.e.*, the length of the specimen in the y direction divided by the length in the x direction). This feature of the specimen will directly affect the distribution of H_d within the specimen, and the result will be presented later. To calculate the phase shift due to B, M and H_s, three-dimensional distribution of the magnetic field was calculated using the commercial code ELF/MAGIC (ELF Corp.). The simulated area indicates the cuboid (*i.e.*, the area indicated by the letters E, F, F_0, E_0, R, S, S_0, and R_0) in Fig. 4.1(b), which is assumed to be irradiated

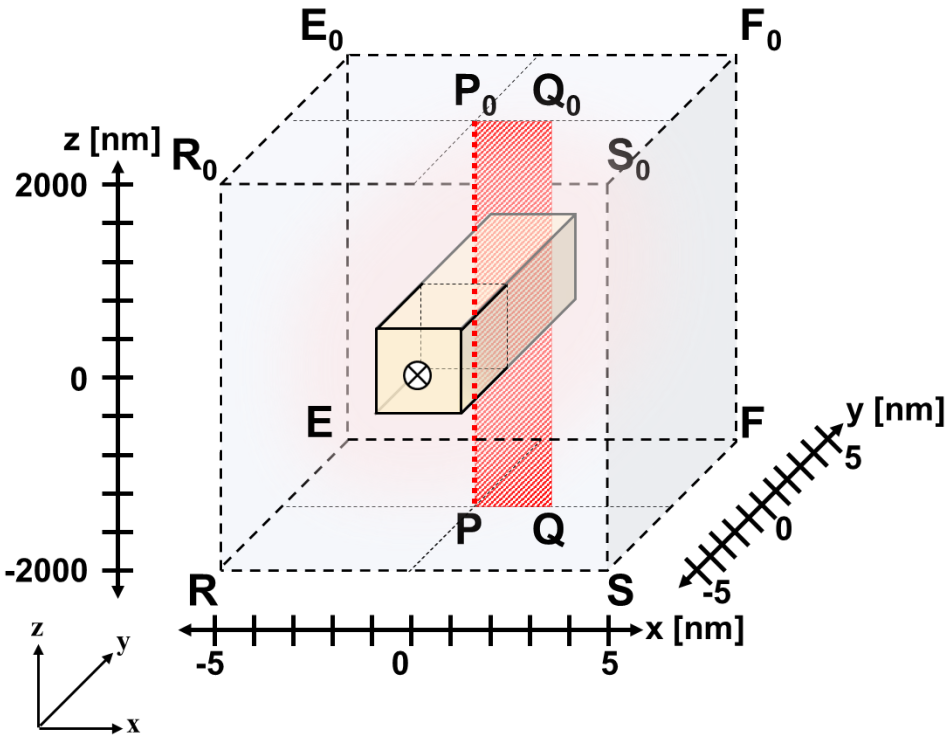

Fig. 4.2. Schematic representation describing the process of surface integral using an artificial $Nd_2Fe_{14}B$ specimen magnetized in the *y* direction. The surface integral was performed for P_0Q_0QP area. P_0 and P represent the start position of surface integral, fixed as (0, y_0, 2000) and (0, y_0, -2000) in the *x*-*y*-*z* coordinates system, respectively.

by the object electron wave. The incident electrons towards $-z$ direction. The phase maps in this chapter will be presented for the area of EFSR in Fig. 4.1(c), which are corresponding to that in Fig. 4.1(b). Refer to Chapter 3 for the details about the simulations.

4.3 Results and discussion

4.3.1 Procedure for the surface integral to obtain the phase maps

The phase maps could be obtained using the surface integral, as explained in Chapter 3.4.2, but it led to the asymmetric phase map of $\Delta\phi_{H_d}$ shown in Fig. 4.8(b). This result indicated that we need essential modifications to the

procedure for the surface integral, in order to obtain a reasonable, symmetric phase map that was calculated for a symmetric specimen as shown in Fig. 4.3(e). For this purpose, the coordinates of the reference points of P_0 and P (*i.e.*, the start points of the surface integral) from P_0 (0.05, y_0, 2000) and P (0.05, y_0, -2000) were changed to P_0 (0, y_0, 2000) and P (0, y_0, -2000), as illustrated in Fig. 4.2. This modification enables that the trace of reference points P_0 and P indicated by the red dotted line in Fig. 4.1(b) is placed on the equiphase line where the real values of phase shift that was assumed to be $\Delta\phi_{A_z}$ in the artificial specimen have zero, as indicated by the red dotted line in Fig. 4.4, because the surface integral yields the initial value of phase shift (*i.e.*, the phase shift located at the reference points of P_0 and P) having 0, as discussed in Chapter 3. The effects of this change in the positions of P_0 and P on the phase maps will be discussed for details in the next subsection. Details about the process of the surface integral are described in what follows.

The surface integral using Eq. (4.1) representing $\Delta\phi_B$ was performed for the hatched area closed by the four points P_0 (0, y_0, 2000), Q_0 (x_0, y_0, 2000), Q (x_0, y_0, -2000), and P (0, y_0, -2000), as shown in Fig. 4.2 [where the cuboidal area indicated by E_0, F_0, S_0, R_0, E, F, S, and R is corresponding to that in Fig. 3.1(b)].

$$\Delta\phi_B = -\frac{e}{\hbar}\iint_{P_0Q_0QP} B_y(x,y,z)dxdz, \qquad (4.1)$$

where B_y is the y component of magnetic flux density. For one value of y_0, the positions of P_0 and P are invariable which are fixed at the coordinates of

(0, y_0, 2000) and (0, y_0, -2000), respectively. Meanwhile, two positions of Q_0 (x_0, y_0, 2000) and Q (x_0, y_0, -2000) are variable in the x_0 range of [-5, 5]. By repeating the surface integral over this x_0 range, the phase shift in the line connecting two terminal points of Q (-5, y_0, -2000) and Q (5, y_0, -2000) could be determined. Adopting the same process in the surface integral for a different value of y_0 allows for the plots of phase shift in another line connecting Q (-5, y_0, -2000) and Q (5, y_0, -2000) with a different value of y_0. Following the steps, we could obtain the phase map representing $\Delta\phi_B$, which consists of all plots of the phase shift determined for the y_0 series, as shown in Fig. 4.3(a). This procedure of the phase-shift calculation was also applied to the determination of $\Delta\phi_M$ and $\Delta\phi_{H_s}$. The phase maps representing $\Delta\phi_M$ and $\Delta\phi_{H_s}$ derived by this process are shown in the next subsection.

4.3.2 Mapping of demagnetization field

Figure 4.3(a) shows the phase map that represents $\Delta\phi_B$ of the artificial bar magnet [*i.e.*, calculations by using Eq. (4.1)], where the magnitude and sense (increase or decrease) of the phase shift are indicated by colors with reference to a color bar shown in the mid of Fig. 4.3. The specimen is present in the area closed by the gray lines, which the outskirt area represents the vacuum region (*i.e.*, outside of the specimen). As described in Chapter 3.4, the small change in the phase was induced by the small volume of the specimen shown in Fig. 4.1(b). The contour gradient in Fig. 4.3(a) represents the phase contours, which can be a good approximation of the distribution of magnetic flux lines [2]. With reference to the phase map in Fig. 4.3(a), the

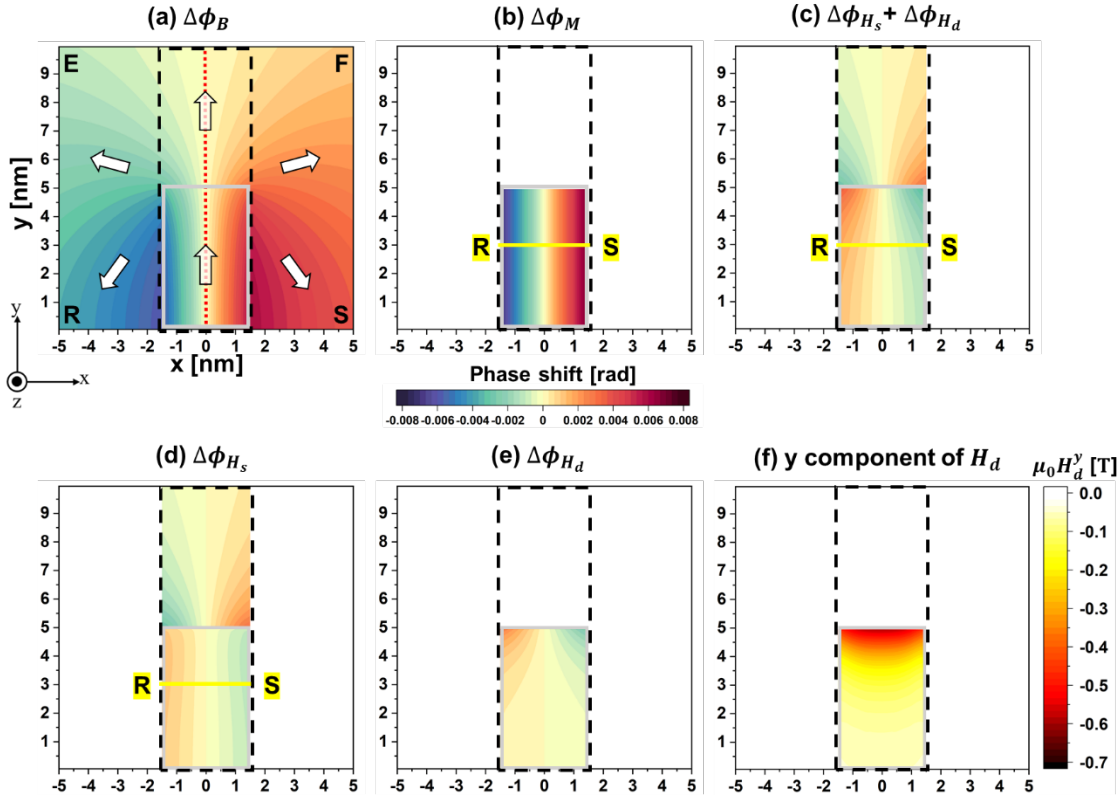

Fig. 4.3. Demagnetization field revealed using calculations of the phase images for an artificial $Nd_2Fe_{14}B$ specimen. (a) Phase image of $\Delta\phi_B$ representing the contribution from the magnetic flux density. (b) Phase image of $\Delta\phi_M$ representing the contribution from the magnetization. (c) Phase image of $\Delta\phi_{H_s}$+$\Delta\phi_{H_d}$ obtained by the subtraction of $\Delta\phi_M$ from $\Delta\phi_B$. (d) Phase image of $\Delta\phi_{H_s}$ representing the contribution from the stray magnetic field outside of the specimen. (e) Phase image of $\Delta\phi_{H_d}$ representing the contribution from the demagnetization field inside of the specimen. The result was obtained by the subtraction of $\Delta\phi_{H_s}$ from $\Delta\phi_{H_s}$+$\Delta\phi_{H_d}$. (f) Mapping of the *y* component of the demagnetization field revealed using the result in (e). The phase images in (b)-(f) are presented in the area indicated by the black dotted line in (a). Line profiles of phase shift measured along the R-S line in (b), (c) and (d) are shown in Fig. 4.5

directions of the magnetic flux lines are indicated by the white arrows. Note that, as Eq. (4.1) indicates, the phase image in Fig. 4.3(a) was obtained by using the surface integral with respect to B_y. The result of the surface integral showed a good agreement with the calculation when using the line integral for A_z shown in Fig. 4.4. The symmetric shape of the artificial specimen meant that the value of phase shift ($\Delta\phi_B$) in the red dotted line of Fig. 4.3(a)

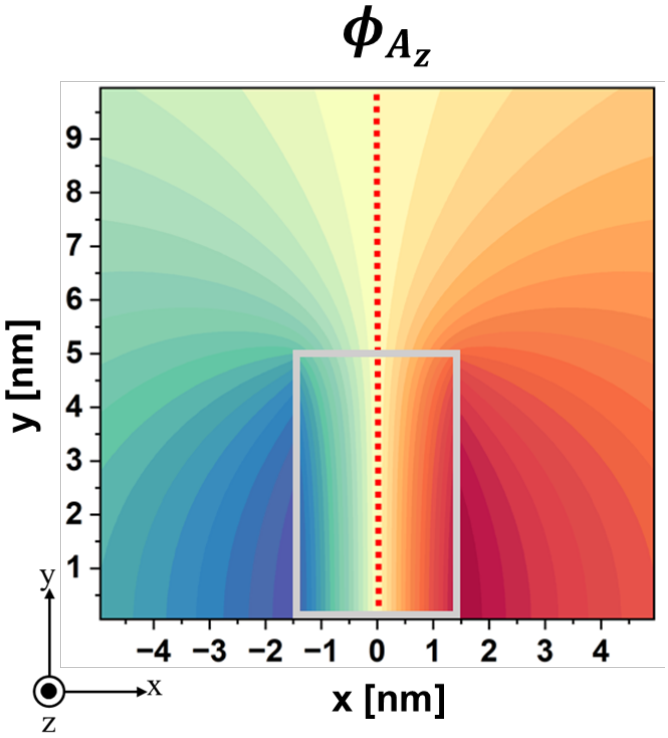

Fig. 4.4. Phase map calculated from the line integral for A_z using the artificial specimen.

could be zero for both the calculations using the *y* component of magnetic field B_y (surface integral) and the *z* component of vector potential A_z (line integral). The reference points in the surface integral (*i.e.*, P_0 and P) for this artificial specimen were placed on the red dotted line in Fig. 4.3(a). Great details about it will be discussed in subsection 4.3.3.

Figure 4.3(b) provides a phase image that represents $\Delta\phi_M$ calculated using Eq. (4.2) with the y component of magnetization M_y:

$$\Delta\phi_M = -\frac{e}{\hbar}\iint_{area2}\mu_0 M^y(x,y,z)dxdz, \qquad (4.2)$$

The specimen was magnetized along the *y* direction; therefore, the sense of the phase gradient is positive, *i.e.*, the value of the phase shift increases in the *x* direction. The phase gradient measured along the R-S line in Fig. 4.3(b) is indicated by the blue plots representing $\Delta\phi_M$ in Fig 4.5, showing the positive gradient of phase shift with respect to the *x* direction. Figure 4.3(c) shows the phase map that represents $\Delta\phi_{H_s} + \Delta\phi_{H_d}$, which was obtained by the subtraction of $\Delta\phi_M$ from $\Delta\phi_B$, in accordance with Eq. (4.3).

$$\Delta\phi_{H_s} + \Delta\phi_{H_d} = \Delta\phi_B - \Delta\phi_M. \qquad (4.3)$$

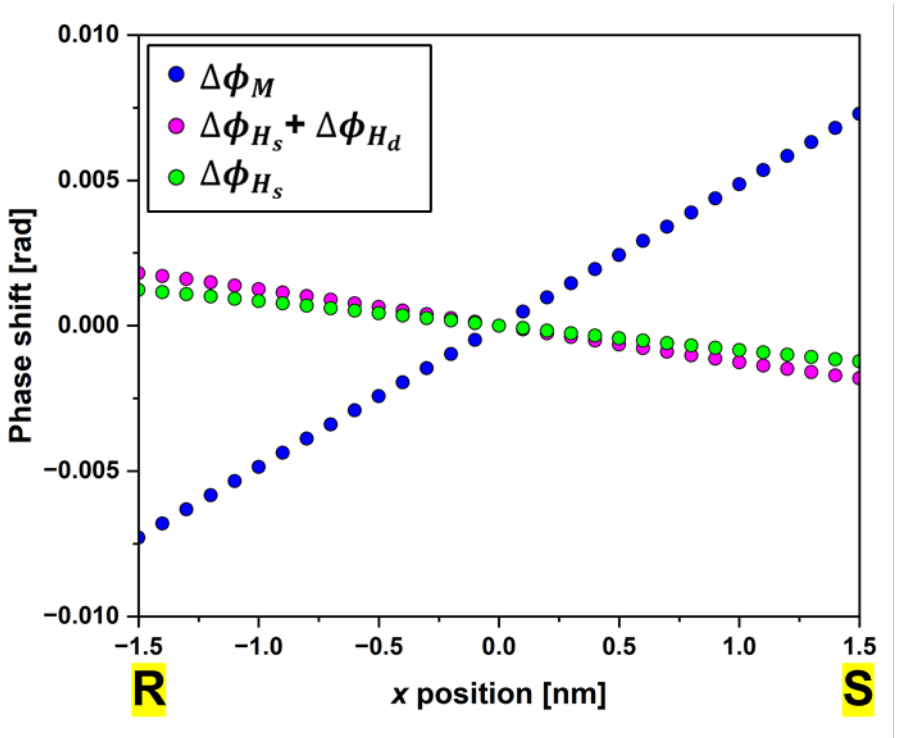

Fig. 4.5. Line profiles of phase shift measured along in the R-S line (in the *x* direction) in Fig. 4.3. Blue, pink and green plots representing the phase shift due to *M*, phase shift due to $H_s + H_d$, and phase shift due to H_s.

The result of the subtraction is presented for the area closed by the black dotted lines; this closed area is identical to those in Figs. 4.3(a), (b), and (d)-(f). The details related to this will be discussed in the next subsection. The result in the upper area of Fig. 4.3(c) (*i.e.*, the plot in the vacuum region) simply shows the phase shift due to the stray magnetic field ($\Delta\phi_{H_s}$) and is identical to the upper area in Fig. 4.3(a). More importantly, in the lower area of Fig. 4.3(c), the sense of the phase gradient has become negative, *i.e.*, the value of phase shift decreases in the *x* direction, and this result is indicated by the pink plots for $\Delta\phi_{H_s} + \Delta\phi_{H_d}$ in Fig. 4.5 that was measured along the R-S line in Fig. 4.3(c). This is in contradiction to the positive phase gradient observed in Figs. 4.3(a) and (b). Therefore, the result of Fig. 4.3(c) indicates the presence of a magnetic field, of which the direction is opposite to the magnetization *M*, in the specimen.

To reduce the contribution of $\Delta\phi_{H_s}$, which is superposed to Fig. 4.3(c), the stray magnetic field outside of the specimen was calculated in three dimensions with reference to the specimen shown in Fig. 4.1. Using Eq. (4.4), which refers to the *y* component of H_s (H_s^y), a phase map that represents $\Delta\phi_{H_s}$ was obtained, as shown in Fig. 4.3(d).

$$\Delta\phi_{H_s} = -\frac{e}{\hbar}\iint_{outside}\mu_0 H_s^y(x,y,z)dxdz, \qquad (4.4)$$

Because of the stray magnetic field that exists in both areas $z > 0$ and $z < 0$, *i.e.*, areas 1 and 3 in Fig. 4.1(a), the lower half region of Fig. 4.3(d) (showing the specimen position) is subject to a negative phase gradient in

the x direction, as referring to the green plots [estimated along the R-S line in Fig. 4.3(d)] for $\Delta\phi_{H_s}$ in Fig. 4.5. This result also indicates the presence of a stray magnetic field in the $-y$ direction of this region. Figure 4.3(e) shows the contribution of $\Delta\phi_{H_d}$, which was obtained by subtraction of the result in Fig. 4.3(d) from Fig. 4.3(c). There is a significant phase shift in the plot of $\Delta\phi_{H_d}$ near the specimen edge. In contrast, there is only a negligible change in phase in the region away from the specimen edge. The distribution of the $\Delta\phi_{H_d}$ plots in Fig. 4.3(e) appears the symmetry, and the related discussion will be covered in the next subsection. The phase shift of $\Delta\phi_{H_d}$ was converted to the y component of the demagnetization field ($\mu_0 H_d^y$, in the unit of magnetic flux density, tesla) using the relationship [1]:

$$\mu_0 H_d^y = -\frac{\partial \Delta\phi_{H_d}}{\partial x} \cdot \frac{\hbar}{e} \cdot \frac{1}{t}, \qquad (4.5)$$

where e, $\hbar$ and t is the elementary charge, Planck's constant divided by 2π and the specimen thickness, respectively. Figure 4.3(f) plots the value of $\mu_0 H_d^y$ for the area in which the specimen exists. As expected for the small parallelepiped specimen with the large aspect ratio, shown in Fig. 4.1(b), the demagnetization field is maximized in the vicinity of the specimen edge, although it is abruptly reduced with distance from the edge. The maximum value of $\mu_0 H_d^y$ was approximately -0.67 T (in the $-y$ direction). This magnitude in terms of $\mu_0 H_d^y$ is considered as reasonable value when referring to the micromagnetic calculation reported by Bance et. al. [8], where the magnitude of $\mu_0 H_d^y$ estimated for a cuboidal shape of model

$Nd_2Fe_{14}B$ specimen having a small $Nd_2Fe_{14}B$ grain (~10 nm) indicated a value less than approximately 0.7 T. For further discussion regarding the validity of the method, the mapping of H_d using the real $Nd_2Fe_{14}B$ thin foil is analyzed with the viewpoint of classical electromagnetism and calculations by micromagnetic simulations performed in this study.

4.3.3 Discussion

The phase map of $\Delta\phi_B$ of Fig. 4.6(a) [equal to Fig. 4.3(a)] that was obtained by using the surface integral for B_y shows the symmetric magnetic flux lines, which is consistent with the phase map using the line integral for A_z [Fig. 4.4].The result of Fig. 4.3(a) it is in contrast with the previous phase map of $\Delta\phi_B$ shown in Fig. 4.6(b) [equal to Fig. 3.3(a)] although two phase

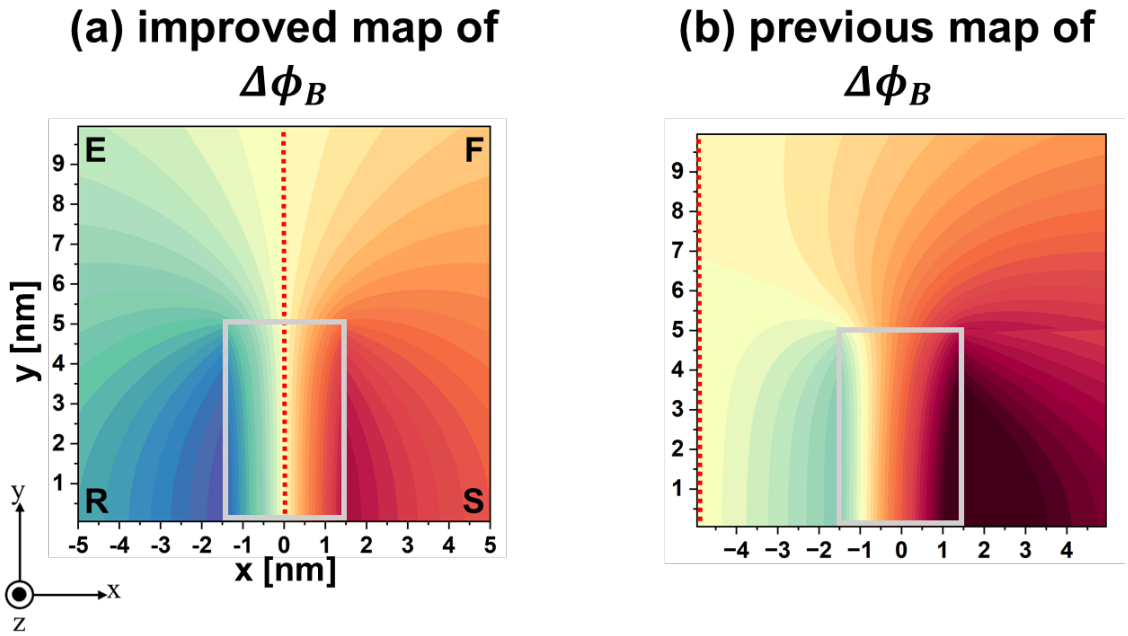

Fig. 4.6. Phase maps representing the contribution of *B*. (a) Phase map of $\Delta\phi_B$ identical to Fig. 4.3(a), where the reference points are P_0 (0, y_0, 2000) and P (0, y_0, -2000). (b) Previous phase map about $\Delta\phi_B$ due to incorrect offset of phase shift, equal to Fig. 3.3(a), where the reference points are P_0 (0.05, y_0, 2000) and P (0.05, y_0, -2000).

maps were determined identically by the surface integral using B_y. As mentioned in the above subsection, the modification of reference positions [*i.e.*, transfer to P P_0 (0, y_0, 2000) and P (0, y_0, -2000)] could force the initial $\Delta\phi_B$ using the surface integral to be placed on the plausible locations of x=0, that is, placed along the equiphase line indicated by the red dotted line in the phase map of ϕ_{A_z} in Fig. 4.4 representing true phase shift inferred from the artificial specimen. However, regarding the real specimen, such as non-symmetric shaped specimen and not completely uniaxial of the c-axis of the crystal grain, it is difficult to find the positions of the reference points to be placed perfectly on the equiphase line in the phase image. For this point, the offset of phase shift (*i.e.*, the initial value of phase shift) should be determined by referring to the experimental result, that is, the electron

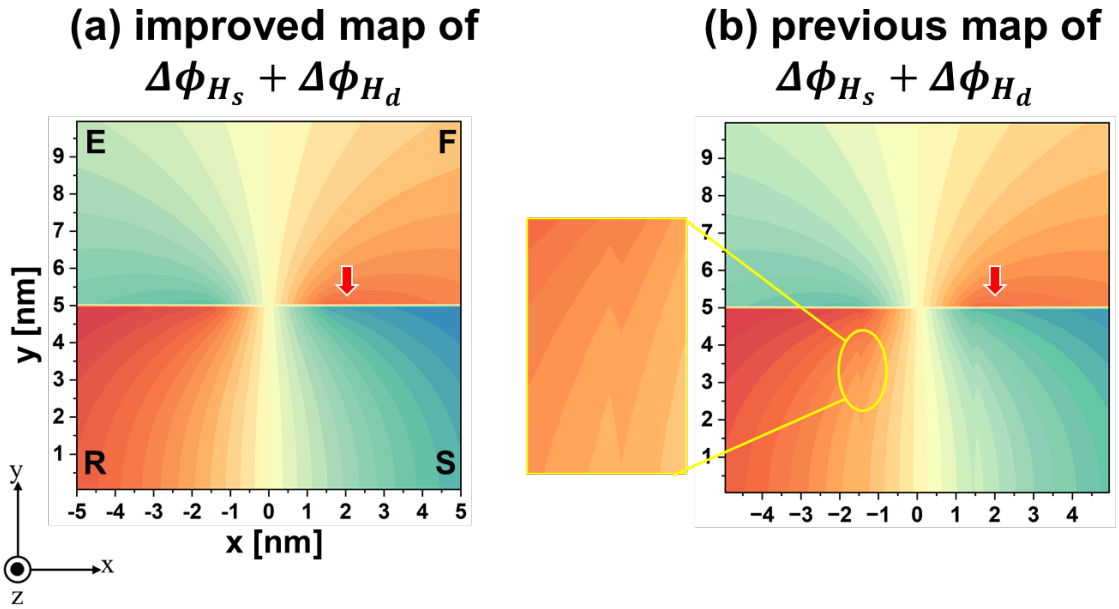

Fig. 4.7. Phase maps representing the contribution of H_s and H_d. (a) Phase map of $\Delta\phi_{H_s} + \Delta\phi_{H_d}$, for which the entire plots (indicated by letters E, F, S, and R) for $\Delta\phi_{H_s} + \Delta\phi_{H_d}$ presented from Fig. 4.3(c). (b) Phase map about $\Delta\phi_{H_s} + \Delta\phi_{H_d}$ equal to the Fig. 3.5(b). Red arrow and yellow lines indicate the phase gap and fluctuation near the interfaces/surface of specimen.

holography observation. Results related to this will be discussed in Chapter 5. As a result, for the artificial specimen, the reasonable offset for the phase shift $\Delta\phi_B$ could be determined on the basis of the calculations using the vector potential (*i.e.*, ϕ_{A_z}), and this operation was also applied to the offset for other phase shift $\Delta\phi_M$ and $\Delta\phi_{H_s}$ shown in Figs. 4.3(b) and (d).

The map of $\Delta\phi_{H_s} + \Delta\phi_{H_d}$ [Fig. 4.3. (c)], as a result of the subtraction of $\Delta\phi_M$ from $\Delta\phi_B$, shows a gap in the phase at the interface between the specimen and the vacuum region, as indicated by the red arrow in Fig. 4.7: that is, as described in Chapter 3.4, this simple method using the subtraction is unable to provide essential phase information in the surface/interface region. Nevertheless, the discussion on the phase gradient is valid for a wide area in the specimen, except for the limited portions in the surface and/or interface. Meanwhile, the map of $\Delta\phi_{H_s} + \Delta\phi_{H_d}$ in this chapter has improved than the previous map of Fig. 4.7(b) [equal to Fig. 3.5(b)], and the improved map of Fig. 4.7(a) showing all plots of $\Delta\phi_{H_s} + \Delta\phi_{H_d}$ for the entire region [corresponding to the EFSR area shown in Fig. 4.3(a)] to Fig. 4.3(c). The previous result of Fig. 4.7(b) shows that the fluctuation of phase shift is observed near the specimen edges in the *y* direction, as indicated by the yellow line and referring to the enlargement. Otherwise, Fig. 4.7(a) provides the phase map with no phase fluctuation near the specimen edges in the *y* direction. The fluctuation of phase shift near the specimen edges in the *y* direction, as described in Chapter 3.4, appeared to be caused by the unconsidered magnetic fields located at (and/or very close to) the specimen edge, when performing the surface integral. For this source, in this study, the three-dimensional magnetic field with the coordinates of $[x_1,\ y_0,\ z_0]$, where

the ranges of x_1, y_0 and z_0 are $x_1 = \pm 1.5$, $-5 \leq y_0 \leq 5$, and $-2000 \leq z_0 \leq 2000$, was calculated for the phase shift $\Delta\phi_B$, $\Delta\phi_M$, and $\Delta\phi_{H_s}$. Because of the existing the plots of phase shift placed on the specimen edges (in the *y* direction), the fluctuation of phase shift could be reduced in the phase map of $\Delta\phi_{H_s} + \Delta\phi_{H_d}$, as shown in Fig. 4.7(a). For the real specimen, however, determining the true plots of phase shift located on the surfaces/interfaces of the specimen using the surface integral is somewhat difficult. Therefore, to effectively reveal the phase maps, the author used the operation that trims the unreliable areas derived from the vicinity of the specimen edges [*i.e.*, elimination of the remaining except for the area closed by the black dotted line in Fig. 4.3(a)], as shown in the lower half regions of Figs. 4.3 (b)-(e). This operation was also applied to the phase maps using the real specimen, as discussed in Chapter 5.

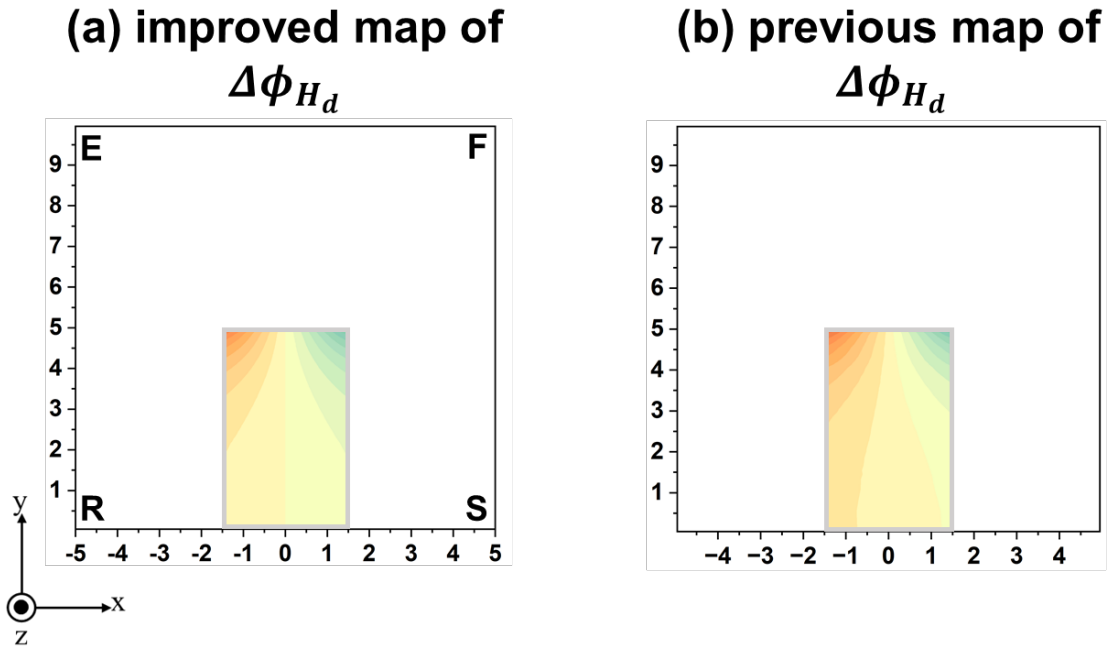

Fig. 4.8. Phase maps representing the contribution of H_d. (a) Phase map of $\Delta\phi_{H_d}$ identical to Fig. 4.3(e) having the symmetric phase contours. (b) Previous phase map about of $\Delta\phi_{H_d}$ that is identical to Fig. 3.5(d).

Figure 4.8(a) shows the improved phase map representing $\Delta\phi_{H_d}$ that is identical to Fig. 4.3(e). The previous map of Fig. 4.8(b) approximating $\Delta\phi_{H_d}$, equal to Fig. 3.5(d), shows the asymmetric phase distribution. On the contrary, Fig. 4.8(a) reveals the symmetric distribution of the $\Delta\phi_{H_d}$ plots. This result was originated from the correctly determined offset in the phase shift $\Delta\phi_B$, $\Delta\phi_M$ and $\Delta\phi_{H_s}$ because the phase map of $\Delta\phi_{H_d}$ was determined by the subtraction of phase maps for $\Delta\phi_M$ and $\Delta\phi_{H_s}$ from the phase map of $\Delta\phi_B$.

4.4 Summary

In this chapter, the validity of the proposed method was demonstrated using the artificial $Nd_2Fe_{14}B$ specimen with the improved phase images. For the phase map of $\Delta\phi_{H_s} + \Delta\phi_{H_d}$, we found that the fluctuation in the phase shift near the specimen edges disappeared although the phase gap placed on the interfaces in the *x* direction was left. Unfortunately, this kind of improvement (*i.e.*, removal of the phase fluctuation around the specimen edge) cannot be applied to the real specimen. Therefore, the phase map of $\Delta\phi_{H_s} + \Delta\phi_{H_d}$ (also other phase maps representing $\Delta\phi_M$, $\Delta\phi_{H_s}$ and $\Delta\phi_{H_d}$) only revealed the remained region inside the specimen by trimming the vicinity of the specimen edges. Furthermore, the phase map of $\Delta\phi_{H_d}$ showed a visible improvement with the symmetric distribution of the $\Delta\phi_{H_d}$ plots by correctly determining the offset for the phase shift $\Delta\phi_B$, $\Delta\phi_M$ and $\Delta\phi_{H_s}$ with reference to the calculation using the vector potential. The characteristic feature of the H_d distribution derived from this phase map of $\Delta\phi_{H_d}$ showed

the maximized magnitude of $\mu_0 H_d$ in the adjacent to the specimen edge, which was consistent with the expectation about H_d for the small parallelepiped specimen having the large aspect ratio.

Chapter 4 References

1. E. Völkl, L. F. Allard, and D. C. Joy (1999) *Introduction to Electron Holography.* (Kluwer Academic/Plenum Publishers, New York.)

2. A. Tonomura (1999) *Electron Holography (2nd ed.).* (Springer, Heidelberg)

3. G. Schütz, W. Wagner, W. Wilhelm, P. Kienle, R. Zeller, R. Frahm, and G. Materlik (1987) Absorption of circularly polarized x rays in iron. *Phys. Rev. Lett.* 58:737-740

4. C. T. Chen, F. Sette, Y. Ma, and S. Modesti (1990) Soft-x-ray magnetic circular dichroism at the $L_{2,3}$ edges of nickel. *Phys. Rev. B* 42:7262

5. W. Wulfhekel and J. Kirschner (1999) Spin-polarized scanning tunneling microscopy on ferromagnets. *Appl. Phys. Lett.* 75:1944

6. W. Wernsdorfer, K. Hasselbach, A. Benoit, W. Wernsdorfer, B. Barbara, D. Mailly, J. Tuaillon, J. P. Perez, V. Dupuls, J. P. Dupin, G. Guiraud, and A. Perex (1995) High sensitivity magnetization measurements of nanoscale cobalt clusters. *J. Appl. Phys.* 78:7192

7. J. N. Chapman (1984) The investigation of magnetic domain structures in thin foils by electron microscopy. *J. Phys. D: Appl. Phys.* 17:623-647

8. S. Bance, B. Seebacher, T. Schrefl, L. Exl, M. Winklhofer, G. Hrkac, ... &

A. Manabe, (2014). Grain-size dependent demagnetizing factors in permanent magnets. *Journal of Applied Physics 116*(23): 233903.

5. Evaluation of the method using a real specimen

5.1 Introduction

In the field of electron microscopy, the observation of the demagnetization field (H_d) has been considered as a challenge. This issue has been also applied to electron holography that detects the phase shift induced by only magnetic flux density B ($\Delta\phi_B$) for the magnetic materials because $\Delta\phi_B$ is perceived as the summation of the phase shift due to magnetization M ($\Delta\phi_M$), the phase shift due to stray magnetic field H_s ($\Delta\phi_{H_s}$), and the phase shift due to H_d ($\Delta\phi_{H_d}$) [1,2]. Moreover, the discussion about H_d is important for the permanent magnets, *i.e.*, the Nd-Fe-B system that is a typical sintered permanent magnet. The various industries including hybrid/electric vehicles, robots, and drones have required further improvement of the coercivity (H_c, the measured value of critical magnetic field to induce undesired magnetization reversal), as this demand allows traction motors to be significantly downsized. Note that the demagnetization field contributes to the coercivity mechanism: the region where H_d within the magnet are most distributed can trigger nucleation of the reverse magnetic domains, leading to a drop in the coercivity [3,4]. This effect of H_d on the coercivity mechanism has been revealed using micromagnetic simulations, and model specimens of simple shapes has been mainly dealt with [4-10] (refer to Chapter 1.2 for details about the study on H_d using micromagnetic simulation). However, studies on H_d using real magnetic specimens have not been intensively revealed due to the technical limit to the experimental tools.

In order to overcome the problems derived from H_d in both electron microscopy field and the magnetic material engineering, the method was proposed to extract the phase information of H_d and its validity was evaluated using the artificial $Nd_2Fe_{14}B$ bar, as presented in Chapter 3 and 4. In this chapter, the method was applied to an actual thin-foil specimen comprised of a single crystal of the $Nd_2Fe_{14}B$ phase using the electron holography observation. For this evaluation, the author attempted to obtain a rectangular specimen having a constant thickness by using a focused ion-beam system. However, the specimen that was analyzed showed an asymmetric shape with thickness variation. Although the irregularity in the specimen shape (*i.e.,* deviation from an ideal rectangular specimen having a constant thickness) degrades the precision in extracting the phase information related to H_d, we used this thin-foiled specimen to discuss the effectiveness of the method. In addition, this chapter showed results of various electron microscopy observations and simulations involved in producing the phase maps that represent $\Delta\phi_M$ and $\Delta\phi_{H_s}$. As it will be mentioned later, the phase information representing H_d (derived from the electron holography observation) will be compared with the result of micromagnetic simulation.

5.2 Experimental methods

5.2.1 Specimen preparation

As discussed in section 5.3 in greater detail, we attempted to map H_d in a thin-foil Nd-Fe-B specimen. A system of focused ion beam / scanning electron microscope (FIB/SEM; Helios G4 UX, FEI Co.) in National Institute for Materials (NIMS) was used to obtain an approximately rectangle-shaped $Nd_2Fe_{14}B$ crystal (in a single-crystalline state) from a

commercial Nd-Fe-B sintered magnet with micrometer sized crystal grains. The rectangular crystal was then polished into a thin foil using another FIB instrument (MI4000L, Hitachi Ltd.) in the Ultramicroscopy Research Center (URC) of Kyushu University. To reduce surface damage, the foil was polished using a Ga ion beam with a low acceleration voltage (5 kV) at the final stage of specimen preparation.

5.2.2 Electron microscopy observations

The orientation of the *c*-axis of the thin-foil single-crystalline specimen was determined using electron diffraction with a 300 kV transmission electron microscope (HF-3300X, Hitachi Ltd.) and lattice image observation with a 200 kV transmission electron microscope (JEM-ARM200F, JEOL Ltd.) in the URC of Kyushu University. The specimen thickness (*t*) was determined using a log-ratio method (described in Chapter 2.1.2) of electron energy-loss spectroscopy [11] with a spectrometer GIF Quantum ER system (Gatan Inc.) attached to the JEM-ARM200F microscope in the URC of Kyushu University. EELS provided spectrum images, for which a region indicated by green lines in Fig. 5.1(a) was investigated. The intensity of the zero-loss peak was measured by 0.5 eV per channel where the convergence angle and an aperture size of condenser lens are 3 rad and 40 μm, respectively. Accordingly, Fig. 5.1(b) shows a log-ratio relative thickness map (*i.e.*, the map representing $\frac{t}{\lambda}$, where λ stands for the mean free path of inelastic scattering in the $Nd_2Fe_{14}B$ phase). To obtain only the thickness component from Fig. 5.1(b), λ for the $Nd_2Fe_{14}B$ phase was determined by the complex analysis using cross sectional observations and the simulations, and details

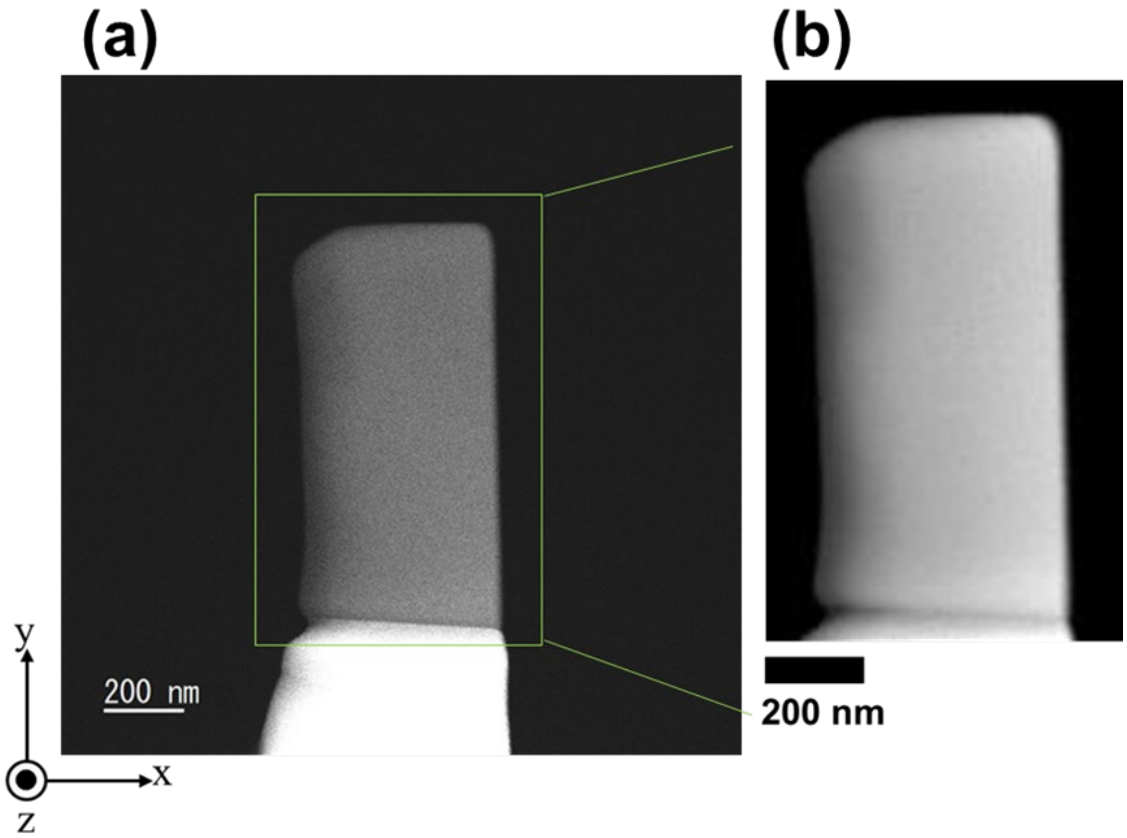

Fig. 5.1 (a) Scanning transmission electron microscopy (STEM) image of a thin-foiled $Nd_2Fe_{14}B$ specimen. Green lines indicate the investigated area for a spectrum image. (b) Log-ratio relative thickness map ($= \frac{t}{\lambda}$) by EELS, corresponding to the area indicated by the green lines in (a).

of the process for the determination of λ is explained in the next section. After all, by using λ determined in this study, the thickness map of the specimen could be obtained, and results related to this is presented in the next section as well.

5.2.3. Electron holography

Electron holograms were acquired using the HF-3300X microscope (in the URC of Kyushu University) equipped with the double biprism system [12], where the specimen was placed in a position free from the magnetic

field generated by the objective lens (*i.e.*, Low-Mag mode mentioned in Chapter 2.1.1). The holograms were recorded using a high-sensitivity camera (K3 IS camera, Gatan Inc.). When the electron hologram was acquired, the electron biprism was put in the left side of the specimen, away from the right edge of the specimen by 1908 nm, which was measured from the origin (x=0 nm) defined in Fig. 5.9(d). The width of interference between the object and reference waves was 2663 nm. The parameters for hologram acquisition were incorporated when a reconstructed phase image was simulated using the model specimen shown in Fig. 5.9(b). The model specimen was utilized to work out the three-dimensional distribution of magnetic fields (using the ELF/MAGIC code, EFL Corp.) for the prediction of $\Delta\phi_M$ and $\Delta\phi_{H_s}$, and the discussion addressing this is described in Chapter 5.3.

5.3 Results and discussion

5.3.1 Crystal orientation (the direction of the *c*-axis)

To determine the coordinates of c-axis of the thin-foil $Nd_2Fe_{14}B$ specimen shown in Fig. 5.2(a), the author used a rotation matrix [13]. In the x-y-z coordinates system given in Fig.5.9, a rotation of α radians about the x-axis, a rotation of β radians about the y-axis are defined as

$$R_x(\alpha) = \begin{bmatrix} 1 & 0 & 0 \\ 0 & \cos\alpha & -\sin\alpha \\ 0 & \sin\alpha & \cos\alpha \end{bmatrix}, \quad (5.1)$$

$$R_y(\beta) = \begin{bmatrix} \cos\beta & 0 & \sin\beta \\ 0 & 1 & 0 \\ -\sin\beta & 0 & \cos\beta \end{bmatrix}, \quad (5.2)$$

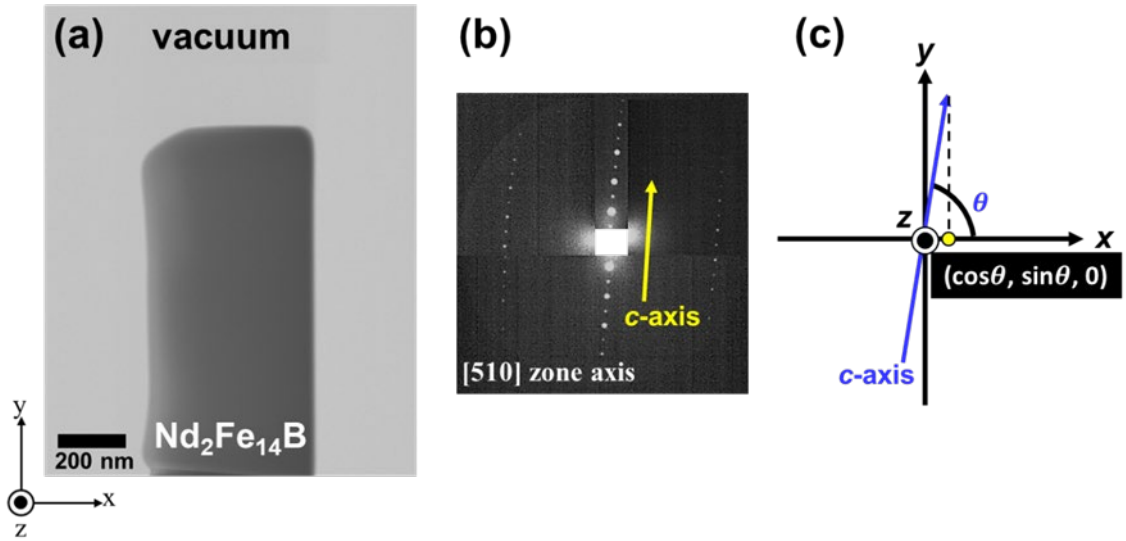

Fig. 5.2 Calculation of the direction of *c*-axis using electron diffraction pattern. (a) TEM image of the thin-foiled $Nd_2Fe_{14}B$ specimen. (b) electron diffraction pattern of the specimen with the [510] zone axis. Yellow arrow approximately indicates the direction of *c*-axis of the specimen. (c) Schematic illustration representing the coordinate of *c*-axis, that is $(\cos\theta, \sin\theta, 0)$, given from (b) in the *x*-*y* coordinate system.

where α and β are the Euler angles [the other degree of freedom of rotation (γ) about the z-axis was disregarded, as a double-tilt transmission electron microscopy (TEM) holder that functionalizes the rotation for the α and β angles was utilized for TEM observations]. The electron incidence is in the $-z$ direction. The rotation matrix can be expressed by two rotations [*i.e.*, $R_x(\alpha)$ and $R_x(\beta)$]. In principle, the elements of rotation matrix depend on the order of those rotations $R_x(\alpha)$ and $R_x(\beta)$ that are multiplied. Among the several orders of the matrix about each axis, in this study, the general form of rotation matrix was considered as the rotation first about the x-axis, then the y-axis, which is represented as the matrix product by

$$R = R_x(\beta)R_x(\alpha). \quad (5.3)$$

The direction of *c*-axis was analyzed by exploiting two results of TEM observations: (1) the electron diffraction pattern (DP) and (2) the lattice image. Figure 5.2(b) is a DP of the thin-foil specimen made up the single $Nd_2Fe_{14}B$ grain at the zone axis of [510] where the Euler angles about the *x*- and *y*-axis were α_1 and β_1, respectively. The coordinates of the *c*-axis (*i.e.*, the magnetization vector) was calculated by referring to the direction of the *c*-axis indicated by the yellow arrow in Fig. 5.2(b) and the angle (θ) that is from the *x*-axis in Fig. 5.2(c), which could be considered as the coordinates of $(\cos\theta, \sin\theta, 0)$ in the coordinates of *x*-*y*-*z* system. Then, when the electron holograms were acquired with the specimen rotated by of α_0 and β_0, the rotation matrix using Eq. (5.3) should be applied to the magnetization vector [*i.e.*, the coordinates of $(\cos\theta, \sin\theta, 0)$] deduced from the DP], where α and β in Eq. (5.3) were inserted as $\alpha_0 - \alpha_1$ and $\beta_0 - \beta_1$, respectively. Note that the electron diffraction pattern provides the

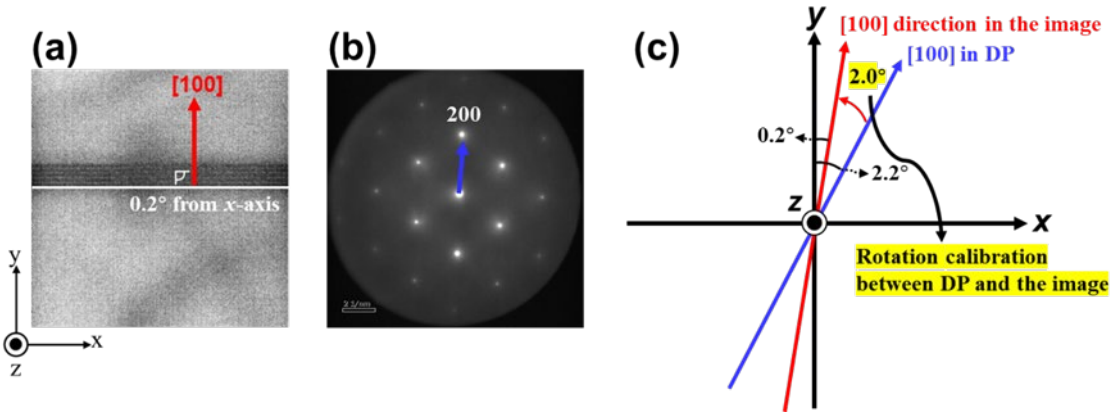

Fig. 5.3 Calibration of rotation angle between (a) TEM image and (b) DP using the calibration reference standard manufactured from a single crystal silicon wafer. (c) Schematic illustration representing the process of determining the rotation angle to calibrate between (a) and (b) in the *x*-*y* coordinate system

approximation about the coordinates of the *c*-axis because this result should be calibrated by the rotation calibration between the DP and the projected image recorded by the cameras [*e.g.*, the slow-scan charge-coupled-device (CCD) camera and the direct detection camera] in TEM. Regarding this rotation calibration, the calibration reference standard for TEM (MAG*I*CAL® NANORULER, Norrox Scientific Ltd.) was used, which was manufactured from a single crystal silicon wafer, and the results are presented by Fig. 5.3. Figure 5.3(a) shows a TEM image of the standard specimen. The [100] direction is considered as 'up' in the image (*i.e.*, the [100] direction perpendicular to the specimen edge in the *x* direction) indicated by the red arrow in Fig. 5.3(a), that is almost 0.2 degrees from the *y*-axis shown in Fig. 5.3(c) that represents the coordinates system of the *x*-*y* plane. On the other hand, an angle to the (200) diffraction spot in a DP of the standard specimen [Fig. 5.3(b)] is approximately 2.2 degrees from the *y*-axis, as indicated by the blue arrow in Fig. 5.3(c). This result indicates that the rotation calibration from DP to the image is about 2.0 degrees in the anti-clockwise direction, as presented in Fig. 5.3(c). Then, by applying this rotation calibration (Fig. 5.3) to the orientation of the *c*-axis using DP of Fig. 5.2(b), the direction of magnetization vector was determined to be [0.05039, 0.9947, -0.08922] with reference to the *x*-*y*-*z* coordinate system shown in Fig. 5.9. This result shows the crystal orientation tilted from the *y*-axis that is nearly parallel to the long-axis of the specimen: namely, the direction of the c-axis on the surface grain of the specimen in the *x*-*y* plane is tilted by about 2.9 degrees from the *y*-axis. On the contrary to DP, a lattice image enables us to straightforwardly obtain the crystal orientation. Figure 5.4(a) shows the lattice mage of the $Nd_2Fe_{14}B$ thin-foil specimen with the [510] zone axis and

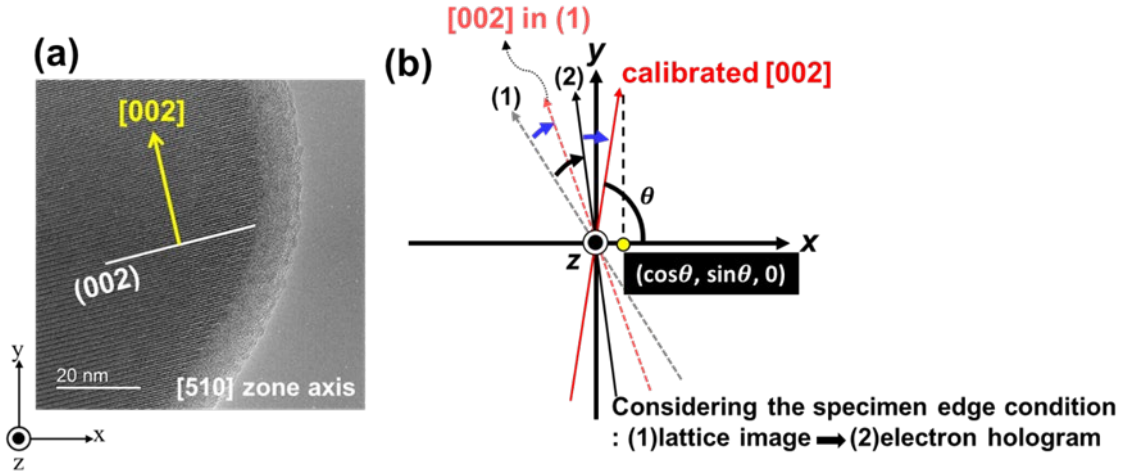

Fig. 5.4 Analysis on the direction of *c*-axis of the specimen using (a) a lattice image at the [510] zone axis. (b) Schematic illustration representing the process of determining the direction of *c*-axis with reference to the conditions of specimen edge between (1) lattice image and (2) electron hologram.

represents the direction of the *c*-axis indicated by the yellow arrow, which was observed under the condition of Euler angles having α_2 and β_2. Through the observation of lattice image, we could know the rotation angle between (1) the specimen edge in the *y* direction and the [002] direction deduced from the lattice image, which was presented in the blue arrow in Fig. 5.4 (b) (*i.e.*, in the coordinates system of the *x*-*y* plane).One to be noted is the position of specimen edges should be carefully considered, as the specimen position put in the specimen holder was slightly different when taking (2) the electron holograms and (1) the lattice images. Following a careful consideration in terms of specimen edges, as shown in Fig. 5.4(b), we could obtain the calibrated direction of the c-axis that is indicated by the red arrow by using the rotation angle between the specimen edge and the [001] direction [*i.e.*, (2) rotated by the blue arrow]. This result allowed us to determine the initial coordinates of the *c*-axis as the $(\cos\theta, \sin\theta, 0)$ vector. Then, the same process (*i.e.*, the rotation matrix) was applied to the result of *c*-axis (Fig. 5.4) deduced from the lattice image using Eq. (5.3), where the

α and β was substituted to $\alpha_0 - \alpha_2$ and $\beta_0 - \beta_2$, respectively. As a result, the direction of the c-axis is [0.02671, 0.9957, -0.08836] in the *x*-*y*-*z* coordinate system, which represents the crystal orientation of the specimen is slightly off the *y*-axis in the *x*-*y* plane (about 1.5 degrees), as indicated by the electron diffraction pattern [inset of Fig. 5.9(a)] *via* Fourier transform of the lattice image [Fig. 5.4(a)]. This is because the specimen position was not perfectly perpendicular to the electron beam (*i.e.*, the specimen rotated by α_0 and β_0) when acquiring the electron holograms. Nevertheless, the *c*-axis was aligned approximately parallel to the long axis of the thin-foil specimen; refer to the projection of the *c*-axis as indicated by the yellow arrow in Fig. 5.9(a).

5.3.2 Specimen thickness

In this study, the thickness distribution of the specimen was obtained by EELS. However, in principle, the phase image showing the contribution from mean inner potential (V_0) [Refer to the first term of Eq. (2.9)] can also provide the thickness map, as V_0 for $Nd_2Fe_{14}B$ is known [14]. The equation related to this is represented by

$$\phi_{elecric} = \sigma \int V_0\,(x, y, z)\,dz$$
$$= \sigma \cdot V_0 \cdot t\,(x, y), \qquad (5.4)$$

where σ stands for an interaction constant that depends on the acceleration voltage applied to the incident electrons. Figure 5.5(a) shows the

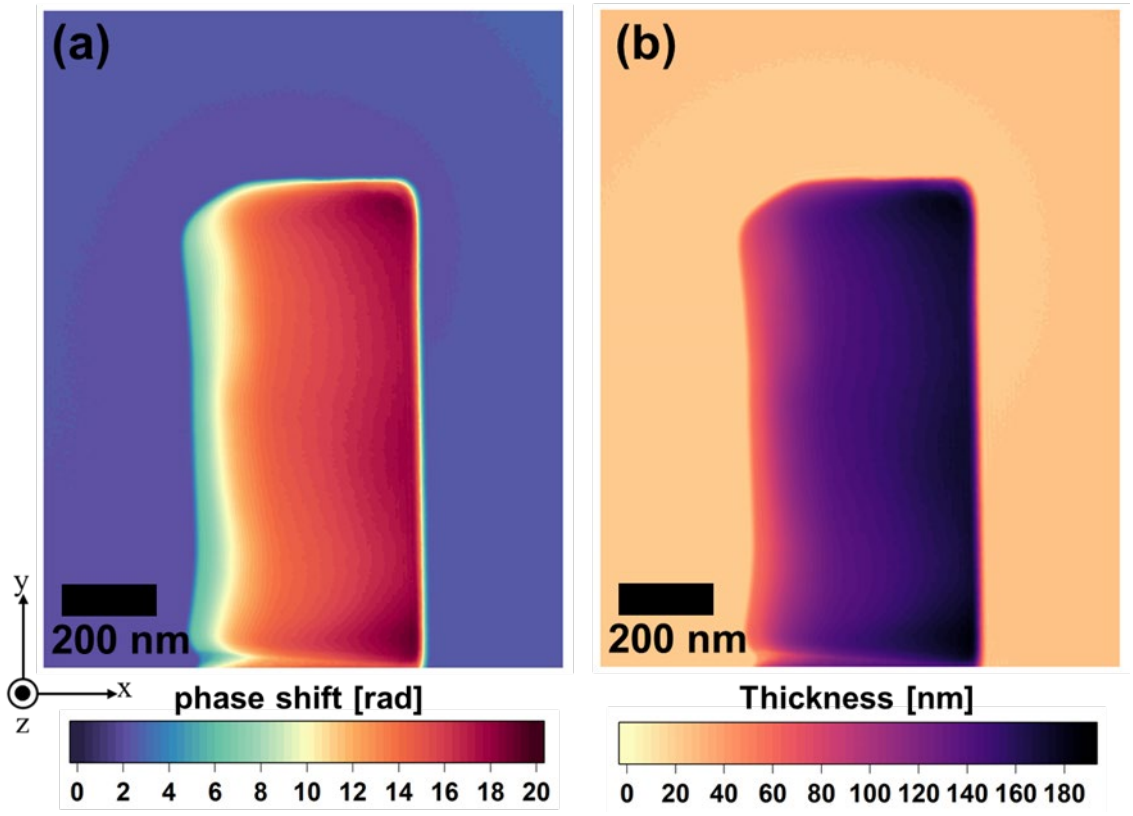

Fig. 5.5 (a)Reconstructed phase image representing the mean inner potential. (b) Distribution map showing specimen thickness given from (a).

reconstructed phase image representing V_0 in the thin-foil specimen. Unexpectedly, this phase image revealed undesired residual phase shift in the vacuum region, which appeared to be caused by the contact potential difference between the $Nd_2Fe_{14}B$ foil and the Mo support. For this problem, the specimen thickness of Fig. 5.5(b) given from Fig. 5.5(a) seems to be overestimated than the real values in t. Therefore, the specimen thickness was determined by EELS, for which λ in the $Nd_2Fe_{14}B$ thin-foil specimen was evaluated by cross-sectional observation and simulations as follows.

Figure 5.6(a) is a backscattered electron - scanning electron microscope (BSE-SEM) image showing the cross-section of the specimen from which the electron holograms were collected. The cross-sectional observation straightforwardly determined the specimen thickness at the positions of a, b,

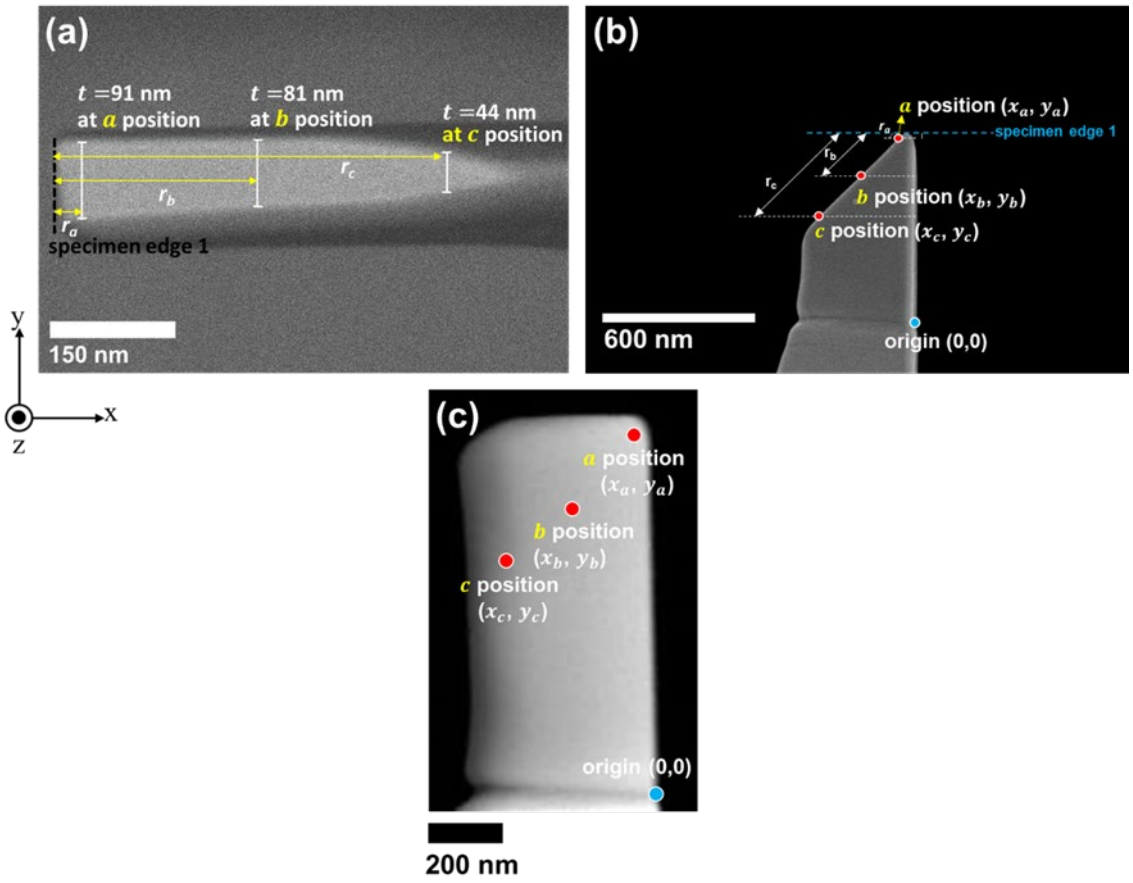

Fig. 5.6 Estimation of λ for a $Nd_2Fe_{14}B$ phase by electron holography observations. (a) BSE-SEM image providing the specimen thickness. (b) SEM image of the specimen that has been cut. (c) Log-ratio relative thickness map ($=\frac{t}{\lambda}$) by EELS, equal to Fig. 5.1(b). The origin of the *x*-*y*-*z* coordinate system is corresponding to the right bottom of the specimen indicated by the blue circle in (b) and (c).

and *c* as shown in Fig. 5.6(a). The distance between specimen edge 1 and three-position (*i.e.*, *a*, *b*, and *c* positions) represents r_a, r_b and r_c, respectively. Figure 5.6(b) shows a SEM image of the specimen that had been cut when the projection direction to the specimen in Fig. 5.6(b) is corresponding to that in Fig. 5.1. The three-positions of *a*, *b*, and *c* positions could be placed in the specimen with reference to the distance of r_a, r_b and r_c, as shown in Fig. 5.6(b). We assume that the origin of the *x*-*y*-*z* coordinate system corresponds to the right bottom of the specimen indicated by the blue circle

in Figs 5.6(b) and (c), so that the *y*-axis can be parallel to the right edge of the specimen, which was also applied to a model specimen explained in the next subsection. Based on this coordinates system, the coordinates each for the a, b and c positions were evaluated as (x_a, y_a), (x_b, y_b) and (x_c, y_c), respectively, which was adopted to the log-ratio relative map of Fig. 5.6(c) [equal to the Fig. 5.1(b)]. Following the operation, λ at three-position could be calculated by using the information of t given from Fig. 5.6(a) and the map representing t/λ of Fig. 5.6(c). In the first step to find the optimized value for λ, the author used one value for λ that is derived from the *c* position, *i.e.*, $\lambda =$ 60.6 nm. Then, the phase gradient ($= \frac{\partial \Delta\phi_B}{\partial x}$) in the *x* direction was calculated with reference to the crystal orientation, the thickness variation of the specimen given from $\lambda =$ 60.6 nm by simulations (ViewField, ELF corp.) that allows for obtaining the phase shift due to vector

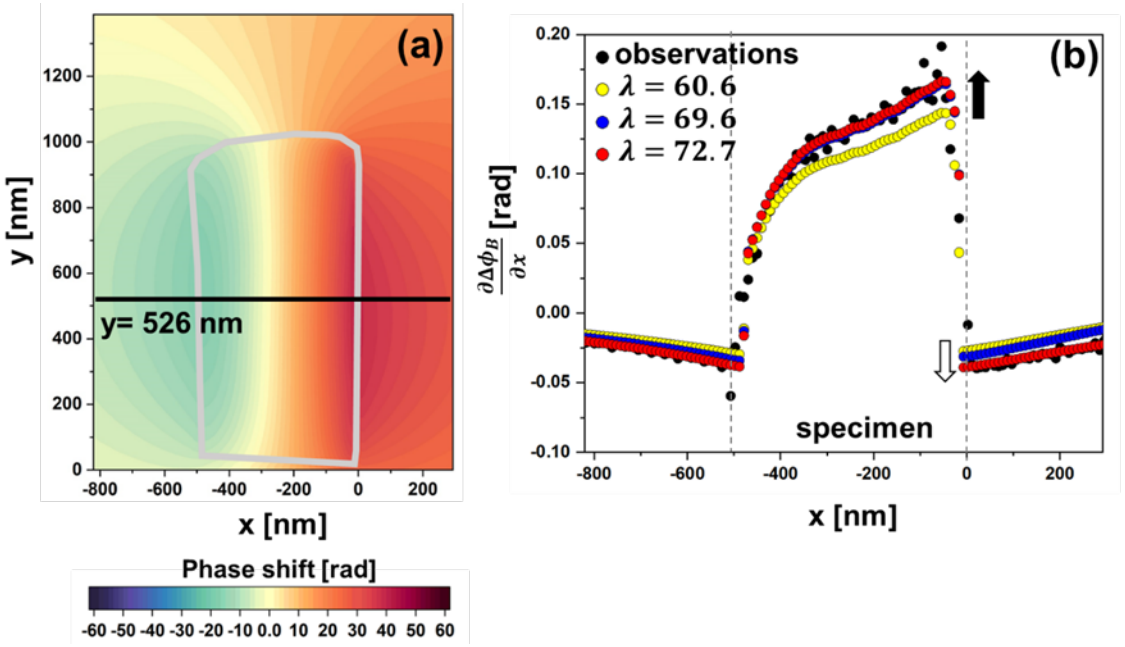

Fig. 5.7 Determination of λ using simulations. (a) Reconstructed phase image of the thin-foiled $Nd_2Fe_{14}B$ specimen. (b) Plots of phase gradient ($= \frac{\partial \Delta\phi_B}{\partial x}$) in the observations and simulations, measured along $y =$ 526 nm.

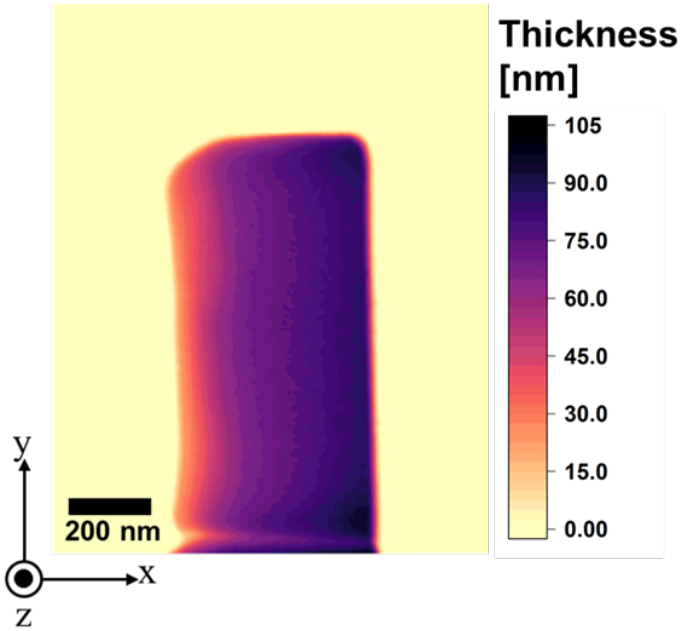

Fig. 5.8 Thickness variation of the specimen by EELS and λ (=72.7) determined in this study.

potential. The calculated phase gradient was investigated along a line at $y =$ 526 nm, as shown in Fig. 5.7(a) that is the reconstructed phase image, that is, electron holography observation representing $\Delta\phi_B$ (discussion about the phase image will be addressed in the next subsection). Figure 5.7(b) shows the plots of observations and simulations. The yellow plots (for $\lambda =$ 60.6) are quietly far away the black plots (observations) in both of specimen and vacuum regions, which may have occurred due to measurement errors in the process of determining the coordinates of *a*, *b* and *c* in Figs. 5.6(b) and (c) based on the cross-sectional observation of Fig. 5.6(a) with reference to the distance from specimen edge, *i.e.*, r_a, r_b and r_c. Therefore, λ should improve as the simulation plot approaches the black plot of in the observations. The operation for improvement of λ was performed, as indicated by the black and white arrows in Fig. 5.7(b), *i.e.*, the simulation plots moving up in the specimen region and moving down in the vacuum. As a result, the mean free

path of inelastic scattering in the $Nd_2Fe_{14}B$ phase was evaluated to be 72.7 nm as presented in the red plots in Fig. 5.7(b). The variation of the specimen thickness could be revealed by EELS with λ determined in this study, as shown in Fig. 5.8.

5.3.3 Calculation of three-dimensional magnetic field using the modeled specimen

Figure 5.9(a) shows a TEM image of the thin-foil specimen, equal to 5.2(a), from which electron holograms were acquired. With reference to the *x*-*y*-*z* coordinate system given in Fig. 5.9, the foil plane was assumed to be parallel to the *x*-*y* plane, while the electron incidence is in the $-z$ direction. As described in subsection 5.3.1, the coordinate and direction of c-axis was evaluated to be [0.02671, 0.9957, −0.08836] in the *x*-*y*-*z* coordinate system and approximately parallel to the long axis of the thin-foil specimen, as indicated by the diffraction pattern and the yellow arrow in Fig. 5.9(a). The thickness map of the specimen shown in Fig. 5.8 was obtained by EELS with λ of $Nd_2Fe_{14}B$ phase estimated in this study, as described in subsection 5.3.2. These electron microscopy observations allowed for the construction of a model specimen made of small polyhedral meshes (*i.e.,* 4.7×4.7 nm^2 in the *x*-*y* plane), as shown in Fig. 5.9(b), which approximates the thin-foil specimen in terms of the shape, size, thickness variation, and crystal orientation. The magnetic-field distribution in this model specimen was calculated in three dimensions for the cuboidal region (1113×40000×1388 nm^3) indicated by the letters E, F, F_0, E_0, R, S, S_0, and R_0 in Fig. 5.9(c). Note that, the origin of the *x*-*y*-*z* coordinate system corresponds to the right bottom

of the specimen, so that the *y*-axis can be parallel to the right edge of the specimen, as shown schematically in Fig. 5.9(d). This model specimen was employed to determine the three-dimensional distribution of magnetic field for $\Delta\phi_M$ and $\Delta\phi_M$. For this performance, the phase map of $\Delta\phi_B$ induced by the model specimen was evaluated with the electron holography observation, which is discussed in the next subsection.

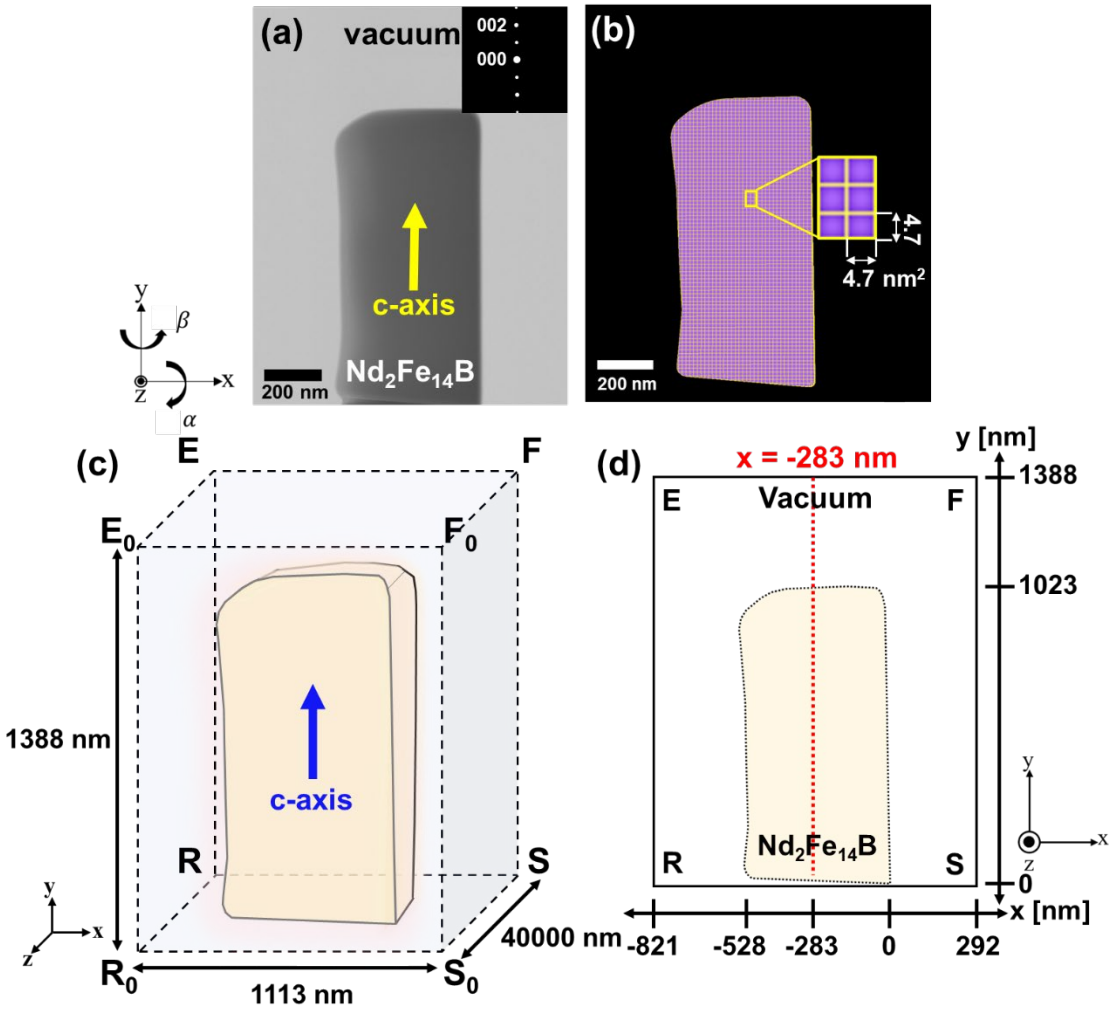

Fig. 5.9 Thin-foil specimen comprised of single crystalline $Nd_2Fe_{14}B$ prepared using FIB. (a) TEM image of the thin-foil specimen and electron diffraction pattern (inset). The yellow arrow indicates the projection of the *c*-axis in the *x*-*y* plane. (b) Model specimen used in three-dimensional calculations of the stray magnetic field outside of the specimen. (c) Volume for which the stray magnetic field was calculated using the model specimen in (b). (d) Area in which the phase images in Fig. 5.10 are revealed.

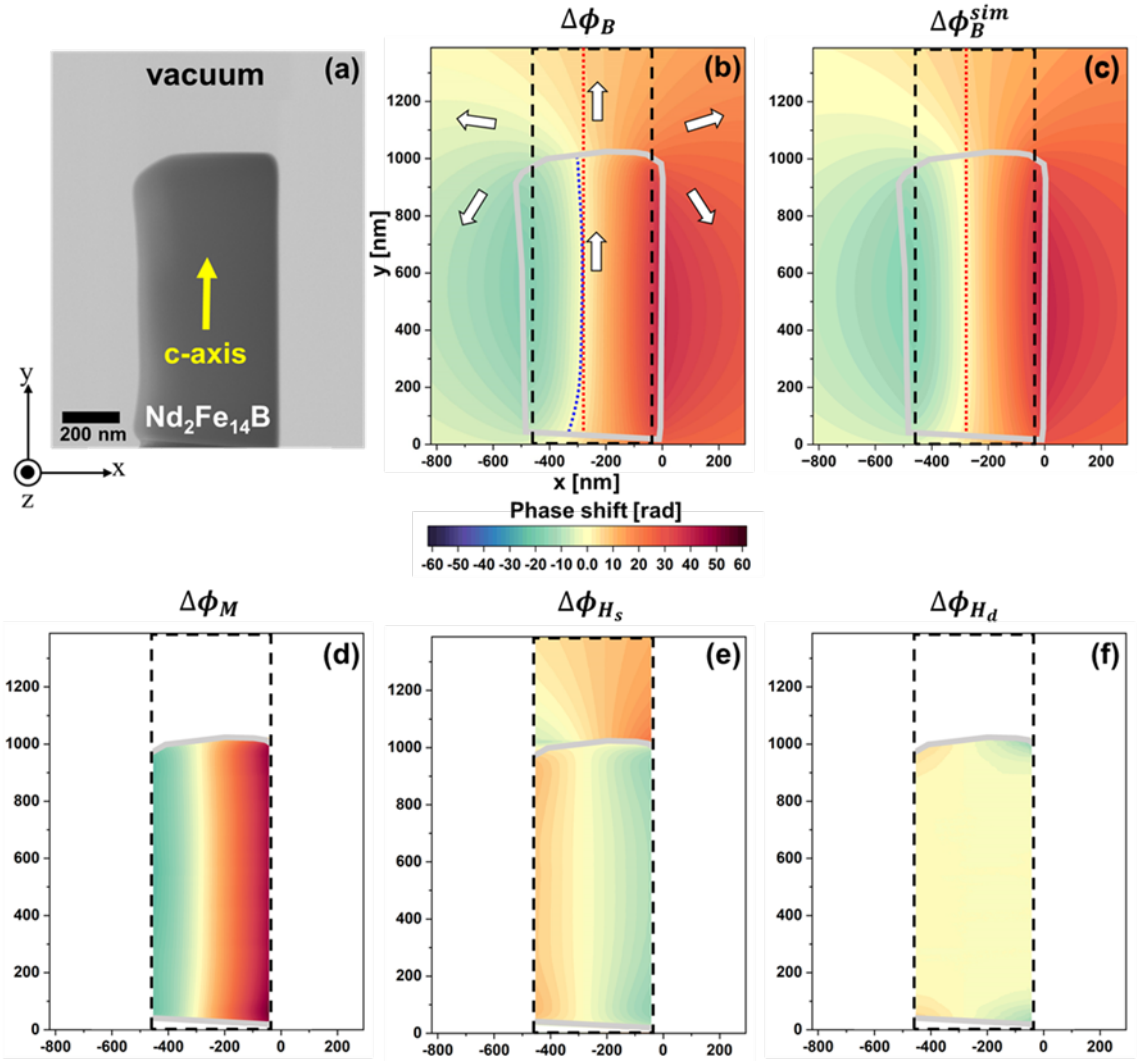

Fig. 5.10 Demagnetization field revealed using electron holography observation of a thin-foil $Nd_2Fe_{14}B$ specimen. (a) TEM image of the thin-foil specimen, which is identical to Fig. 5.9(a). (b) Phase image of $\Delta\phi_B$ revealed by electron holography. (c) Calculation of $\Delta\phi_B$, which shows good agreement with the phase image in (b). (d) Phase image of $\Delta\phi_M$ deduced from the magnetization vector determined by TEM observations. (e) Phase image of $\Delta\phi_{H_s}$ that was calculated using the model specimen in Fig. 5.9(b). (f) Phase image of $\Delta\phi_{H_d}$ determined for the thin-foil specimen. The phase images in (d)-(f) are presented in the area indicated by the black dotted lines in (b) and (c).

5.3.4 Visualizing phase information approximating H_d

Figure 5.10(b) shows the reconstructed phase image representing $\Delta\phi_B$ (*i.e.,* the electron holography observation) acquired from the field of view shown in Fig. 5.10(a), which is identical to Fig. 5.9(a). The phase shift is represented by colors, based on the color scale in Fig. 5.10. The phase map reasonably explains that the specimen is magnetized in the *y* direction; the white arrows in Fig. 5.10(b) indicate the directions of magnetic flux both in the specimen region (bordered by grey lines) and the outskirt vacuum region. The result of the simulation [$\Delta\phi_B^{sim}$, Fig. 5.10(c)] using the model specimen was in good agreement with the observation ($\Delta\phi_B$) in Fig. 5.10(b). The result implies that use of the model specimen in Fig. 5.9(b) can be useful for the prediction of $\Delta\phi_M$ and $\Delta\phi_{H_s}$, and accordingly to have the approximation of $\Delta\phi_{H_d}$. Note that $\Delta\phi_B^{sim}$ was calculated by the surface integral expressed by Eq. (5.5) in terms of the *y* component of magnetic flux density B_y:

$$\Delta\phi_B = -\frac{e}{\hbar}\iint B_y\,(x,y,z)dxdz, \qquad (5.5)$$

where e and $\hbar$ represent the elementary charge and Planck's constant divided by 2π, respectively. The red dotted lines in Fig. 5.10(c) and in Fig. 5.9(d) indicate the start position (*i.e.,* reference position) of the surface integral for each slice of the *x*-*z* plane. The red dotted lines thus represent the trace of the reference positions P_0 and P as defined in Chapter 3. For convenience in calculations, the red dotted line was fixed at the position of $x = -283$ nm, so that the red dotted line is closed to an equiphase line (*i.e.,* a

line along which $\Delta\phi_B = 0$) within the thin-foil specimen, as indicated by the blue dotted line in Fig. 5.10(b). Regarding the simulation in Fig. 5.10(c), to determine the offset in the phase shift (*i.e.,* to determine the initial value of $\Delta\phi_B^{sim}$ in the red dotted line at $x = -283$ nm), the author referred to the values of phase shift in Fig. 5.10(b) that were determined by experiment. This offset enables a thorough analysis using the simulation [Fig. 5.10(c)], which should be compared with the observation [Fig. 5.10(b)].

Figure 5.10(d) provides the phase image relevant to the *y* component of magnetization ($\Delta\phi_M$) calculated using Eq. (5.6).

$$\Delta\phi_M = -\frac{e}{\hbar}\iint \mu_0 M^y\,(x,y,z)dxdz, \qquad (5.6)$$

where μ_0 and M^y stands for the permeability of vacuum and the *y* component of magnetization: refer to the *x*-*y*-*z* coordinate system in Fig. 5.9. The surface integral was performed with reference to the TEM observations of the specimen shape, the thickness variation, and the orientation of the *c*-axis (*i.e.,* easy magnetization axis indicating the magnetization vector). Note that $\Delta\phi_M$ was plotted for the limited area closed by the black dotted lines in Fig. 5.10, as we can disregard the artificial gap of the phase (*i.e.,* discontinuity of the phase) caused by the surface integral using Eq. (5.6) across the specimen border (both the left and right borders of the specimen), which was explained as the technical problems for the method using the surface integral in Chapter 3 and 4. As demonstrated using the artificial specimen in Chapter 4, the sense of the phase gradient in Fig. 5.10(d) is

positive (*i.e.*, increase of the value of phase shift) in the *x* direction because the specimen is magnetized along the *y* direction. Figure 5.10(e) shows the phase image that represents the contribution of the stray magnetic field ($\Delta\phi_{H_s}$) outside of the specimen, which was calculated using Eq. (5.7) applied to the model specimen in Fig. 5.9(b):

$$\Delta\phi_{H_s} = -\frac{e}{\hbar}\iint \mu_0 H_s^y\,(x,y,z)dxdz, \qquad (5.7)$$

where H_s^y represents the *y* component of the stray magnetic field that exists outside the specimen. Again, the result was plotted for the limited area closed by the black dotted lines. Within the area where the specimen exists [*i.e.,* the lower area in Fig. 5.10(e)], the sense of the phase gradient is negative (*i.e.*, decrease of the value of phase shift) in the *x* direction. This result is also attributed to the stray magnetic field directed opposite to the direction of magnetization. Figure 5.10(f) shows a phase map relevant to the demagnetization field ($\Delta\phi_{H_d}$) within the thin-foil specimen, representing the subtraction of $\Delta\phi_M + \Delta\phi_{H_s}$ [summation of Figs. 5.10(d) and 5.10(e)] from the phase image ($\Delta\phi_B$) in Fig. 5.10(b) determined experimentally. As demonstrated for the artificial specimen, the phase gradient is significant in the regions near the specimen edge, while there is only a negligible change in the phase in the inner area of the thin-foil specimen. The results indicate the effectiveness of this method. Note that the offset in the surface integral [*i.e.,* the initial value of the phase at the reference point P indicated by the red dotted line in Fig. 5.9(d)] was incorporated in the calculations of Fig.

5.10(d) (for the region inside of the specimen) and Fig. 5.10(e) (for the region outside of the specimen). Therefore, in the phase plot of Fig. 5.10(f), which represents the subtraction of $\Delta\phi_M + \Delta\phi_{H_s}$ from $\Delta\phi_B$, we simply assumed that there is no contribution from the offset. In other words, the plots for $\Delta\phi_{H_d}$ at the reference points have zero value. However, for more precise analysis about $\Delta\phi_{H_d}$using a real specimen having an irregular shape, we need further considerations about the offset: this point remans a challenge in this phase analysis.

5.3.5 Visualizing the demagnetization field distribution

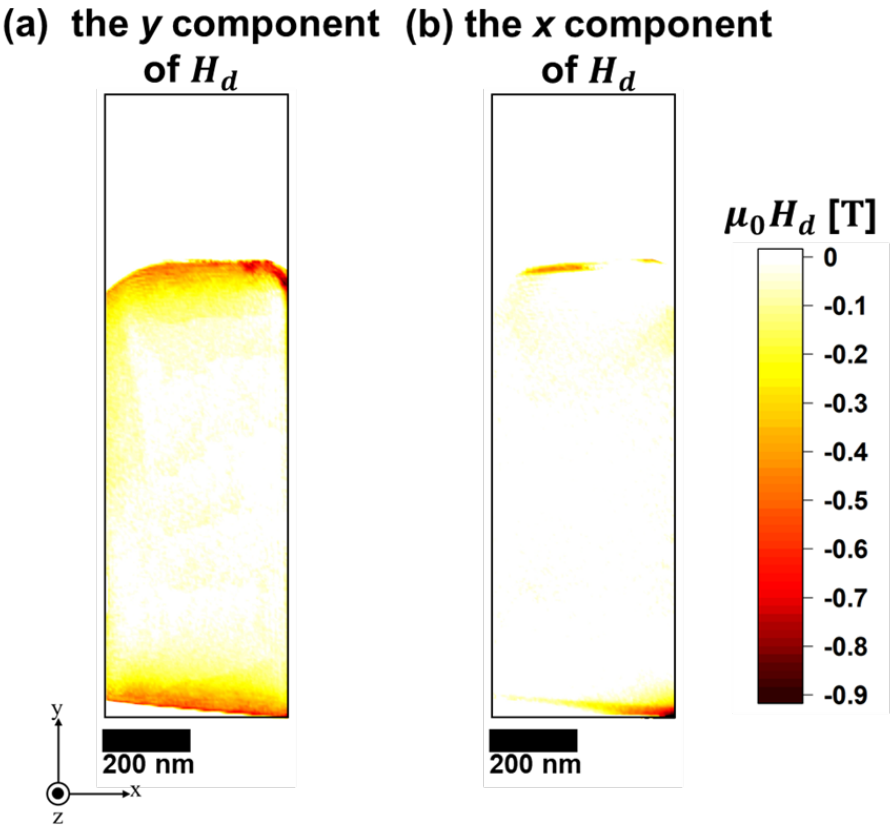

Fig. 5.11 Mapping of demagnetization field within the thin-foil $Nd_2Fe_{14}B$ specimen deduced from this method. (a) showing the plots for the *y* component of H_d. (b) showing the plots for the *x* component of H_d.

The application of Eq. (5.8) [1] with $\Delta\phi_{H_d}$ in Fig. 5.10(f) allowed the y component of the demagnetization field ($\mu_0 H_d^y$) within the thin-foil specimen to be plotted, as shown in Fig. 5.11(a). The area shown in Fig. 5.11(a) is identical to those indicated by the dotted lines in Fig. 5.10.

$$\mu_0 H_d^y = -\frac{\partial \Delta\phi_{H_d}}{\partial x} \cdot \frac{\hbar}{e} \cdot \frac{1}{t}. \qquad (5.8)$$

As predicted by the classical electromagnetism, the demagnetization field (oriented in the $-y$ direction) can be maximized in the positions near the upper and lower specimen edges, although there is only a negligible amount of demagnetization field in the inner region of the thin-foil specimen. It is noted that the gradient of $\Delta\phi_{H_d}$ in the y direction could reveal a map of the x component of the demagnetization field by using Eq. (5.9).

$$\mu_0 H_d^x = \frac{\partial \Delta\phi_{H_d}}{\partial y} \cdot \frac{\hbar}{e} \cdot \frac{1}{t}. \qquad (5.9)$$

However, when the rectangle-shaped specimen was magnetized in the y direction, the x component of demagnetization field was too small to allow for comprehensive discussion, as shown in Fig. 5.11(b). Therefore, for further discussion on H_d , we focus on the y component of the demagnetization field observed in the area enclosed by the blue line in Fig. 5.12(a) that is equal to Fig. 5.11(a). This area is enlarged in Fig. 5.12(b). The

magnitude of $\mu_0 H_d^y$ at the position labeled as #1 was evaluated to be -0.38 T, where the negative value represents the magnetic field that is directed to the $-y$ direction. The map of $\mu_0 H_d^y$ indicates that the demagnetization field is enhanced at the right side of position #1, while it is reduced at the left side. The result can be explained by the wedge-shaped cross section of the thin-foil specimen prepared using FIB, as shown in Fig. 5.9(a). With regard to the variation in the y direction (*i.e.*, toward the midpoint of the specimen), the magnitude of $\mu_0 H_d^y$ at position #2 (75 nm from position #1) was reduced to -0.14 T. The value of $\mu_0 H_d^y$ was further reduce to -0.034 T at position #3, which was 146 nm from #1. It should be noted that the rate of reduction in $\mu_0 H_d^y$ can be explained by a power law of r^{-2}, where r is the distance from the magnetic charge (magnetic pole), as predicted by classical electromagnetism [15]. This result also shows the usefulness of this method to extract the demagnetization field from reconstructed phase images.

For further examination of $\mu_0 H_d^y$, Fig. 5.12(c) provides the result of micromagnetic simulation (*i.e.*, Landau-Lifshitz-Gilbert calculations [16,17]) obtained using the commercial EXAMAG LLG code (Fujitsu). The simulation was performed using another model specimen that approximated the actual thin-foil specimen in terms of the shape, size, thickness variation, and crystal orientation. The model specimen, which was also made of many small polyhedra, was produced using Hyper Works software (Altair Engineering). As input magnetic parameters for the $Nd_2Fe_{14}B$ phase, the exchange stiffness constant and the magnetocrystalline anisotropy were assumed to be 12 pJ m^{-1} and 4.5 MJ m^{-3}, respectively [18,19]. In terms of the distribution of the demagnetization field within the specimen, the simulation

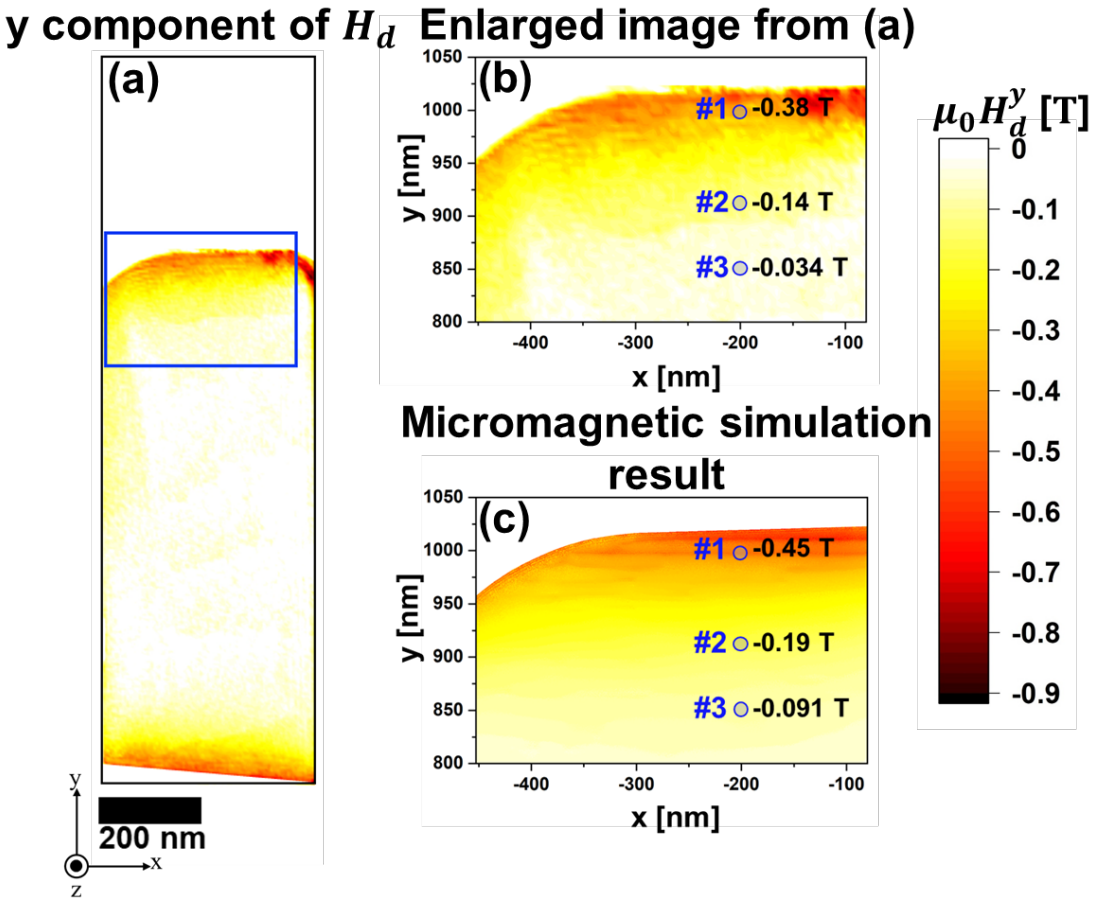

Fig. 5.12 Evaluation of *y* component of the demagnetization field ($\mu_0 H_d^y$) in the thin-foil $Nd_2Fe_{14}B$ specimen. (a) Plot of the *y* component of the demagnetization field within the thin-foil specimen, which is equal to Fig. 5.11(a). (b) Enlargement of the area enclosed by the blue line in (a). (c) Result of micromagnetic simulation.

in Fig. 5.12(c) shows good agreement with the observation in Fig. 5.12(b). The simulation reproduced (1) the demagnetization field, which is affected by the wedged specimen shape, and (2) a reduction rate of $\mu_0 H_d^y$ that could be explained by a power law of r^{-2}, both of which were observed experimentally. There were slight deviations in the values of $\mu_0 H_d^y$ that were measured at positions #1, #2, and #3. In this examination, the values of $\mu_0 H_d^y$ determined by electron holography were smaller than the predictions by the micromagnetic simulation. A plausible source of the deviations is the

ambiguity in the determination of the foil thickness, crystal orientation, and other geometric parameters in the specimen. We should also consider the effect of a surface damage layer that may be induced by polishing with FIB. Nevertheless, the observation of $\mu_0 H_d^y$ agrees with the simulation within an accuracy of $<$0.065 T.

5.4 Summary

In this chapter, the effectiveness of the method was demonstrated using the electron holography observation for the single-crystalline $Nd_2Fe_{14}B$ thin-foil. The analysis on the direction of *c*-axis in the specimen was performed by the TEM observations (*i.e.*, the electron diffraction pattern and the lattice image), as referring to the rotation matrix. The mean free path for inelastic scattering in the $Nd_2Fe_{14}B$ phase was evaluated to be 72.7 nm by the complex analysis using the cross-sectional observation by electron microscopy and the simulations. With this result, the distribution map of specimen thickness could be obtained by EELS. Through various electron microscopy observations, the model specimen that approximated the actual thin-foil specimen could be made with reference the specimen shape, the direction of c-axis, and the variation of specimen thickness. The validity of the model specimen for determining $\Delta\phi_M$ and $\Delta\phi_{H_s}$ was verified by comparing the electron holography observation and the calculated phase image of $\Delta\phi_B$ given from the three-dimensional distribution of magnetic fields using the model specimen. The phase information approximating H_d was visualized by the application of this method (*i.e.*, by reducing the calculated phase components of $\Delta\phi_M$ and $\Delta\phi_{H_s}$ from the electron holography observation),

which deduced the plot of the demagnetization field. For further discussion about the *y* component of H_d, the plot for H_d was in good agreement with the predictions from both classical electromagnetism and micromagnetic simulations. The results indicate the usefulness of the method that was applied to examinations using a single-crystalline specimen, although we need an approximately rectangular specimen to reduce uncertainties in the data processing related to the offset in phase shift.

Chapter 5 References

1. E. Völkl, L. F. Allard, and D. C. Joy (1999) *Introduction to Electron Holography.* (Kluwer Academic/Plenum Publishers, New York.)

2. A. Tonomura (1999) *Electron Holography (2nd ed.).* (Springer, Heidelberg)

3. J. Thielsch, D. Suess, L. Schultz, and O. Gutfleish (2013) Dependence of coercivity on length ratios in sub-micron $Nd_2Fe_{14}B$ particles with rectangular prism shape. *J. Appl. Phys.* 114: 223909.

4. J. Li, Lihua Liu, H. Sepehri-Amin, Xin Tang, T. Ohkubo, N. Sakuma, T. Shoji, A. Kato, T. Schrefl, and K. Hono (2018) Coercivity and its thermal stability of NdFeB hot-deformed magnets enhanced by the eutectic grain boundary diffusion process. *Acta Mater.* 161: 171-181.

5. M. Grönefeld and H. Kronmüller (1989) Calculation of strayfields near grain edges in permanent magnet material. *J. Magn. Magn. Mater.* 80: 223-228.

6. S. Bance, B. Seebacher, T. Schrefl, L. Exl, M. Winklhofer, G. Hrkac, G. Zimanyi, T. Shoji, M. Yano, N. Sakuma, M. Ito, A. Kato, and A. Manabe (2014) Grain-size dependent demagnetizing factors in permanent magnets. *J. Appl. Phys.* 116: 233903.

7. J. Fidler and T. Schrefl (1996) Overview of Nd-Fe-B magnets and coercivity. *J. Appl. Phys.* 79: 5029-5034.

8. J. Fidler and T. Schrefl (2000) Micromagnetic modelling-the current state of the art. *J. Phys. D: Appl. Phys.* 33: R135.

9. H. Sepehri-Amin, T. Ohkubo, M. Gruber, T. Schrefl, and K. Hono (2014) Micromagnetic simulations on the grain size dependence of coercivity in anisotropic Nd-Fe-B sintered magnets. *Scr. Mater.* 89: 29-32.

10. W. Li, Q. Zhou, L. Z. Zhao, Q. X. Wang, X. C. Zhong, and Z. W. Liu (2018) Micromagnetic simulation of anisotropic grain boundary diffusion for sintered Nd-Fe-B magnets. *J. Magn. Magn. Mater.* 451: 704-709.

11. T. Malis, S. C. Cheng, and R. F. Egerton (1988) EELS log-ratio technique for specimen-thickness measurements in the TEM. *J. Electron Microsc. Tech.* 8: 193-200.

12. K. Harada and A. Tonomura (2004) Double-biprism electron interferometry. *Appl. Phys. Lett.* 84: 3329.

13. G. G. Slabaugh (1999) Computing Euler angles from a rotation matrix. *Retrieved on August* 6: 39-63.

14. Y. Murakami, K. Niitsu, S. Kaneko, T. Tanigaki, T. Sasaki, Z. Akase, D. Shindo, T. Ohkubo, and K. Hono (2016) Strain measurement in

ferromagnetic crystals using dark-field electron holography. *Appl. Phys. Lett.* 109: 193102.

15. K. M. Krishnan (2016) *Fundamentals and applications of magnetic materials.* (Oxford Univ. Press, New York.)

16. T.L. Gilbert (1955) A Lagrangian formulation of the gyromagnetic equation of the magnetization field. *Phys. Rev.* 100: 1243.

17. L.D. Landau and E. M. Lifshitz (1935) On the theory of the dispersion of magnetic permeability in ferromagnetic bodies. *Phys. Z. Sowjet.* 8: 153–169.

18. K. Hono and H. Sepehri-Amin (2012) Strategy for high-coercivity Nd-Fe-B magnets. *Scr. Mater.* 67: 530-535.

19. Y. Toga, M. Nishino, S. Miyashita, T. Miyake, and A. Sakuma (2018) Anisotropy of exchange stiffness based on atomic-scale magnetic properties in the rare-earth permanent magnet $Nd_2Fe_{14}B$. *Phys. Rev. B* 98: 054418.

6. Toward the precision improvement in phase-shift analysis: application of noise reduction with the wavelet hidden Markov model to electron holography observations

6.1 Introduction

To attain the observation of demagnetization field (H_d), which is crucial for both electron microscopy and the magnetic material engineering, this study proposed the method that allows the phase imaging due to H_d (*i.e.*, visualizing the phase shift due to H_d, $\Delta\phi_{H_d}$) for the magnetic material specimen using the electron holography observation corresponding to the reconstructed phase image (Chapter 3). Subsequently, the method was evaluated to demonstrate the validity and effectiveness by the applications to the artificial and real specimens composed of the single crystal $Nd_2Fe_{14}B$ grain (Chapters 4 and 5). The plots for H_d deduced from the method could be considered reasonable as discussed along with the prediction of classical electromagnetism and the micromagnetic simulation. However, this method requires the manifold analyses including the subtraction and differential operation for the phase images to obtain the $\Delta\phi_{H_d}$ and H_d, respectively, which may deteriorate the accuracy in the mapping of $\Delta\phi_{H_d}$. When considering the solutions to enhance the quality of the phase image $\Delta\phi_{H_d}$, a technique of noise reduction can contribute to the precision improvement of the method for the in-depth discussion on H_d.

To reduce the noise in the phase image, the author used the image processing that is a useful technique to decrease the noise without any

changes in optical and/or interferometry parameters when taking the electron hologram. Among the image processing techniques, the wavelet thresholding (*i.e.*, the wavelet transform of the images to which thresholds are applied) [1] is a useful and conventional noise reduction. This method eliminates the noise which is lower than the value of the threshold. However, this conventional noise reduction causes a critical problem that also removes the weak signal than the threshold. To solve this problem, Midoh and Nakame [2] established the wavelet hidden Markov model (WHMM) which is a type of the noise reduction from electron microscopy images (including electron holograms and reconstructed phase images) using the wavelet transform. An essential point is that WHMM allows for separating the weak signal from the noise with a sufficiently high probability, based on the approach of the optimization problem in information science [2]. Indeed, Tamaoka et. al. [3] demonstrated the effectiveness of the noise reduction using WHMM in the electron holography observations from the $LaFeO_3/SrTiO_3$ film. These studies imply that WHMM can be as well promising for the phase-shift analysis associated with the mapping of $\Delta\phi_{H_d}$, which was demonstrated in the previous chapters. It is expected that the noise reduction using WHMM can be effective especially for $Nd_2Fe_{14}B$ specimens, which (on many occasions) provide only a poor contrast of electron holograms due to the strong absorption of electrons by the heavy elements Nd. The noise reduction can be accordingly beneficial to the process using image subtraction/differential as employed in the mapping of $\Delta\phi_{H_d}$. However, WHMM has not yet been applied to electron holography studies on $Nd_2Fe_{14}B$ thin foils.

The aim of this chapter is to assess the effectiveness of the noise reduction

using WHMM in the phase-shift analysis of $Nd_2Fe_{14}B$ thin-foils. This examination is essential for the future applications of WHMM to the precision improvement in the method that extracts the H_d information from electron holography observations. For this purpose, electron holograms were acquired from a $Nd_2Fe_{14}B$ thin-foil specimen. In this case, as mentioned later in detail, the spacing (s_{obj}) of interference fringes in the electron hologram can be an essential factor representing the image quality. Indeed, the fringe spacing is important parameter for the interferometry system because a high spatial resolution in the phase image can be attained when the value of s_{obj} is small [4]. Note that this narrow fringe spacing deteriorates the visibility of the electron hologram, which determines the phase detection limit [5]. In other words, the phase analysis can be less precise due to the reduced visibility derived from the narrow s_{obj}. To overcome this dilemma between the interferometric parameter, such as s_{obj}, and the phase resolution, the noise reduction was applied to the experimental data (*i.e.*, the electron holography observations) with varying the fringe spacing, and the noise-reduced results were mainly discussed in terms of the discontinuity in the phase shift induced from the low visibility in this chapter.

6.2 Methods

6.2.1 Noise reduction using the wavelet hidden Markov model

For ease of understanding of the wavelet transform and the essence of WHMM, we shall refer to the wavelet transform using a one-dimensional spectrum. Figure 6.1(a) shows a spectrum that can be expressed using several wavelets with different frequencies and amplitudes. When the wavelet

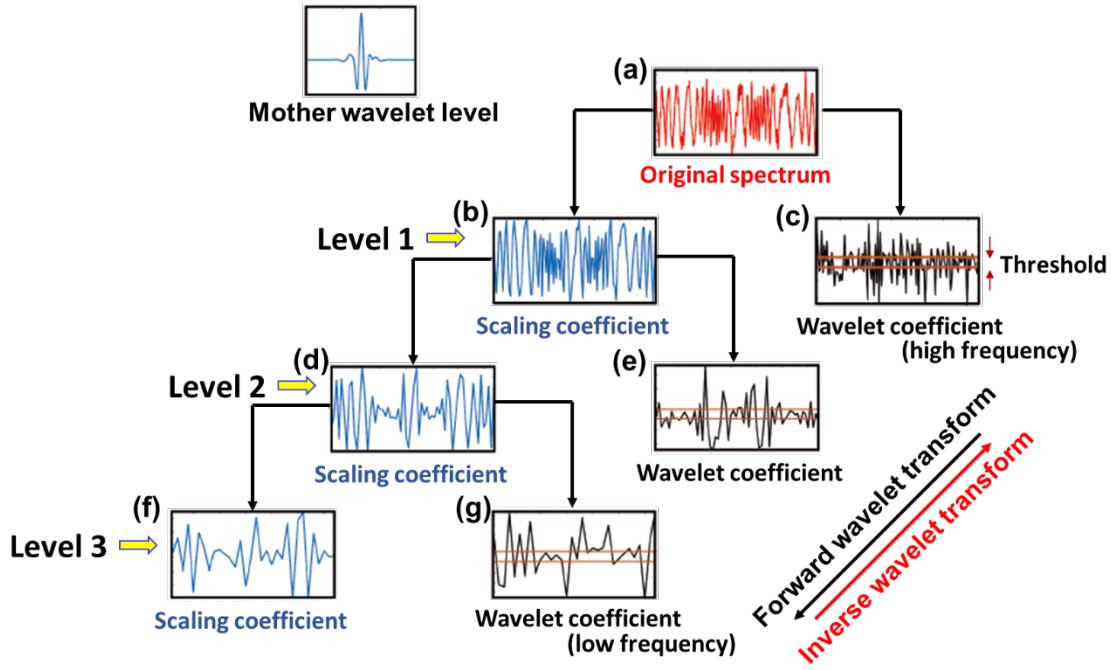

Fig. 6.1 Overview of wavelet transform for one-dimensional spectrum. (a) Original spectrum. (b) and (c) Scaling and wavelet coefficient at Level 1. (d) and (e) Scaling and wavelet coefficient at Level 2. (f) and (g) Scaling and wavelet coefficient at Level 3 [6].

transform is applied to the original spectrum shown in Fig. 6.1(a) using a type of the mother wavelet as shown in the inset, the original spectrum is resolved into a scaling coefficient of Fig. 6.1(b) representing the original shape of the spectrum, and a wavelet coefficient of Fig. 6.1(c) representing the contribution of the wavelet at individual pixels. Figures 6.1(b) and (c) can be considered as data series generated by the wavelet transform at Level 1, in which the wavelet transform was conducted with reference to a specific frequency of the mother wavelet. Subsequently, the wavelet transform to produce the scaling and the wavelet coefficient is repeated with reference to lower frequencies of the mother wavelet, as schematized in Figs 6.1(d)-(g). In the illustration shown in Fig. 6.1, the wavelet transform was carried out for three conditions (three different frequencies) of the mother wavelet, which are respectively presented as Level 1, Level 2, and Level 3. This

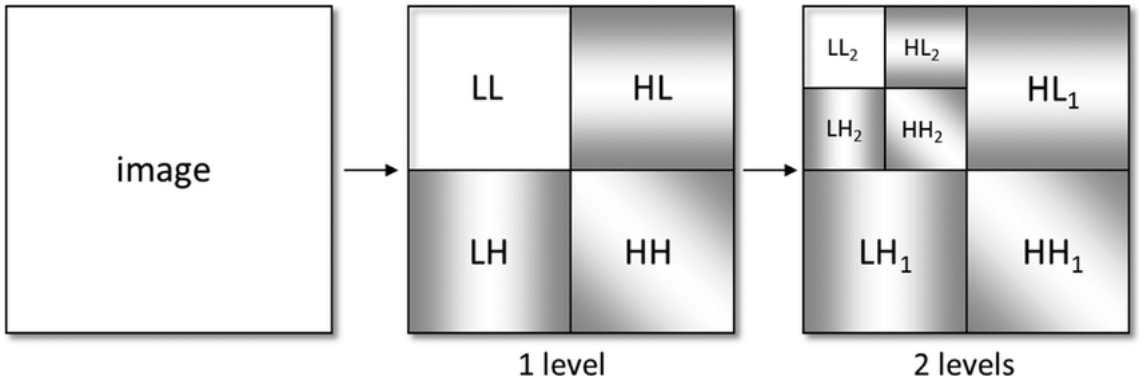

Fig. 6.2 Illustrative example for two-dimensional wavelet transform [7].

process represents the forward wavelet transform. Importantly, the original spectrum can be reproduced using the inverse wavelet transform, as indicated by the red arrow in Fig. 6.1. When a threshold is applied to each level of the wavelet coefficient, during the inverse transform, the wavelet coefficient smaller than the threshold is not reflected in the reproduction of the original spectrum. In other words, noise in the spectrum can be reduced through the application of the threshold in the inverse wavelet transform. This is the essence of noise reduction using a wavelet transform. In the conventional method of noise reduction using the wavelet transform, the threshold (T_{TH}) can be represented by the general expression using the standard deviation of the wavelet coefficients (σ) and the number of sampling (N_0):

$$T_{TH} \approx \sigma\sqrt{2\ln N_0}. \qquad (6.1)$$

However, as mentioned earlier, this conventional method reduces not only noise, but also weak signals below the threshold.

The problems in the conventional thresholding method also arise in the

noise reduction using the two-dimensional wavelet transform. Figure 6.2 schematizes the two-dimensional wavelet transform applied to an image, where LL represents the scaling coefficient, and others (*i.e.*, LH, HL and HH) represents the distribution of the wavelet coefficients for the vertical, horizontal, and diagonal directions, respectively. Again, the noise can be reduced via the inverse wavelet transform by applying the threshold to each wavelet coefficient in LH, HL and HH components, whereas the signal weaker than the threshold are lost.

To improve the method of noise reduction in this study, a wavelet hidden Markov model that was reported by Midoh and Nakamae [2] was employed to distinguish between a weak signal and noise. To explain the concept of WHMM, Fig. 6.3 schematically shows as to how the image size (or number of image pixels) is reduced by the forward wavelet transform: *i.e.*, from top to bottom. Similarly, Fig. 6.3 shows how the image size (or number of image pixels) is increased by the inverse wavelet transform: *i.e.*, from bottom to top. When the inverse wavelet transform using a two-dimensional image is referred to, one pixel (S_i) at the bottom level (S_0 at Level 3) corresponds to four pixels at the upper level (S_1, S_2, S_3 and S_4 at Level 2). Importantly, in WHMM, each pixel at all levels has two hidden states, which are represented

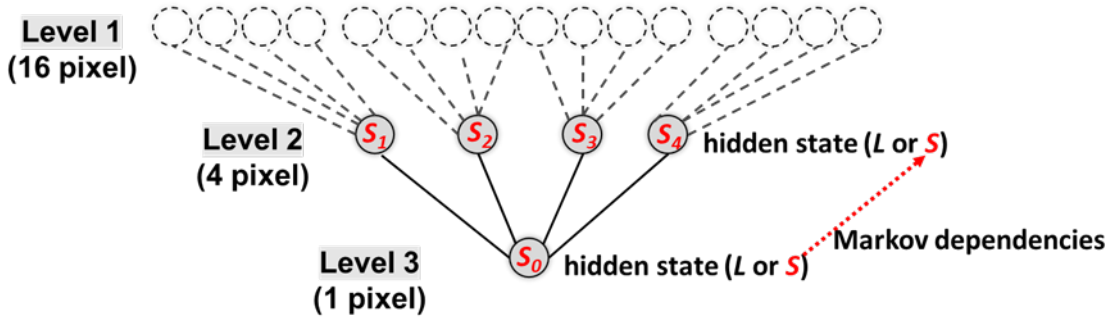

Fig. 6.3 Schematic diagram showing the noise reduction using WHMM. S_0 indicates one pixel at Level 3, which is corresponding to S_1, S_2, S_3 and S_4 at Level 2. L and S are the hidden state representing the noise and signal, respectively.

as L and S, respectively. The hidden state S produces noise with a high probability, whereas the hidden sate L produces signal with a high probability. With regard to the hidden state S, as shown in Fig. 6.4(a), the probability to attain the wavelet coefficient w_i is expressed by a Gaussian function $g(w)$ (as a function of the wavelet coefficient) whose standard deviation is small. This sharp Gaussian function allows for only a limited range of the wavelet coefficient that is achieved by experiments, and accordingly represents the signal. In contrast, with regard to the hidden state L, as shown in Fig. 6.4(b), the probability to attain the wavelet coefficient w_i is expressed by a Gaussian function $g(w)$ whose standard deviation is large. The broad Gaussian function well explains the dispersion of noise components which exist over a wide range of the wavelet coefficient. Note that WHMM assumes the state probability σ_S, representing that one pixel (to be considered for all pixels in all levels) occupies the hidden state S with the probability σ_S. In addition, this pixel occupies the hidden state L with the probability σ_L. An essential point in WHMM is, when the hidden state S is dominant in one pixel of Level 3, this dominance can be inherited by the inverse wavelet transform to the corresponding, upper pixels in Level 2 with a high probability ε. This tendency (*i.e.*, inheriting the dominance to the upper level) represents the Markov property. For simplicity, those probability parameters are referred to as the Markov parameters θ. The parameters θ should be optimized using the Baum-Welch algorithm [8,9] (one of the expectation-maximization algorithm) so that the values of the parameters explain well the wavelet coefficients w_i in all the pixels, which were determined by the analysis using the experimental observation.

Once the Markov parameters are optimized by the Baum-Welch algorithm,

the nose reduction can be performed for all the pixels by using the expression of Eq. 6.2. This equation related the wavelet coefficient after the noise reduction w_i' with the original coefficient w_i [2].

$$w_i' = \sum_{m=1}^{M} p(S_i = m|w, \theta) \frac{\sigma_{i,m}^2}{\kappa\sigma_n^2 + \sigma_{i,m}^2} w_i. \qquad (6.2)$$

Here, i identifies the pixels, m indicates one of the hidden states (the hidden state S or L), $p(S_i = m|w, \theta)$ is the state probability (a type of condition probability) to takes the hidden state m (S or L) when the wavelet coefficient w and the set of the Markov parameter θ are given. σ_n^2 is the variance of wavelet coefficients in HH in the first Level of the wavelet transform (refer to Fig. 6.2). κ is the denoising factor related to the strength of noise

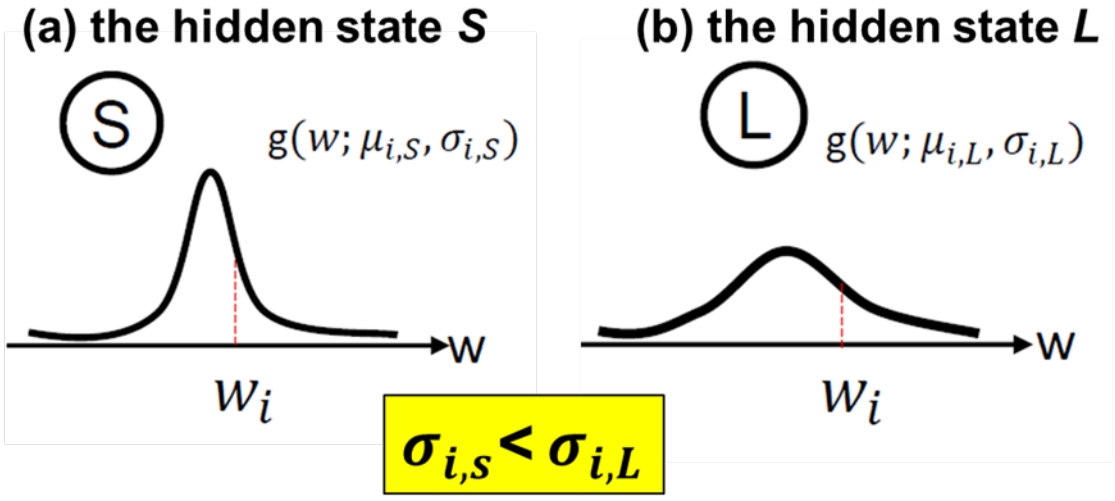

Fig. 6.4 Principle of the noise reduction with reference to WHMM. (a) Variance of the wavelet coefficient $\sigma_{i,S}$ with low value in the hidden state S, which contributes the strong noise reduction. (b) Variance of the wavelet coefficient $\sigma_{i,L}$ with high value in the hidden state *L*, which contributes the negligible noise reduction.

reduction. $\sigma_{i,m}^2$ is the variance of the wavelet coefficient given S_i is in the state m, and this is also one of the Markov parameters that can be optimized by the Baum-Welch algorithm. Consequently, we could identify pixels which have a significant probability as noise pixels. Strong noise reduction attributed to low $\sigma_{i,s}$ was applied to pixels representing noise (the hidden state *S*), as shown in Fig. 6.4(a). In contrast, only negligible noise reduction attributed to high $\sigma_{i,m}^2$ was applied to the other pixels representing the signal (the hidden state *L*), as presented in Fig. 6.4(b). For details about the principal and practically evaluation of WHMM, refer to [2].

In this study, a mother wavelet "farras wavelet" was used for the two-dimensional wavelet transform. The noise reduction was applied not to electron holograms as the raw data, but to the complex images *(i.e.*, both real part and the imaginary part) that were obtained by Fourier transform of the electron holograms. This is because WHMM applied to electron holograms attains the noise reduction for a limited range of frequencies, while the application to the complex images results in the noise reduction for a wide frequency range. In what follows, the real and the imaginary parts are abbreviated as $\Re$ and $\Im$, respectively.

6.2.2 Specimen preparation and electron holography observation

A thin-foil $Nd_2Fe_{14}B$ specimen was used to evaluate the denoising effect with reference to the wavelet hidden Markov model. A system of focused ion beam / scanning electron microscope (FIB/SEM; Helios G4 UX, FEI Co.) in National Institute for Materials (NIMS) was exploited to provide a poly-crystalline rectangle-shaped block, including grain boundaries (GBs) and a

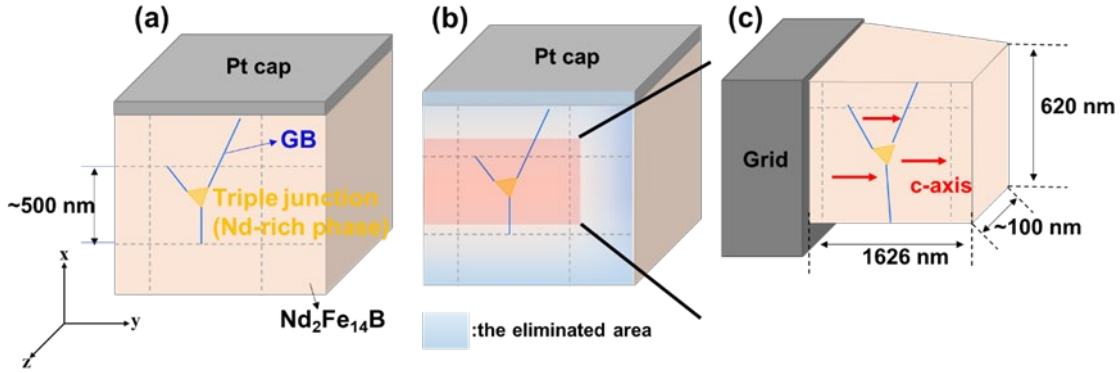

Fig. 6.5 Schematic illustrations representing the process to prepare a thin-foiled $Nd_2Fe_{14}B$ specimen by FIB. (a) Poly-crystalline rectangle-shaped block. (b) Polishing (a) into a thin foil. Blue areas in (b) indicates the eliminated area during the shaping. (c) Thin-foil $Nd_2Fe_{14}B$ specimen subjected to polishing at low acceleration voltages to reduce the surface damage.

triple junction made of a Nd-rich phase, as shown in Fig. 6.5(a) (the gray dotted line indicates an artificial damaged line to remark the positions within the specimen). Then, the rectangular block was polished into a thin foil using another FIB instrument (MI4000L, Hitachi Ltd.) in the Ultramicroscopy Research Center (URC) of Kyushu University, while some areas near the specimen edges presented by the blue areas in Fig. 6.5(b) were lost during the shaping. To reduce surface damage, the foil was polished at low acceleration voltages (5 kV and 2 kV) using Ga ion beam at the final stage of specimen preparation. Following the operation by various FIB instruments, the thin-foil $Nd_2Fe_{14}B$ specimen shown in Fig. 6.5(c) was obtained. The thin-foiled area corresponds to the region marked with the red in Fig. 6.5(b). The crystal orientations (the direction of *c*-axis of grains) in the *x*-*y*-*z* coordinates system are nearly parallel to the long-axis of the rectangular foil in the *y* direction indicated by the red arrows in Fig. 6.5(c). The incidence of electron beam is $-z$ direction.

Fig. 6.6 External view of electron holography (HF-3300X, Hitachi Ltd.) [13].

Electron holograms were acquired in various conditions of fringe spacing. To collect the data series with variable s_{obj}, the author used the double biprism system in the HF-3300X microscope in the URC of Kyushu University presented in Fig. 6.6, which allows the control of s_{obj} by controlling the voltage of the upper filament electrode (*i.e.*, the voltage of upper biprism, V_{BP1}), while the voltage of the lower filament electrode (*i.e.*, the voltage of lower biprism, V_{BP2}) is constant (refer to [10] for details about the control of interference parameters including s_{obj} in the double biprism system). With reference to this operation, the electron holograms were acquired at $V_{BP1} = -50$ V, -70V, -90V, -110V, -130V, and -150V, which attained the values of s_{ob} at 5.2 nm, 3.7 nm, 2.9 nm, 2.5 nm, 2.1 nm, and 1.7 nm, respectively. For all holograms, the electron exposure time (t_a) was 3.0 s. The variation of s_{obj} affected the visibility of electron holograms, at the expense of the coherency of electron waves (in addition to other factors)

as described in later. Results of applying the noise reduction to these observations are also presented in the next section. The holograms were recorded using a high-sensitivity camera (K3 IS camera, Gatan Inc.) that can identify the individual electrons as discrete counts at a particular pixel, as leading up to the improved visibility of the hologram compared to using the slow-scan charge-coupled-device (CCD) camera [11].

6.3 Results and discussion

6.3.1. Visibility of electron holograms depending on fringe spacing

Figure 6.7 shows the observed visibility (V), which is defined as Eq. (6.3), of electron holograms as function of the fringe spacing s_{obj}.

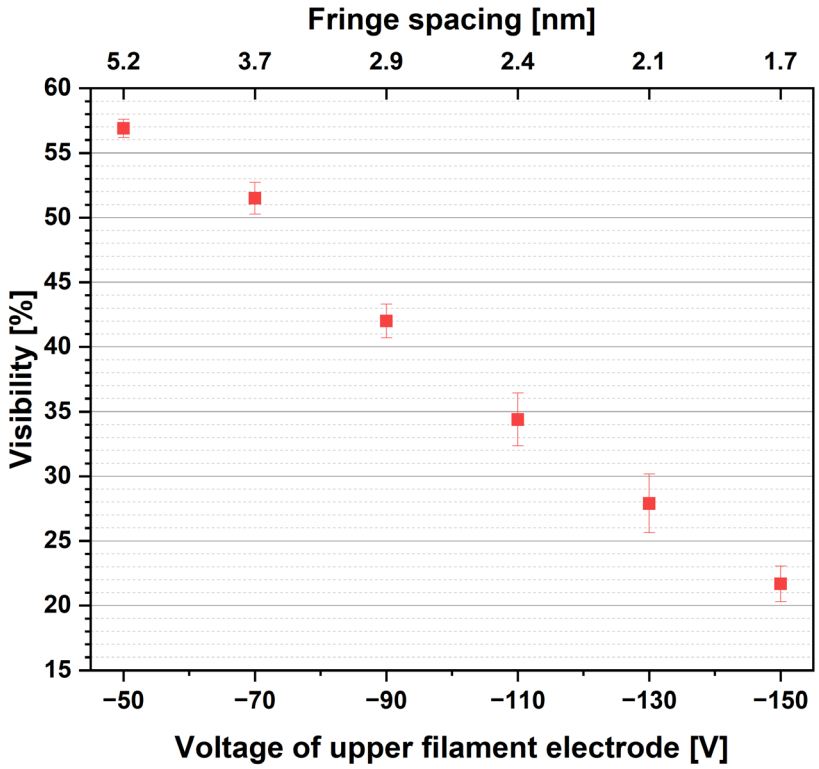

Fig. 6.7 Visibility of electron holograms as function of the fringe spacing

$$V = \frac{I_{max} - I_{min}}{I_{max} + I_{min}}, \qquad (6.3)$$

where, I_{max} and I_{min} represents the peaks and troughs of the fringe profile. As the fringe spacing decreased, V gradually decreased, which can be explained by Eq. (6.4):

$$V = V_0(t) \times S_0(\widehat{N_o}) \times MTF(k_0). \qquad (6.4)$$

Here, $V_0(t)$ is the time-dependent part of visibility raised from instrument instabilities that are slower than the fastest exposure time. $S_0(\widehat{N_o})$ is the spatial coherence envelope of the wavefield as a function of the average number of incident electrons per pixel (N_0) per unit time (t), $\widehat{N_o}$ ($= \frac{N_0}{t}$). $MTF(k_0)$ is the modulation transfer function (MTF) of the camera at the fringe spatial frequency k_0. The relationship indicates that, in addition to the coherency of electrons, MTF affects the visibility of electron holograms when the fringe spacing is narrow.

The impact of s_{obj} on the visibility could be revealed in the reconstructed phase image (*i.e.*, electron holography observations) shown in Fig. 6.8. Figure. 6.8(a) is a transmission electron microscopy (TEM) image of the thin-foil $Nd_2Fe_{14}B$ specimen, for which the electron holograms were acquired. Figures 6.8 (b)-(c) show the reconstructed phase images representing the phase shift (ϕ) of incident electron waves that is defined as follows:

$$\phi = \sigma \int V(x,y,z)\, dz - \frac{e}{\hbar} \int A_z(x,y,z)\, dz, \qquad (6.5)$$

where σ, $V(x,y,z)$, e, $\hbar$ and $A_z(x,y,z)$ stand for an interaction constant that depends on the acceleration voltage applied to the incident electrons, the electrostatic scalar potential, the elementary charge, Planck's constant divided by 2π and the z component of the vector potential, respectively. Here, the z direction is corresponding to the electron incidence. The change in the phase is presented by colors with respect to the color bar in Fig 6.8. The position of specimen borders is indicated by the white dotted lines. As the fringe spacing was reduced [*i.e.*, in the order of (b), (c), and (d) in Fig. 6.8], the population of the artificial phase discontinuities (indicated by the abrupt change in colors) increases. The values of s_{obj} are 2.4 nm, 2.1 nm,

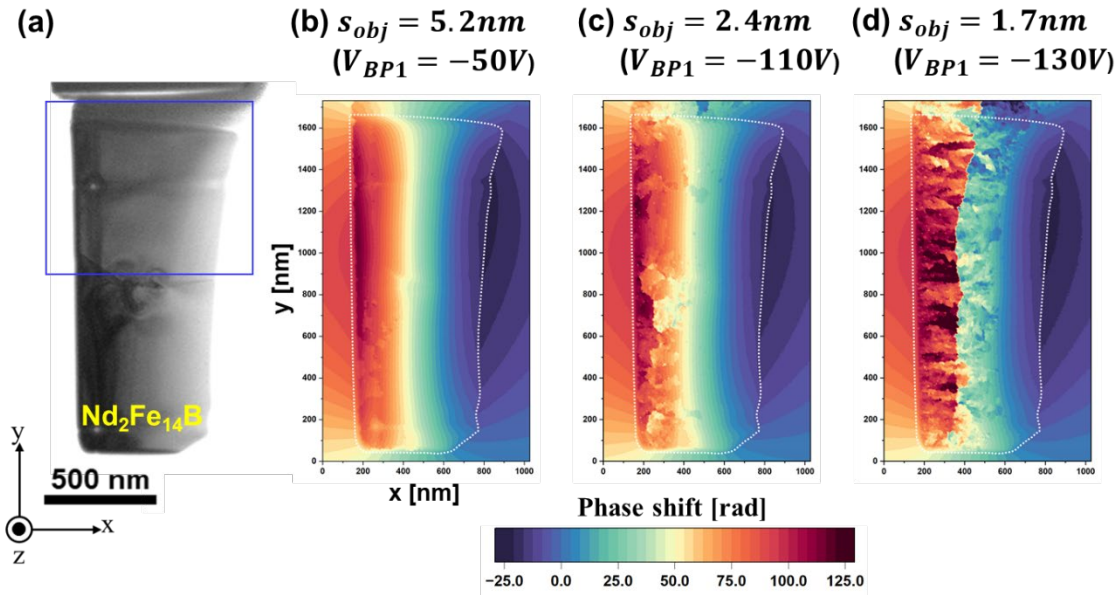

Fig. 6.8 Reconstructed phase images representing phase shift ϕ. Area indicated by the blue lines in (a) is corresponding to the areas in Fig. 6.9. (a) TEM image of the $Nd_2Fe_{14}B$ thin-foil specimen. (b)-(d) Phase images subjected to s_{obj} = 5.2 nm, 2.4 nm, and 1.7 nm, respectively.

and 1.7 nm, respectively. The artificial phase discontinuities, which are produced by the process of phase retrieval using Fourier transform, are due to the poor visibility of electron holograms. Note that the specimen thickness is not uniform, but the right region of the foil (with reference to the presentation in Fig. 6.8) is thicker than that of the left region. Accordingly, as the visibility of holograms is poor in the thick region, many phase discontinuities are observed in the thick region of the specimen.

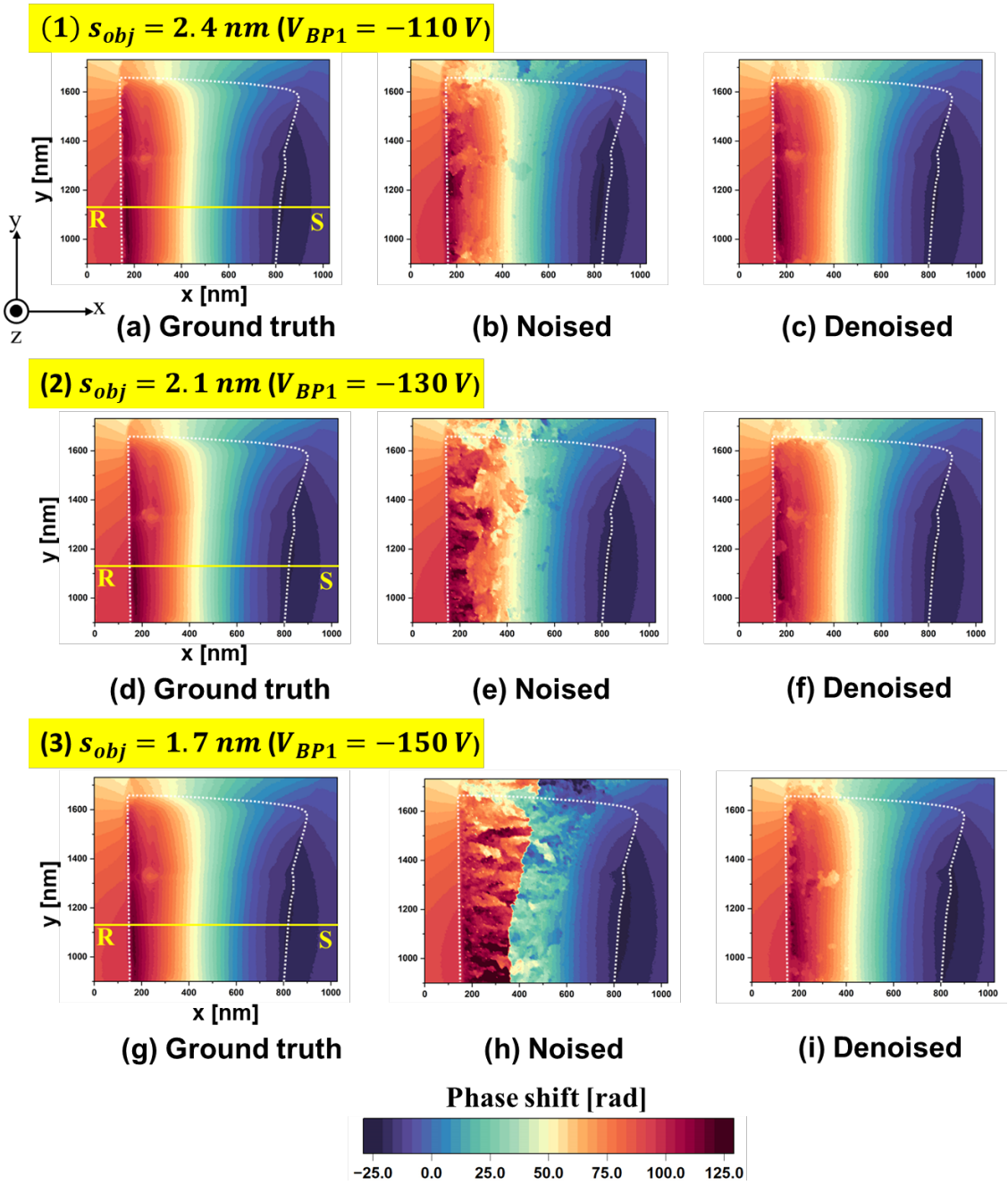

Fig. 6.9 Data series of phase images collected in three conditions of fringe spacing (1) s_{obj} = 2.4 nm, (2) s_{obj} = 2.1 nm, and (3) s_{obj} = 1.7 nm. (a), (d) and (g) Ground truth images for (1), (2) and (3) conditions, respectively. (b), (e) and (h) Original phase image for (1), (2) and (3) conditions, respectively, to which the noise reduction using WHMM has not applied. (c), (f) and (i) Phase images after applying the noise reduction to (b), (e) and (h), respectively.

6.3.2. Evaluation of noise-reduced images subjected to WHMM

Figure 6.9 shows data series of phase images collected in three conditions of fringe spacing: (1) $s_{obj} = 2.4$ nm, (2) $s_{obj} = 2.1$ nm, and (3) $s_{obj} = 1.7$ nm. The area shown in Fig. 6.9 is identical to the region closed by the blue lines in Fig. 6.8(a). In Fig. 6.9, "ground truth" represents the phase images having only negligible phase discontinuities. Practically, the ground truth images were obtained by a long electron exposure to improve the image quality of electron holograms: *i.e.*, in this study, the exposure time t_a was determined at 15 s. These ground truth images [Figs. 6.9 (a), (d), an d (g)] will be used to calculate the peak signal-to noise ratio (*PSNR*) in the later part of this subsection. Figures 6.9(b), (e) and (h) represent the original phase images to which the noise reduction by WHMM was not yet been applied: see the images labelled by "Noised" in each series of observations. Figures 6.9(c), (f) and (i) provide the phase images after the noise reduction using WHMM. As mentioned in the above subsection, the narrow fringe spacing results in many phase discontinuities within the reconstructed phase images, as shown in Figs. 6.9(b), (e), and (h). However, the phase discontinuity distributed in the specimen area could be reduced by applying the noise reduction method using WHMM, as shown in Figs. 6.9(c), (f), and (i) Although the phase discontinuities could not be completely removed, the effectiveness of the noise reduction is clearly shown in Fig. 6.9.

For further examinations, the phase shift was measured in the position indicated by the R-S line shown in Fig. 6.9. The plots of the phase shift ϕ are presented in Fig. 6.10. Note that Fig. 6.10 (a) plots three sorts of line profiles that were respectively measured in the phase images of Figs. 6.9 (a), (d), and (g). Similarly, Fig. 6.10 (b) and Fig. 6.10 (c) present the plots from

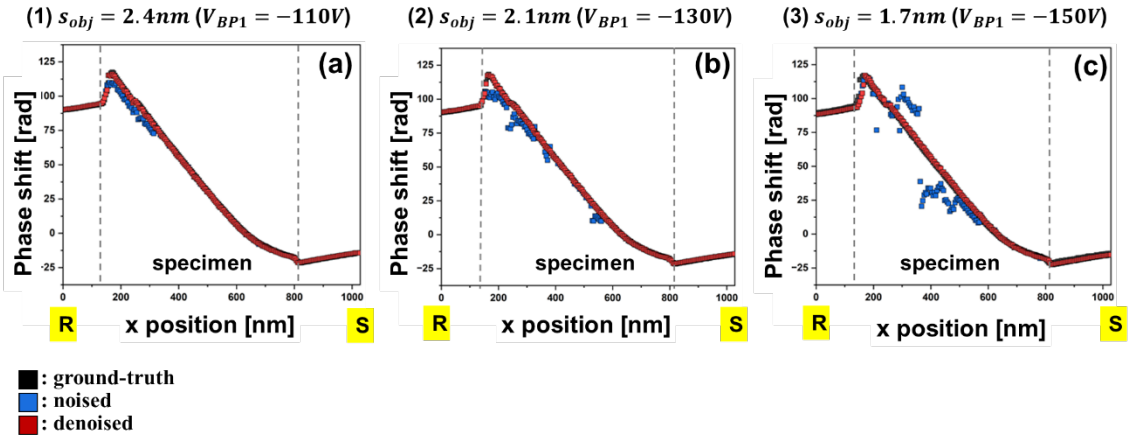

Fig. 6.10 Plots of the phase shift ϕ measured along R-S line in Fig. 6.9 for (a) s_{obj} = 2.4 nm, (b) s_{obj} = 2.1 nm, and (c) s_{obj} = 1.7.

Figs. 6.9 (b), (e), (f) and Figs. 6.9 (c), (f), (i), respectively. In Fig. 6.10, the blue dots representing the electron holography observation scatter significantly as the fringe spacing becomes narrow. In contrast, all the red plots representing the results after noise reduction appear to be smooth showing only negligible scattering. These results show the effectiveness of the noise reduction, which allows the precision improvement of phase analysis providing the improved phase images with the denoised ϕ plots.

Furthermore, the author evaluated the denoised phase images in terms of the peak signal-to noise ratio (*PSNR*) defined as follows:

$$PSNR = 20 \cdot \log_{10}\left(\frac{255}{\sqrt{1/MN\sum_{i=1}^{M}\sum_{j=1}^{N}\left(I(i,j)-G(i,j)\right)^2}}\right), \qquad (6.6)$$

where $I(i,j)$ and $G(i,j)$ are the pixel value of the evaluated phase image and the ground truth phase image at the coordinate i,j with a size of $M \times N$

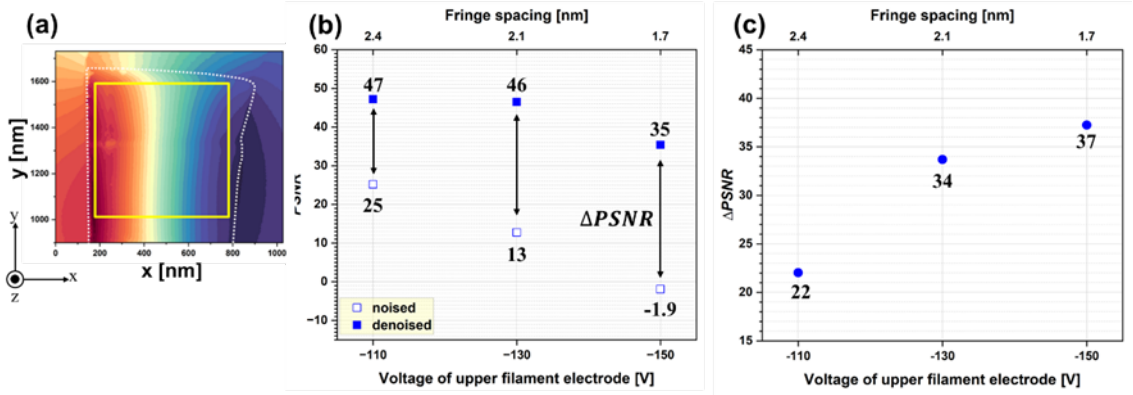

Fig. 6.11 Evaluation of noise reduction in terms of PSRN. Area indicated by the yellow lines in phase image of (a) represents the area for PSNR calculation. (b) PSNR as function of the biprism voltage V_{BPI} (lower horizontal axis) that determines the fringe spacing s_{obj} (upper horizontal axis). (c) Difference of PSNR between noised (in original phase images) and denoised plots (in phase images of applying the noise reduction by WHMM to original images).

pixels [12]. The region that was referred to in the PSNR calculation was indicated by the yellow lines in Fig. 6.11(a). Figure 6.11(b) shows the results representing *PSNR* as function of the biprism voltage V_{BPI} (*i.e.*, lower horizontal axis) that determines the fringe spacing s_{obj} (*i.e.*, upper horizontal axis), where the open and closed plots indicate *PSNR* calculated from the noised phase image (*i.e.*, the original electron holography observation) and the denoised phase images, respectively. For the open plots in Fig. 6.11(b), *PSNR* at $s_{obj} = 1.7$ nm was reduced to -1.9, meaning that the signal was much weaker than the noise for the evaluated area. As a result of applying the noise reduction, all the closed plots in Fig. 6.11(b) show a noticeable improvement of *PSNR* compared with the open plots. For a more detailed evaluation, the difference of *PSNR* ($\Delta PSNR$) between noised and denoised plots was measured, as indicated by the black arrows in Fig. 6.11(b). Figure 6.11(c) represents the result of measuring $\Delta PSNR$ and shows that the largest improvement in terms of *PSNR* are obtained as estimated to be 37

at the narrowest s_{obj} (= 1.7 nm) resulting in the lowest visibility of electron hologram described in Fig. 6.7.

6.4 Summary

In this chapter, the effectiveness of the noise reduction was demonstrated by applying it to the electron holography observations (*i.e.*, the complex image reconstructed from the electron holograms) for the polycrystalline $Nd_2Fe_{14}B$ thin foil specimen. The noise reduction was performed by exploiting the wavelet hidden Markov model that can discriminate the signal even weaker than the threshold. The electron holograms were acquired depending on the fringe spacing. As the fringe spacing narrowed, the visibility of the holograms decreased, which led to increasing the discontinuity of the phase shift in the reconstructed phase images. The denoised ϕ plots were much improved than the noised ϕ plots originated from the reduced visibility with reference to the line profiles of plotting ϕ and the evaluations using *PSNR*. These results indicate that the noise reduction is promising tool for the precision improvement of phase analysis, which can be applied in the future to the method of extracting the phase imaging due to demagnetization field.

Chapter 6 References

1. M. Jansen (2012) *Noise reduction by wavelet thresholding*. (Springer Science & Business Media, New York)

2. Y. Midoh and K. Nakamae (2020) Accuracy improvement of phase

estimation in electron holography using noise reduction methods, *Microscopy* 69: 123-131.

3. T. Tamaoka, Y. Midoh, K. Yamamoto, S. Aritomi, T. Tanigaki, M. Nakamura, K. Nakamae, M. Kawasaki, and Y. Murakami (2021) Denoising electron holograms using the wavelet hidden Markov model for phase retrieval-Applicatiions to the phase-shifting method, *AIP adv.* 11: 025135.

4. M. Lehmann and H. Lichte (2002) Tutorial on off-axis electron holography, *Microsc. Microanal.* 8: 447-466.

5. A. Harscher and H. Lichte (1996) Experimental study of amplitude and phase detection limits in electron holography, *Ultramicroscopy* 64: 57-66.

6. Y. Midoh, K. Nakamae, H. Shinada, and Y. Murakami (2020) Noise reduction of electron holograms by using wavelet hidden Markov model, *顕微鏡* 552: 53-59.

7. L. Boubchir and B. Boashash (2013) Wavelet denoising based on the MAP estimation using the BKF prior with application to images and EEG signals, *IEEE Trans. sign. proc.* 61: 1880-1894.

8. L. E. Baum and T. Petrie (1966) Statistical inference for probabilistic functions of finite state Markov chains, *The annals of mathematical statistics* 37: 1554–1563.

9. L. E. Baum, T. Petrie, G. Soules, and N. Weiss (1970) A maximization technique occurring in the statistical analysis of probabilistic functions of Markov chains. *The annals of mathematical statistics* 41: 164-171.

10. K. Harada and A. Tonomura (2004) Double-biprism electron

interferometry. *Appl. Phys. Lett.* 84: 3329.

11. S. L. Chang, C. Dwyer, J. Barthel, C. B. Boothroyd, and R. E. Dunin-Borkowski (2016) Performance of a direct detection camera for off-axis electron holography, *Ultramicroscopy*, 161: 90-97.

12. S. Arora, J. Acharya, A. Verma, and P. K. Panigrahi (2008) Multilevel thresholding for image segmentation through a fast statistical recursive algorithm. *Pattern Recognition Letters* 29: 119-125.

13. https://www.hvem.kyushu-u.ac.jp/en/atomicscale.html

7. Conclusions

Electron holography (EH) is a powerful tool that enables us to observe the magnetic domain structure for a thin-foil specimen by measuring the phase shift of incident electron wave that has traversed the specimen. For magnetic materials, however, EH is only sensitive to magnetic flux density (B) that is perceived as the summation of magnetization (M), stray magnetic field (H_s) outside the specimen, and demagnetization field (H_d) inside the specimen. In other words, the discussion of H_d has been difficult for EH. Note that this problem was common for other methods of magnetic imaging that uses the electron probe, including Lorentz microscopy and differential phase contrast (DPC) microscopy. From an engineering viewpoint, the analysis on H_d is important for the research and development of sintered permanent magnets including the Nd-Fe-B magnet that is widely used in traction motors in electric/hybrid vehicles. Until now, the automobile industry has demanded a further improvement of the coercivity, which represents critical magnetic field to induce undesired magnetization reversal for the sintered magnet. Indeed, H_d is regarded to be a source for the undesired magnetization reversal. However, direct observation of H_d has been hampered because of the lack of the experimental tools.

To overcome the problem, in this study, the author developed a method that allows for extracting the phase information about H_d from EH observation, along with the sophisticated analysis using various electron microscopy observations and simulations. The validity of this method was examined via the application to an artificial bar magnet ($Nd_2Fe_{14}B$) shaped in a square

pillar. For further evaluations using an actual specimen, this method was applied to the mapping of H_d in a thin foil made of a single-crystalline $Nd_2Fe_{14}B$. The H_d map determined by this method showed a good agreement with the prediction by theories. On the other hand, this method requires the manifold analyses including the subtraction and differential operation for the phase images to obtain the $\Delta\phi_{H_d}$ and H_d, respectively, which may deteriorate the accuracy in the mapping of $\Delta\phi_{H_d}$. Therefore, toward the precision improvement of this method, the effectiveness of a noise reduction technique was assessed. In order to reduce the noise in the phase image, this study employed the wavelet hidden Markov model (WHMM) which allows a reasonable separation of weak signal from noise. It was demonstrated that WHMM could be effective for the noise reduction in the phase images acquired from a $Nd_2Fe_{14}B$ thin-foil, which provides a poor contrast of electron holograms due to the strong absorption of electrons by the heavy elements (*i.e.*, Nd element).

The achievements in this study are summarized as follows:

(1) A method was proposed to obtain the phase map representing H_d that was determined by using the EH observation showing the phase shift due to B ($\Delta\phi_B$). The phase map related to H_d ($\Delta\phi_{H_d}$) can be obtained by subtracting the undesired phase component due to M ($\Delta\phi_M$) and H_s ($\Delta\phi_{H_s}$) from $\Delta\phi_B$. When the crystallographic and morphological features of the specimen, such as the *c*-axis and the thickness of specimen, are unveiled by the observation of transmission electron microscopy (TEM), the three-dimensional distribution of the in-plane component (*i.e.*, the *y* component in this study) of M and H_s in the *x*-*y*-*z* coordinates system can be calculated in three

dimensions. Subsequently, $\Delta\phi_M$ and $\Delta\phi_{H_s}$ can be estimated using the surface integral for the *y* component of *M* and H_s multiplied by factors μ_0, *e*, and $\hbar$, whereμ_0, *e* and $\hbar$ stand for the vacuum permeability, elementary charge and Planck's constant divided by 2π. Consequently, the phase image of $\Delta\phi_{H_d}$ can be obtained by eliminating the contributions due to $\Delta\phi_M$ and $\Delta\phi_{H_s}$ from the EH observation representing $\Delta\phi_B$. Thus, a process to determine $\Delta\phi_{H_d}$ was formulated.

(2) Before the application of this process to the artificial and real specimens of $Nd_2Fe_{14}B$ [as mentioned in (3) and (4)], the authors have assessed this method from a theoretical viewpoint. Since this process uses the surface integral with reference to the *y* component of *M* and H_s, it assumes that the offset phase shift in the calculation is zero. As a result, the calculation causes a distortion in the phase contour lines when the specimen shape is asymmetric. However, this problem can be solved if we provide the reasonable offset, which can be deduced from either phase calculations by using the line integral with reference to the vector potential *A* (in place of the magnetic flux density *B*) or analysis of the EH observation. To avoid the unwanted distortion in the phase map, this technique was employed in the estimation of $\Delta\phi_{H_d}$.

(3) The effectiveness of the method to determine $\Delta\phi_{H_d}$was demonstrated using the artificial $Nd_2Fe_{14}B$ specimen having a simple rectangular shape. Following the process mentioned in (1) and the selection of the correct offset in the surface integral, $\Delta\phi_{H_d}$ could be extracted from the phase image representing EH observation due to $\Delta\phi_B$. The mapping of H_d was derived from the differential for $\Delta\phi_{H_d}$. The magnitude of demagnetization field

($\mu_0 H_d$) was maximized close to the specimen edge, resulting in the maximum value of 0.67 T. The result was reasonable when referred to micromagnetic calculations (reported in previous studies) carried out for small crystal grains (~10 nm) in in the $Nd_2Fe_{14}B$ phase.

(4) The effectiveness of the method was examined in greater detail using the EH observation for a real thin-foiled, single-crystalline $Nd_2Fe_{14}B$ specimen. As mentioned in (1), to obtain the crystallographic/morphological information of the real specimen, the observations for the real specimen by multiple electron microscopy techniques, which includes the electron diffraction pattern and electron energy-loss spectroscopy (EELS), enabled us to calculate the *y* component of *M* and H_s. The surface integral calculations with reference to these results yielded $\Delta\phi_M$ and $\Delta\phi_{H_s}$, to which the removal operation from EH observation of $\Delta\phi_B$ was applied to obtain the phase map about $\Delta\phi_{H_d}$. As a result, the mapping of H_d could be determined for the real specimen having an asymmetric shape with thickness variation. The H_d map showed a good agreement with the micromagnetic simulation. Indeed, in terms of the magnetic flux density, the deviation from the theoretical calculation was less than 0.065 T. Therefore, this method is able to provide a reasonable map of H_d for actual sintered magnets, which can serve as a foundation in the study of the coercivity.

(5) It was demonstrated that the noise reduction using WHMM could be effective for suppressing the unwanted phase discontinuities, which were artificially produced by the process of phase retrieval using electron holograms with a poor contrast. The noise reduction of WHMM could be useful as well for the extraction of $\Delta\phi_{H_d}$, which is obtained after the

subtraction and differential using the phase images, and accordingly help us improve the precision in the analysis of demagnetization field within a magnetic specimen.

Acknowledgements

During my Ph.D. of about 4 years, I received so much guidance and support from teachers, colleagues, and friends. This thesis could not have been completed without their help and encouragement. I would like to express my gratitude to them who have helped me a lot.

I would like to express my sincere gratitude to my supervisor, Prof. Yasukazu Murakami who guided me wholeheartedly during my Ph.D. Thanks to his academically rigorous and sincere guidance, discussion, and consideration, I was able to complete the thesis. In addition to research, Prof. Murakami took care of me so that I could adapt well to life in Japan. Most of all, I would like to express my deepest appreciation for his thoughtful care and support during the difficult time for my health.

I would like to appreciate Prof. Syo Matsumura, Prof. Kazuhiro Yasuda, Asst. Prof. Satoru Yoshioka, Asst. Prof. Tomokazu Yamamoto for their academic support and valuable advice in my Ph.D. Study.

I would like to thank all the members of this thesis committee for taking the time to review and evaluate the thesis. The valuable comments and suggestions are of great help in enhancing the completeness of this thesis.

I would like to express my gratitude to Dr. Kazuhiro Hono, Dr. Tadakatsu Ohkubo, Dr. Taisuke Sasaki at National Institute for Materials Science for providing the samples and for the numerous help and effort required for my thesis.

I would like to thank Asst. Prof. Yoshihiro Midoh at Osaka University for

his helpful comments and technical support regarding the noise reduction.

I would like to sincerely thank Murakami group's member. Asst. Prof. Takehiro Tamaoka gave me invaluable research advice and discussion, experimental help, and kind consideration. I am grateful to Dr. Kunio Yubuta and Mr. Yuto Tomita for their valuable comments and help with the experiments and analysis. Above all, thanks to Ms. Atsuko Sato for very important help related to simulation in terms of research and for her support and interest so that I can do well in the lab life in Japan.

I would like to thank all the members of Murakami, Yasuda, and Matsumura group and the Ultramicroscopy Research Center of Kyushu University. Pooreun Seo is my dear friend who has been of countless help and strength to me. I am grateful to Dr. Mitsunari Auchi for all his help and time with respect to specimen preparation. I appreciate Dr. Youngji Cho, Dr. Hiroshi Nakajima for their support in my Ph.D. study, and secretary Ms. Hiromi Kumagai and Ms. Mayumi Matsumoto for their patiently help and support for research activities and documents.

I would like to express my sincere gratitude to my parents, brother, Sungcheol, and my friends for their concerns. Thanks to their love and support, I was able to complete my Ph.D.